
**Suche nach elektroschwacher Produktion
supersymmetrischer Teilchen mit dem LHC Experiment
ATLAS bei hohen Luminositäten**

**Search for electroweak production of supersymmetric
particles with the LHC experiment ATLAS
at high luminosities**

Masterarbeit an der Fakultät für Physik
der
Ludwig-Maximilians-Universität München

vorgelegt von
Balthasar Schachtner
geboren in Gräfelfing

München, den 22. Dezember 2014



Gutachterin: Prof. Dr. Dorothee Schaile

Contents

1. Introduction	1
2. Theoretical background	2
2.1. Standard Model	2
2.1.1. Quantum field theory	2
2.1.2. Gauge symmetry	3
2.1.3. Particle content of the SM	3
2.1.4. Limitations of the Standard Model	5
2.2. Supersymmetry	7
2.2.1. Theoretical principle of SUSY	7
2.2.2. R -parity	8
2.2.3. Lifting the limitations of the SM with SUSY	9
2.3. Investigated process	9
2.3.1. Electroweak production of chargino 1 and neutralino 2	10
2.3.2. Decay chain Wh	10
3. Experimental setup	11
3.1. LHC	11
3.1.1. General description	11
3.1.2. Luminosity at the LHC	12
3.1.3. HL-LHC	14
3.2. ATLAS detector and HL-LHC upgrades	16
3.2.1. ATLAS coordinate system	16
3.2.2. Magnet system	17
3.2.3. Inner detector	18
3.2.4. Calorimeter	18
3.2.5. Muon Spectrometer	19
3.2.6. Particle discrimination	19
3.2.7. Trigger system	21
3.2.8. Pile-up	21
4. Monte Carlo generated samples	24
4.1. Monte Carlo event generation	24
4.2. Monte Carlo sample handling	25
4.2.1. Filters on generator level	25
4.2.2. Scaling	25
4.3. Background processes included in the analysis	26
4.3.1. Diboson	26

4.3.2.	Triboson	27
4.3.3.	Top-antitop	27
4.3.4.	Z with jets	27
4.3.5.	W with jets	27
4.3.6.	Generator level filters and resulting true \cancel{E}_T cuts	28
4.3.7.	Production of a new MC slice	30
4.4.	Signal Monte Carlo samples	31
4.5.	Truth information	32
5.	Analysis	33
5.1.	Object selection	33
5.2.	Reconstruction efficiencies and energy smearing	33
5.2.1.	Electrons	34
5.2.2.	Muons	34
5.2.3.	Taus	35
5.2.4.	Jets	35
5.2.5.	Missing transverse energy	36
5.3.	Overlap Removal I	37
5.4.	Fake electrons from jets	37
5.5.	Fake taus from jets	38
5.5.1.	Re-weighting of events	38
5.5.2.	Validation of the re-weighting method	42
5.6.	Overlap removal II	44
5.7.	Lepton isolation	44
5.8.	Object definitions	44
5.9.	Trigger	45
6.	Expected sensitivity in the 1 lepton and 2 tau final state	46
6.1.	Calculation of sensitivity	46
6.2.	Channel definition	47
6.3.	B-tagged jet veto	48
6.4.	Signal regions	49
6.4.1.	Missing transverse energy	50
6.4.2.	Invariant mass of the two taus	52
6.4.3.	Scalar sum of the transverse momenta of the two taus	53
6.4.4.	Transverse mass of the light lepton	55
6.4.5.	Signal region yields	55
6.5.	Expected sensitivities	56
6.5.1.	Results	56
6.5.2.	Exclusion potential at 300 fb^{-1}	61
6.5.3.	Exclusion potential in context	61
7.	Conclusion and outlook	64
A.	Parameters for detector response	65

B. Correlations for generator cut and true \cancel{E}_T	66
C. Generator cut on \cancel{E}_T	68
D. MC weights	70
E. Cutflow optimistic signal region	74
Bibliography	75

1. Introduction

About 60 years ago on 29 September 1954 the European Organization for Nuclear Research CERN came into being. A place for the international collaboration of scientists was born. Already a few years later the first accelerator at CERN, the Synchrocyclotron, was built and since then a number of important experiments have taken place at CERN pushing the frontiers in particle physics. The latest of these experiments, the Large Hadron Collider LHC, surpasses all previous accelerators in its extraordinary performance. Since the discovery of a particle consistent with the expected properties of the Higgs Boson the focus of LHC's researchers has shifted more than ever to physics beyond the Standard Model.

Since some time the problems of dark matter and fine-tuning have provided the need for theories beyond the Standard Model. Among the best developed theories are those incorporating a new symmetry, called Supersymmetry. Supersymmetric theories provide a relation between the two fundamental categories of particles: Bosons and fermions. During the previous run of the LHC the exclusion limits for supersymmetric theories could be raised, but many meaningful models are still possible and extended parts of the large parameter spaces which have to be searched are only accessible through an increased amount of data.

In order to maximize the gain from the LHC and to extend the reach of its experiments extensive studies on upgrades of the LHC have been conducted. An important part of the plans is the upgrade of the machine to a High Luminosity LHC. This includes not only upgrades of the accelerator parts but also of the experiments taking data. The proposed target of this project is to take ten times the data the LHC is supposed to take in its original schedule.

This thesis presents an analysis targeting this high luminosity scenario. The ATLAS experiment has published a set of functions parameterizing the expected detector performance and Monte Carlo samples simulating the collisions with an increased center of mass energy of 14 TeV have been produced. An analysis is conducted to explore the expected sensitivity in electroweak production of supersymmetric particles with 3000 fb^{-1} at the ATLAS detector. The analysis is further specialized in the decay channel of Wh decaying to one light lepton and two taus.

Special attention is given to the impact of the available Monte Carlo samples on the analysis. An investigation of the filter requirements implies raised analysis cuts and in order to provide conservative estimates dedicated analyses on the background processes were conducted. In the end the estimates for the sensitivity and the resulting exclusion limits are derived and presented for different signal regions and scenarios and a comparison to the related analysis with three light leptons in the final states is drawn.

2. Theoretical background

In the following sections a brief overview over the theoretical framework used in particle physics is given. After a short introduction to the Standard Model (SM), the motivations and concepts of Supersymmetry (SUSY) are illustrated and finally the process under consideration for this analysis is presented.

2.1. Standard Model

Since the discovery of the electron in 1897 by J. J. Thomson, elementary particle physics has made extraordinary progress in understanding the fundamental processes in our universe. Not only numerous discoveries of new particles mark the progress, but the development of special relativity by A. Einstein and the advent of quantum mechanics provided the necessary tools for today's theoretical framework of particle physics.

2.1.1. Quantum field theory

The theoretical framework of particle physics combines the aspects of special relativity and quantum mechanics into a common framework called quantum field theory. Quantum field theories (QFT) adopt a field formalism, where the elementary particles will be represented as excitations of these fields.

The underlying idea is to develop, borrowing from classical mechanics, a Lagrangian density \mathcal{L} incorporating fields ϕ with the action [1]:

$$S = \int \mathcal{L}(\phi, \partial_\mu \phi) d^4x$$

With the principle of least action the Euler-Lagrange equations of motion

$$\partial_\mu \left(\frac{\partial \mathcal{L}}{\partial(\partial_\mu \phi)} \right) - \frac{\partial \mathcal{L}}{\partial \phi} = 0$$

can be derived yielding the evolution of free fields.

To include quantum mechanics a path integral approach or the canonical quantization is applied on the fields. These fields fulfill then commutation relations and can therefore be seen as operators in a quantum mechanical sense.

Interactions are implemented in the theory with a perturbation based approach. Feynman diagrams with propagators (lines) and interaction points (vertices) can be used to visualize this perturbative expansion. The expansion is done in terms of the coupling parameters α_j .

An important aspect of the perturbation employed is that integrals over arbitrarily high momenta may not converge. For these divergences techniques as e.g. renormalization schemes were developed. These schemes introduce scale-dependent couplings which will lead to considerations on the unification of forces.

2.1.2. Gauge symmetry

The SM is described by a QFT with three gauge symmetries. Gauge symmetries are internal symmetries of the Lagrangian, which give rise to the gauge bosons, the mediators of forces.

The first big success of QFTs was the introduction of a local U(1) symmetry, giving rise to a boson interacting with particles, where $U(n)$ describes the group of unitary $n \times n$ matrices. Interpreting the gauge boson as photon, the theory can be used to describe electromagnetic interactions and is known as quantum electrodynamics (QED).

In the context of QFTs, tools for high-precision calculations were developed. The anomalous magnetic moment of the electron can be measured within a relative uncertainty of $2.6 \cdot 10^{-13}$ [2] and agrees with the theory prediction within the calculated uncertainties. This is probably the best confirmation of QED.

Exploring the principle of gauge symmetries to higher dimensional Lie groups, it turned out that the SM can be described as a combination of the local symmetry groups

$$SU(3)_C \otimes SU(2)_L \otimes U(1)_Y.$$

$SU(3)_C$ describes the interaction of particles carrying color charge via the exchange of eight gluons, called quantum chromodynamics (QCD). The electroweak interaction is described by $SU(2)_L \otimes U(1)_Y$, where L indicates the left handedness of the SU(2) interaction and Y is the hypercharge. This symmetry is spontaneously broken by the Higgs field. The Gell-Mann-Nishijima formula relates the hypercharge with the electric charge Q and the third component of the isospin I^3 :

$$Q = I^3 + \frac{1}{2} Y$$

After the symmetry breaking the chiral interaction describes the weak interaction and the U(1) symmetry resembles the previously mentioned QED.

2.1.3. Particle content of the SM

The full standard model Lagrangian can be used to describe most of the phenomenons known in elementary particle physics. This section describes the particle content of the SM, while the limitations of the SM are illustrated in the next section.

The fundamental particles of the Standard Model can be divided by their intrinsic quantum number spin in two basic categories. Particles with half-integer spin¹ follow the Fermi-Dirac statistics and are therefore called *fermions*, and integer-spin particles follow the Bose-Einstein statistics and are called *bosons*. This fundamental relationship of quantum field theories is called spin-statistics theorem.

¹Using the common convention of high-energy physics $\hbar = c = 1$.

spin	0	1				2
particle	H^0	γ	g	W^\pm	Z	graviton
electric charge	0	0	0	$\pm e$	0	0
mass [GeV]	125.7 ± 0.4	0	0	80.385 ± 0.015	91.1876 ± 0.0021	0

Table 2.1.: Bosonic content of the SM and gravity [3], photon, gluon and graviton mass are set to their theoretically expected value 0 eV.

Bosons

The bosons of the SM mediate the interactions of all particles. They are listed in Tab. 2.1 according to their spin with the corresponding masses and electric charges.

Bosons with spin 1, often called vector bosons or force carriers, are the *photon* (γ) mediating the electromagnetic interaction, W and Z bosons mediating the weak interaction and *gluons* (g) mediating the strong interaction. Gravity is commonly assumed to be mediated by a spin-2 *graviton*, but till now it has not been observed.

In 2012 the scalar Higgs boson was discovered at the LHC experiments ATLAS and CMS ([4],[5]). It plays an important role, since it breaks the $SU(2) \otimes U(1)$ electroweak symmetry to give mass to the W and Z bosons and it introduces Yukawa couplings for fermions. The Yukawa couplings are needed to include fermion masses without violating the gauge invariance of the Lagrangian. If fermions acquire their mass due to Yukawa couplings, a direct consequence is that the coupling of the Higgs boson to fermions is proportional to the fermion masses.

Fermions

For fermions the Pauli principle applies, which is the fact that the wave function is antisymmetric under exchange of two identical particles. This implies that two indistinguishable fermions cannot occupy the same state [6]. Fermions are observed in two families with each three generations:

- The left handed *leptons* are doublets with respect to $SU(2)$ and contain one charged lepton and the corresponding neutrino $\left(\begin{pmatrix} e^- \\ \nu_e \end{pmatrix}, \begin{pmatrix} \mu^- \\ \nu_\mu \end{pmatrix}, \begin{pmatrix} \tau^- \\ \nu_\tau \end{pmatrix} \right)$. W bosons mediate the conversion from charged lepton to its neutrino and vice versa.
- Left handed *quarks* are doublets with respect to $SU(2)$ as well, but carry also a color charge and therefore interact additionally strongly $\left(\begin{pmatrix} u \\ d \end{pmatrix}, \begin{pmatrix} c \\ s \end{pmatrix}, \begin{pmatrix} t \\ b \end{pmatrix} \right)$. Quarks decay via emission of W bosons preferred within the doublets, but as in the CKM matrix described (see e.g. [3]), there are also flavor-changing decays possible. The three upper (“up-type”) quarks carry a $+\frac{2}{3}e$ and the lower (“down-type”) quarks a $-\frac{1}{3}e$ electric charge.

In Tab. 2.2 the SM fermions with their masses and electric charges are listed.

	generation	particle	electric charge	mass
leptons	1	e^-	$-e$	0.511 MeV
		ν_e	0	0 eV
	2	μ^-	$-e$	105.7 MeV
		ν_μ	0	0 eV
	3	τ^-	$-e$	1.777 GeV
		ν_τ	0	0 eV
quarks	1	d	$-\frac{1}{3}e$	4.8 MeV
		u	$\frac{2}{3}e$	2.3 MeV
	2	s	$-\frac{1}{3}e$	95 MeV
		c	$\frac{2}{3}e$	1.28 GeV
	3	b	$-\frac{1}{3}e$	4.18 GeV
		t	$\frac{2}{3}e$	173 GeV

Table 2.2.: Fermionic content of the SM [3], neutrino masses are set to 0 eV, c and b masses are calculated with the $\overline{\text{MS}}$ scheme.

2.1.4. Limitations of the Standard Model

The Standard Model provides a remarkable description of the experiments in particle physics. There are however some inherent limitations to the standard model.

Gravity

A fundamental limitation of the Standard Model is the missing inclusion of gravity. Since gravity is the weakest force, it is usually neglected in the description of experiments in particle physics. It is enough to describe the other three of the four known forces in the SM. The Planck scale can be derived, an energy scale where the effects of gravity would become important. The Planck scale is at 10^{19} GeV, an energy not even close to our experimental reach.

Unification of forces

With the unified description of weak and electromagnetic interaction the question arose if a unification with the strong force was possible. One way to verify if a unification is possible is to extrapolate the three couplings to high energies. It turns out, that in the SM, despite crossing each other, the coupling constants do not reach the same value at the same energy. Fig. 2.1 shows an illustration of the extrapolation of the couplings in the case of SM and SUSY. It is appealing to assume that a unification of the forces exists, since a single grand unified theory could be developed, from which the SM could be derived.

Dark matter

There is compelling astrophysical evidence that a non-SM form of matter called dark matter exists. One possibility is to observe the tangential velocity of stars in galaxies

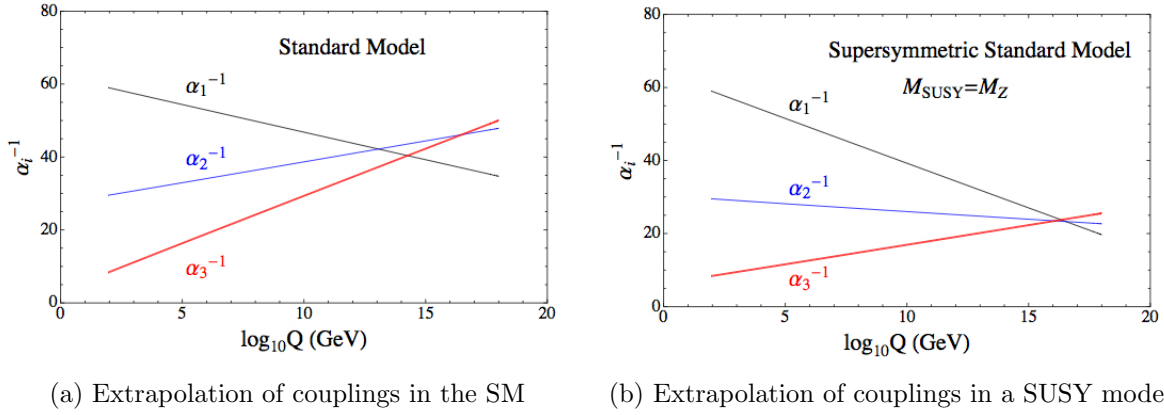


Figure 2.1.: Illustration of the extrapolation of coupling constants for SM and SUSY in terms of the energy scale of the interaction. In the SM the coupling constants do not reach the same value at one energy. In SUSY a perfect meeting point might be possible [7].

using the doppler shift of their atomic spectra [8]. Plotting the velocity with the distance to the center, a rotation curve is obtained. From the brightness of the galaxy an estimate for the visible mass distribution in the galaxy can be given. Comparing the expected rotation curve from the mass estimate with the observed one, a substantial discrepancy can be seen. It indicates that the galaxies are made of more matter than the visible one.

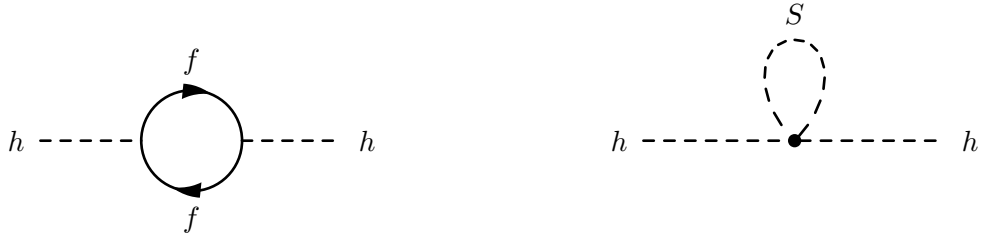
The only candidate within the SM particles not interacting electromagnetically is the neutrino, but due to their low mass they are too fast to be able to explain structure formation. The need for cold dark matter with heavier particles arises. Current searches target an unknown weakly interacting massive particle (WIMP) as explanation for the dark matter observations.

Fine-tuning of the Higgs mass

The last limitation of the SM presented here is the enormous sensitivity of the mass of the Higgs boson to quantum corrections. According to [9] the correction to m_H^2 from the fermionic loop diagram shown in Fig. 2.2a is

$$\Delta m_H^2 = -\frac{|\lambda_f|^2}{8\pi^2} \Lambda_{UV}^2 + \dots,$$

where λ_f is the coupling strength of the fermion and Λ_{UV} the ultraviolet momentum cutoff. If one assumes that there is no new physics up to the Planck scale which could change the high-energy behavior of the theory, the cutoff has to be at least at this scale. It is hard to believe that the Higgs mass of about 125 GeV is subjected to quantum corrections with quadratic dependence on values of the order of the Planck scale. This leads to considerations called naturalness, which forbid extensive fine-tuning of parameters and require that there is a model explaining the parameters without much fine-tuning, but a higher principle.



(a) Loop correction to the Higgs mass due to a fermion f (b) Loop correction to the Higgs mass due to a scalar S

Figure 2.2.: One loop corrections to the Higgs mass.

2.2. Supersymmetry

Wess and Zumino suggested in 1974 a model including a symmetry relating fermions and bosons. This Supersymmetry (SUSY) can provide solutions for the previously discussed limitations of the SM. The theoretical principle and the implications are discussed in the following, leading to the explanation how SUSY helps to overcome the limitations of the SM.

2.2.1. Theoretical principle of SUSY

Supersymmetry introduces the fermionic operators Q and Q^\dagger (hermitian conjugate of Q) as generators of supersymmetric transformations:

$$Q |\text{Boson}\rangle = |\text{Fermion}\rangle, \quad Q |\text{Fermion}\rangle = |\text{Boson}\rangle$$

Therefore every boson obtains a fermionic superpartner and every fermion a bosonic superpartner, each differing by spin $\frac{1}{2}$, but equal in all other quantum numbers.

The generators have to fulfill the following commutation relations:

$$\{Q, Q^\dagger\} \propto P_\mu \quad (2.1)$$

$$\{Q, Q\} = \{Q^\dagger, Q^\dagger\} = 0 \quad (2.2)$$

$$[P^\mu, Q] = [P^\mu, Q^\dagger] = 0 \quad (2.3)$$

Since the momentum operator P_μ commutes with the generators of SUSY, the squared-mass operator P^2 also commutes with the generators and therefore the superpartners have to have equal masses.

It is clear from observations, that SUSY is not realized with equal masses of the superpartners, since e.g. the superpartner of the electron (called selectron²) would be easily observable. In a realistic theory it has to be assumed that SUSY is a (softly) broken symmetry. This breaking introduces small terms violating SUSY and lets the superpartners acquire more mass than the SM partners.

Fig. 2.3 shows some of the possible gauge interaction vertices in SUSY. In addition to the SM couplings (a), (b), (f) there is the later on important gauge boson-gauginos

²Names of the superpartners are obtained by prepending “s” for fermions and by appending “ino” for bosons.

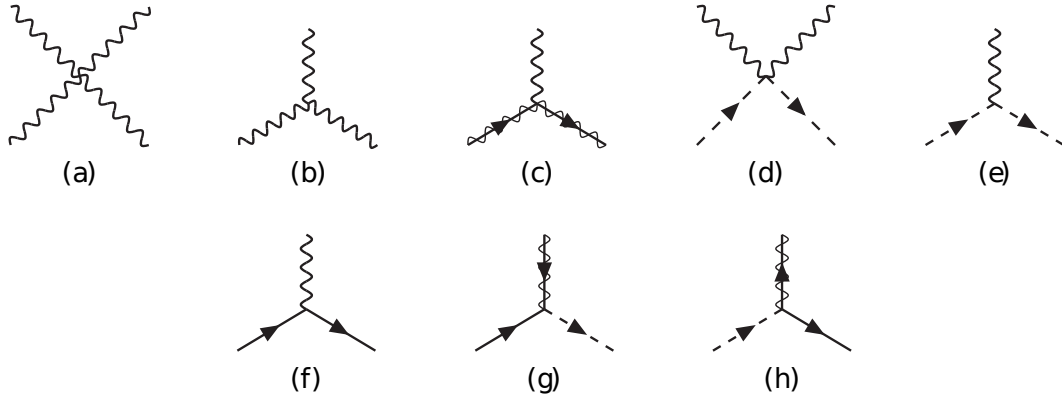


Figure 2.3.: SUSY gauge interaction vertices. The wavy lines overlaid on fermion lines represent gauginos, while dashed lines with arrows correspond to sfermions [9].

coupling (c) and the gauge boson-sfermion couplings (d) and (e). (g) and (h) connect sfermion, fermion and gaugino into a vertex.

For a fully supersymmetric theory the Higgs sector needs to be extended. In a minimal model two complex Higgs doublets are introduced, which will after the electroweak symmetrybreaking give rise to five Higgs bosons. There are two CP-even neutral bosons h_0 and H_0 , with h_0 being the lighter one and identified with the observed SM Higgs boson. Additionally a pair of charged Higgs bosons H^\pm and a CP-odd neutral A_0 are introduced.

Since Higgsinos as well as photino, zino and winos have spin $\frac{1}{2}$, they gain with the exception of the electrical charge identical quantum numbers. This means the neutral (charged) gauginos and Higgsinos will be mixed states, called neutralinos $\tilde{\chi}_{1,2,3,4}^0$ (charginos $\tilde{\chi}_{1,2}^\pm$).

2.2.2. R -parity

Another important concept experimentally observed is R -parity. If no further constraints are applied, SUSY contains vertices which allow the decay of protons. Experiments have already put strong limits on the lifetime of the proton. In the decay channel $p^+ \rightarrow e^+ \pi^0$ the partial mean life time is $> 8.2 \cdot 10^{33}$ years [3]. Fig. 2.4 shows the diagram of a possible proton decay in this channel. Assigning quarks a baryon number B of $\frac{1}{3}$

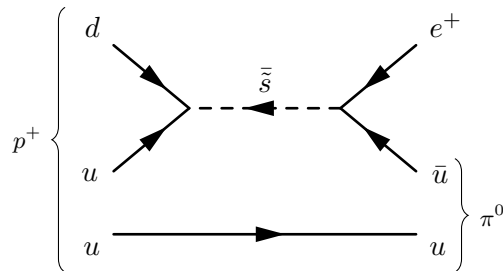


Figure 2.4.: Diagram of the proton decay mediated by a strange squark. Both vertices shown here are R -parity violating.

and leptons a lepton number L of 1 (the antiparticles have the resp. negative value), this process violates baryon number and lepton number conservation ($\Delta B = 1$, $\Delta L = -1$).

R -parity is defined as

$$P_R = (-1)^{3(B-L)+2s},$$

such that SM particles have R -parity equals +1 and SUSY particles R -parity equals -1 . It is a multiplicative quantum number, similar to the conventional parity.

R -parity conservation forbids the vertices shown in Fig. 2.4. The initial state has R -parity of 1, since quarks have a baryon number of $\frac{1}{3}$ and spin of $\frac{1}{2}$:

$$P_R(\text{quark}) = (-1)^{3(\frac{1}{3}-0)+2\frac{1}{2}} = (-1)^2 = 1$$

The intermediate state has R -parity of -1 , since the anti-squark has a baryon number of $-\frac{1}{3}$ and a spin of 0,

$$P_R(\text{anti-squark}) = (-1)^{3(-\frac{1}{3}-0)+2\cdot 0} = (-1)^{-1} = -1,$$

and the spectator quark still has R -parity of +1. Therefore R -parity is violated and the decay forbidden.

The introduction of R -parity conservation has several implications:

- SUSY particles can only be produced in pairs from SM processes, since the final state needs to have R -parity of +1.
- There will be a lightest supersymmetric particle (LSP), which is stable, since with R -parity of -1 it cannot decay to a SM only final state, which would have R -parity of +1.
- SUSY particles usually decay (maybe via intermediate steps) to LSPs.

2.2.3. Lifting the limitations of the SM with SUSY

SUSY is a theory which can lift the limitations of the SM presented in Sec. 2.1.4, while it still lacks an inclusion of gravity.

SUSY more than doubles the number of elementary particles contrary to the SM, therefore establishing in many models new physics far below the Planck scale. It modifies the running of couplings in a way that a unification of the forces at high energies seems possible (see illustrations in Fig. 2.1b).

With the introduction of R -parity conservation, which implies a LSP, a dark matter candidate is provided. Assuming that the LSP is neutral, it may play the role of a WIMP.

For the high sensitivity of the corrections to the Higgs boson mass, the contributions of the SM particles are canceled by destructively interfering diagrams of the superpartners (cf. Fig. 2.2b).

2.3. Investigated process

Since SUSY provides a variety of possible models, analyses have to be limited to a small subset. In the following the process considered in the following analysis is highlighted and the resulting signature presented.

2.3.1. Electroweak production of chargino 1 and neutralino 2

Fig. 2.5 shows two possible production processes for $\tilde{\chi}_2^0$ and $\tilde{\chi}_1^\pm$. (a) is a Drell-Yan like production of a W boson splitting with the vertex (c) of Fig. 2.3 into both supersymmetric particles. (b) shows the t-channel process with exchange of a sfermion, realizing vertices (g) and (h).

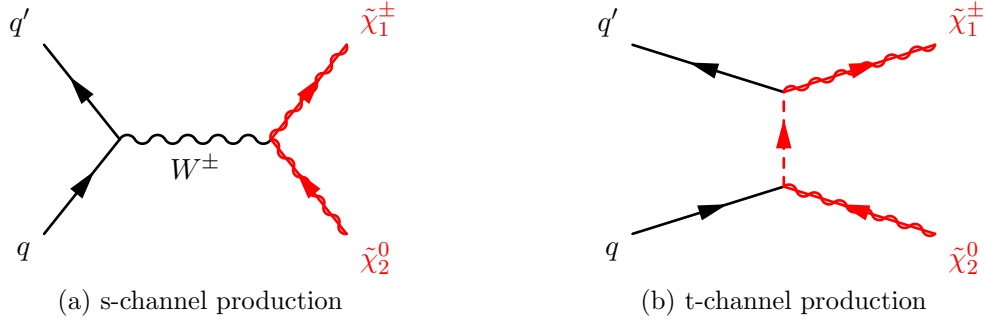


Figure 2.5.: Feynman diagrams of electroweak production of $\tilde{\chi}_2^0$ and $\tilde{\chi}_1^\pm$. The red lines indicate supersymmetric particles.

2.3.2. Decay chain Wh

In this analysis the process shown in Fig. 2.6 is used. It incorporates the previously described associated electroweak production of $\tilde{\chi}_2^0$ and $\tilde{\chi}_1^\pm$.

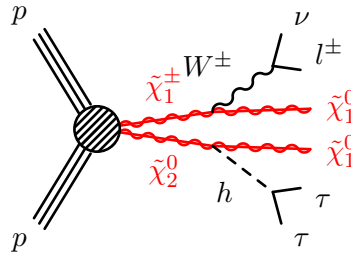


Figure 2.6.: Feynman diagram of the complete considered process. Electroweak production of a chargino 1 and neutralino 2 and subsequent decay via W to a light lepton and via h to two hadronic taus

In the following the $\tilde{\chi}_1^\pm$ decays via the emission of a W boson to a LSP ($\tilde{\chi}_1^0$). The W boson decays leptonically, giving rise to a light lepton (e, μ) and the corresponding neutrino.

The $\tilde{\chi}_2^0$ also decays directly to a LSP and emits a h_0 which is assumed to be a SM-like Higgs boson. This Higgs boson decays to two hadronically decaying taus. This process can only happen if the mass splitting fulfills $m_{\tilde{\chi}_2^0} - m_{\tilde{\chi}_1^0} > 125$ GeV.

3. Experimental setup

3.1. LHC

The European Organization for Nuclear Research (CERN) is one of the most important institutions for high energy physics. Over the last 60 years it has been one of the leading institutions for development and construction of accelerators. Most notably it constructed the Super Proton Synchrotron (SPS), which enabled the discovery of W and Z bosons, and the Large Electron Positron Collider (LEP), the highest-energetic accelerator for leptons until today, providing high-precision measurements of the electroweak interaction [10] and excellent confirmation of the standard model.

Fermilab¹ constructed with the Tevatron a proton-antiproton collider with a proton (antiproton) energy up to 0.98 TeV. CERN superseded this record of beam energy with the Large Hadron Collider (LHC), which is designed to operate at 7 TeV proton energy, with an energy of 1.18 TeV in 2009 [11].

3.1.1. General description

CERN decided to reuse the tunnel housing LEP after its end of service. Since the center-of-mass energy for LEP was limited by synchrotron radiation losses, an upgraded electron-positron accelerator was not feasible and it was decided to install a hadron collider, the LHC, in the existing tunnel [12].

Therefore LHC follows the tunnel layout of LEP with eight alternating straight sections and arcs. One half of the straight sections are beam crossings providing collisions for the experiments, the other straight sections serve various purposes listed below.

Another legacy of LEP and CERN in general is the accelerator chain. Figure 3.1 shows the accelerators delivering the protons to the LHC. Starting with the linear accelerator LINAC protons, created from hydrogen, are accelerated and transferred to the Proton Synchrotron Booster (PSB), which increases the proton energy up to 1.4 GeV [14]. The next stage of acceleration happens at the Proton Synchrotron (PS) up to 25 GeV proton energy. The Super Proton Synchrotron finally takes the protons to 450 GeV an energy, at which they can be injected into the LHC.

The arcs house the dipole magnets, which bend the protons on their quasi-circular trajectory. Since protons are circulating in both directions, their equal charges require propagation in separate beam pipes with opposite magnetic fields. The superconducting dipole magnets are designed to achieve a magnetic field strength of 8.33 T for the maximal proton energy [15].

At four of the straight sections LHC provides proton-proton collisions for the experiments. There are the two omni-purpose experiments ATLAS and CMS, designed to be

¹Fermi National Accelerator Laboratory

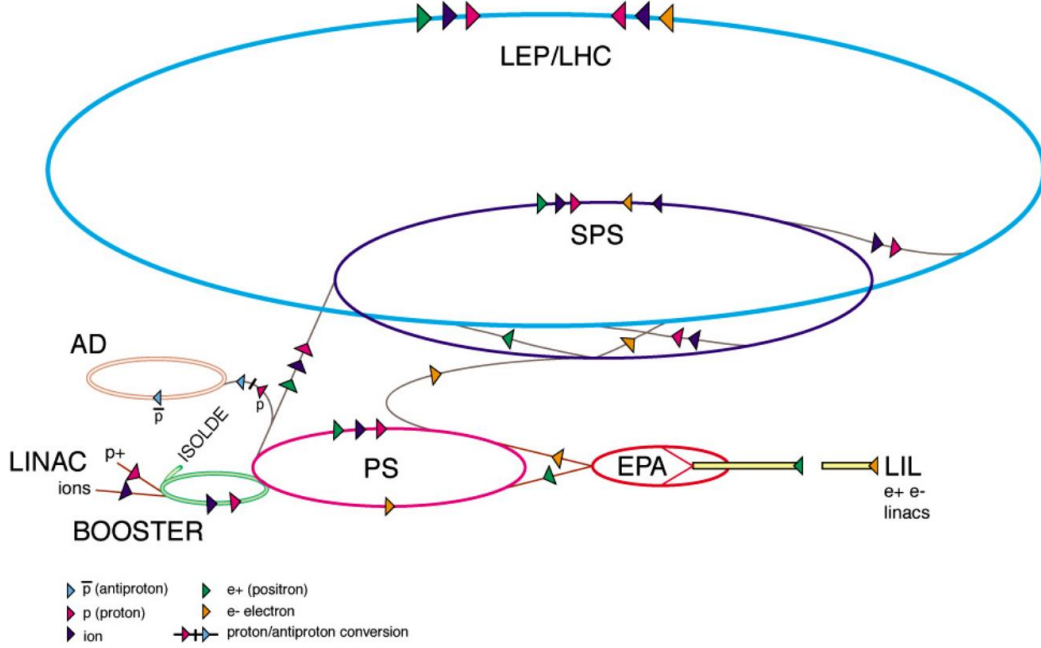


Figure 3.1.: Schematic overview of the accelerators involved at LEP and LHC. Protons for the LHC are accelerated in several stages, starting at LINAC through the PSB (BOOSTER), PS, SPS and are finally brought to the maximal center-of-mass energy by the LHC [13].

able to search for a broad variety of processes and to give a nearly full coverage of the interaction region. Especially searching and measuring the Higgs boson and supersymmetric particles were central design criteria. ALICE is dedicated to investigate heavy-ion collisions and to improve our understanding of QCD. LHCb is finally specialized in B-physics, e.g. investigating the asymmetry between matter and antimatter. An overview over the experiments is given in Fig. 3.2.

Two of the remaining four straight sections are used for momentum and betatron cleaning, while the others house the radio-frequency (RF) and feed-back system, resp. the abort system with the beam dump.

3.1.2. Luminosity at the LHC

A useful measure for the performance of particle colliders is the luminosity. The number of events containing a certain process is given by the product of the cross-section of this process σ and the time integral over the instantaneous luminosity \mathcal{L} [3]:

$$N_{\text{events}} = \sigma \int \mathcal{L} dt \quad (3.1)$$

The instantaneous luminosity can be expressed using beam parameters, where N_b is the number of protons per bunch, n_b is the number of bunches per beam, f_{rev} the

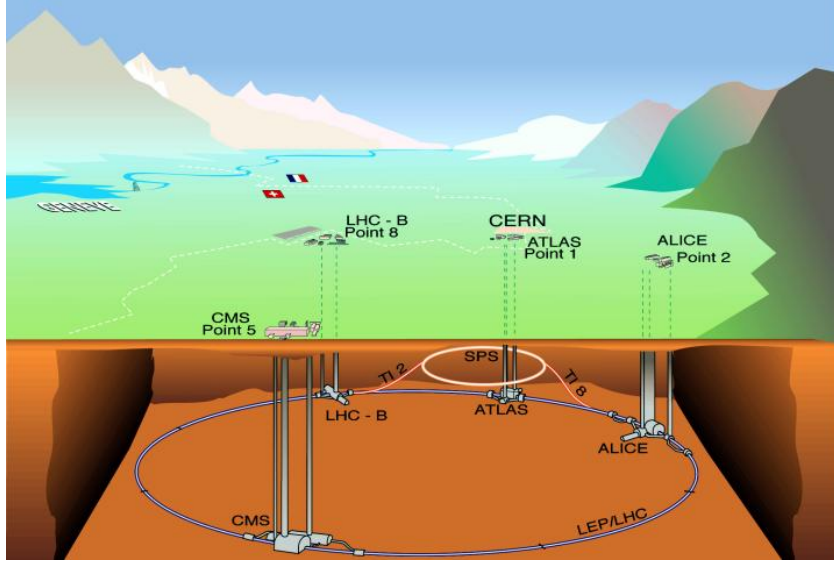


Figure 3.2.: Schematic overview of the situation of the LHC near Geneva with the CERN site and the four main experiments. [16]

revolution frequency and γ_r the relativistic gamma factor [15]:

$$\mathcal{L} = \frac{N_b^2 n_b f_{\text{rev}} \gamma_r}{4\pi \epsilon_n \beta^*} F \quad (3.2)$$

The parameters describing the beam size are: The normalized transverse emittance ϵ_n , a measure of the beam quality, and the amplitude function β^* , quantifying the squeezing of the beam optics at the interaction point. Since the beams collide at an angle θ_c , the luminosity is corrected, with respect to head-on collisions, by the geometric luminosity reduction factor

$$F = \sqrt{1 + \left(\frac{\theta_c \sigma_z}{2\sigma^*}\right)^2}^{-1}, \quad (3.3)$$

where σ_z is the root mean square (RMS) of the bunch length and σ^* the RMS of the transverse beam size at the interaction point.

The number of events produced at the collider can be increased by prolonging the time the accelerator provides collisions and by increasing the instantaneous luminosity. The instantaneous luminosity however is constrained by the machine parameters.

For high-energy accelerators the revolution frequency is fixed by the layout of the collider and cannot be improved. The gamma factor, given by the particle energy, is unalterable at least for practical purposes, since the maximal energy of the particles is given by the field strength of the bending magnets, whose upgrade is costly or even limited by the available technology. The number of bunches per beam is also a parameter which is inherent to the design of the accelerator chain. At the LHC the bunch-spacing is limited to 25 ns. All other presented parameters are targeted by the upgrade efforts and will be explained in more detail in the following Sec. 3.1.3.

LHC does not only push the boundary in terms of beam energy, but also in terms of luminosity. Using equation 3.2, the revolution frequency given by

$$f_{\text{rev}} = \frac{3.00 \cdot 10^8 \frac{\text{m}}{\text{s}}}{27 \text{ km}} = 11.1 \text{ kHz}$$

and the values from table 3.1 one can easily calculate the nominal peak luminosity of $10^{34} \text{ cm}^{-2}\text{s}^{-1}$. This instantaneous luminosity is planned to be reached during run 2, scheduled to start in spring 2015 and ending the long shutdown 1 (LS1) [17].

γ_r	7461	ϵ_n	$3.75 \mu\text{m rad}$
N_b	$1.15 \cdot 10^{11}$	F	0.836
n_b	2808	β^*	55 cm

Table 3.1.: Nominal LHC parameters for the calculation of the peak luminosity with 7 TeV proton energy. [15]

3.1.3. HL-LHC

In the LHC baseline program it is planned to gather about 300 fb^{-1} of integrated luminosity until around 2022 with the intermission of another long shutdown (LS2) starting mid-2018 and ending end of 2019. At this point the statistical gain of running LHC at an unchanged instantaneous luminosity will be small [18]. Figure 3.3 shows a recent timetable of the HL-LHC plans.

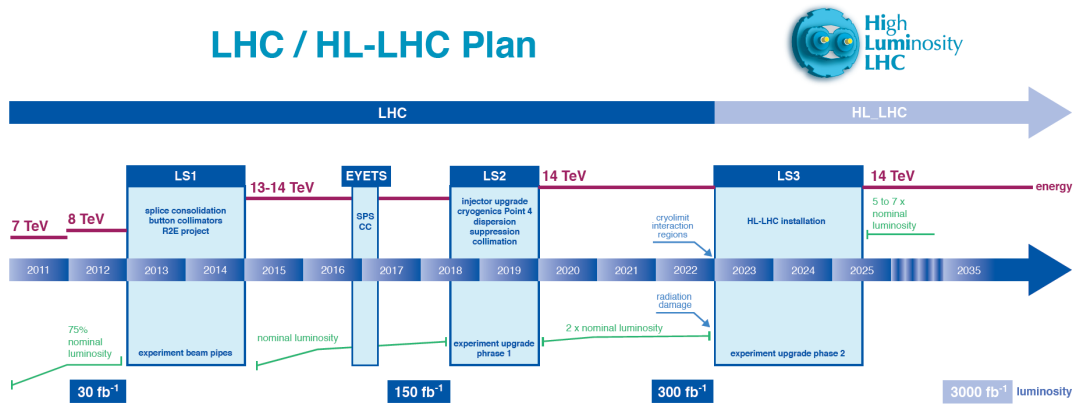


Figure 3.3.: Recent plan of operation of the LHC with planned intermissions and the HL-LHC proposal. [19]

The High-Luminosity LHC (HL-LHC) scenario proposes several upgrades, some during LS2 and most of them during LS3, to achieve an instantaneous luminosity up to ten times of the nominal one. HL-LHC is supposed to run about 10 additional years until in total 3000 fb^{-1} of data are recorded. Important parts of the upgrade target the injector chain, the dipole magnets and the inner triplets, but also consider concepts like extended beam scrubbing, crab bunch tilting or luminosity leveling.

LHC injector upgrade

The LHC Injector Upgrade (LIU) describes the preparation of the accelerator chain for the HL-LHC upgrade. Recalling equation 3.2 (p. 13), it aims to reduce the normalized transverse emittance ϵ_n and prepares the smaller accelerators for high-intensity beams, enabling to overcome limitations of the number of protons per bunch N_b . A more detailed status update is given in [20]. One example is LINAC4, the successor of LINAC2, which is already in construction [21]. It uses H^- -ions, in contrast to LINAC2, which uses protons, for acceleration and will be able to deliver protons with an energy of 160 MeV to PSB (LINAC2: 50 MeV) and help to improve the beam quality. The commissioning is planned to end in 2015. The year 2016 is reserved for reliability tests and already in 2017 LINAC4 will be ready for operation. One year later during LS2 LINAC4 is planned to be included into the LHC accelerator chain.

Dipole magnet upgrade

It is planned to replace some of the LHC 8.33 T dipoles (Nb-Ti) with shorter 13 T superconducting magnets (Nb-Sn) to provide space for additional focusing and defocusing quadrupoles while maintaining the same center-of-mass energy. The second major magnet upgrade is the renewal of the so-called inner triplets, the magnets squeezing the beam in the interaction regions. Increasing the magnetic aperture of the inner triplet and employing a scheme called Achromatic Telescopic Squeeze (ATS), which essentially extends the beam optics to the adjacent arcs, are planned to reduce the beta-function β^* from nominal 55 cm to around 15 cm [22].

Beam scrubbing

A problematic effect expected to grow with increasing beam currents are secondary electrons from the beam pipe. The Secondary Electron Yield (SEY) is the number of electrons emitted by the beam screen per incident particle. If the SEY gets too high, so called “electron-clouds” accumulate and get amplified with every bunch flying past. The electron-clouds extract energy from the beam and increase the heat load for the cryogenics system, which can lead to an early beam dump and therefore a shortened operation time of the LHC. Besides special coating of the beam pipe to reduce the SEY, extended “beam scrubbing” is under consideration. This method uses low-intensity proton bunches² with a reduced bunch spacing (e.g. 5 ns) to significantly reduce the SEY of the beam screen. [23]

Crab bunch tilting

Targeting the geometric correction factor F (cf. eq. 3.3) the so called “crab bunch tilting” was devised. F corrects for the only partial overlap of the bunches at the collision. In an ideal case there would be a head-on collision ($F = 1$). Special crab cavities for point 1 and 5 (ATLAS and CMS) are developed to tilt the bunches out of their alignment along the beam trajectory into an orientation along the symmetry axis of the detectors,

²15-20 % of the nominal intensity

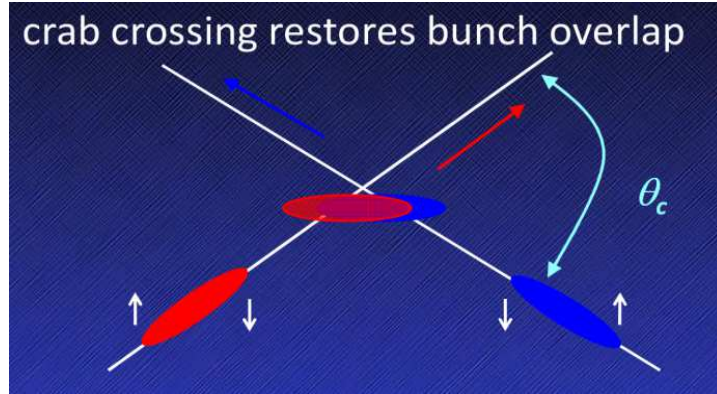


Figure 3.4.: Illustration of crab bunch tilting. Both bunches are at first aligned with the beam axis and get tilted for maximal overlap at the interaction point, without changing the crossing angle. [24]

without the need to change the crossing angle. F could be increased by 41 % to 68 % (cf. [24]) with tilted bunches (cf. Fig. 3.4).

Luminosity leveling

Increasing the instantaneous luminosity above $5 \cdot 10^{34} \text{ cm}^{-2}\text{s}^{-1}$ is considered to pose problems for the detectors, especially in terms of pile-up, therefore “luminosity leveling” is considered [24]. It describes an operation of the LHC where a several magnitudes higher “virtual” luminosity could be reached, but is artificially kept lower by, e.g. increasing β^* with the inner triplet magnets. During the run the unavoidable decay of luminosity can be counteracted by reducing β^* with the inner triplet, such that a maximal possible time of the run is done at peak instantaneous luminosity.

3.2. ATLAS detector and HL-LHC upgrades

With LHC delivering proton-proton collisions at high luminosities, highly specialized detectors are needed. ATLAS is one of the four main experiments. The concept of ATLAS is to provide a full coverage for all particles interacting electromagnetically and strongly. Undetected escaping particles, like neutrinos or not yet discovered particles, carry away energy, which are measured as missing transverse energy. Reliable particle discrimination and precision momentum determination help to identify the physics processes happening in the detector [26].

3.2.1. ATLAS coordinate system

ATLAS uses a right-handed coordinate system, where the z -axis is oriented along the beam axis and the origin located at the nominal interaction point [26]. The x - y -plane is perpendicular to the beam axis with the x -axis pointing to the LHC center and the y -axis pointing upwards. Transverse variables, like transverse momentum p_T , transverse energy E_T or missing transverse energy \cancel{E}_T are defined in this plane.

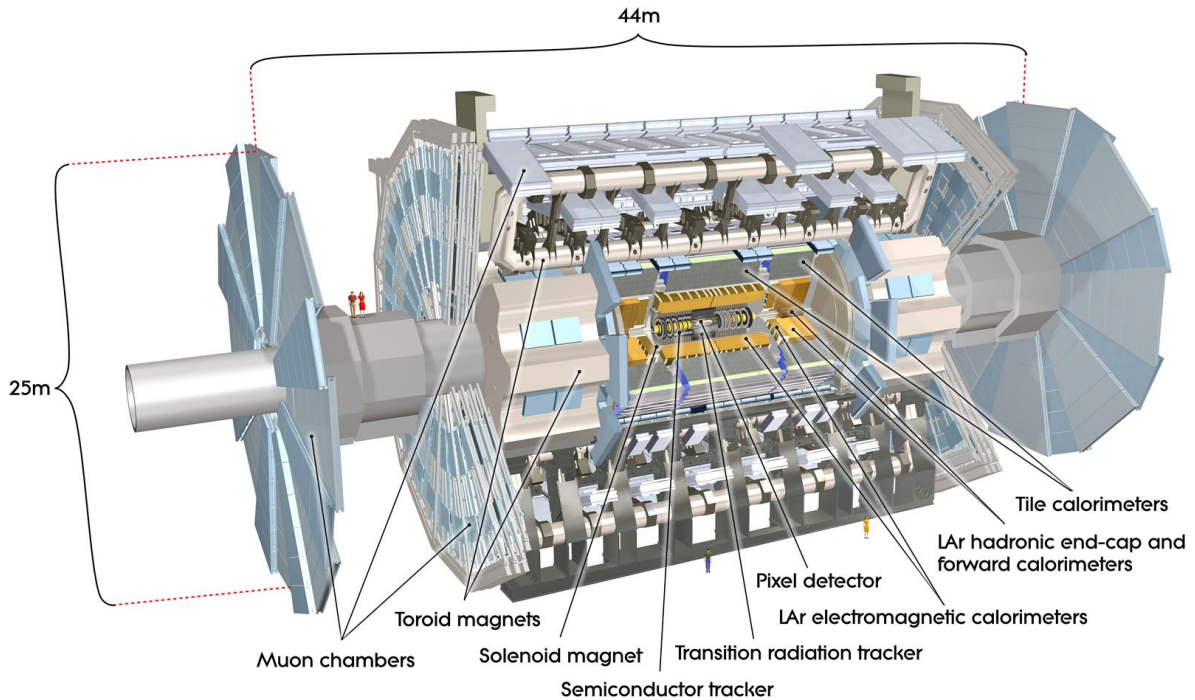


Figure 3.5.: Depiction of the ATLAS detector. It shows the dimensions of the entire detector with humans to scale. In the center the ID is illustrated, surrounded by the yellow LAr calorimeters, embedded in the tile calorimeters. The outer layer shows the large toroid magnets and muon chambers [25].

A more common and convenient way describing particle trajectories are angular coordinates. The azimuthal angle ϕ lies in the x - y -plane, while the polar angle θ is measured from the z -axis. Instead of θ often the pseudorapidity

$$\eta = -\ln \tan \frac{\theta}{2}$$

is used to describe particle trajectories. It has the advantage of being approximately equal to the rapidity $y = \tanh \frac{p_z}{E}$ in the limit $p \gg m$ and $\theta \gg \frac{1}{\gamma}$ [3]. Differences in rapidity (and therefore in the limit equivalently in pseudorapidity) are invariant under boosts in the z -direction.

3.2.2. Magnet system

To detect and determine the charge of particles traveling through the detector several magnetic fields are employed. If the direction of the particle and the magnetic field is known, one can infer from the direction of the deflection using the formula of the Lorentz force

$$\vec{F} = q\vec{v} \times \vec{B} \quad (3.4)$$

the sign of the charge. From the curvature of the track a momentum measurement is possible.

A major part of the tracking happens in the inner detector (see below), which is enclosed by the central solenoid (CS) providing a central field of 2 T, peaking at 2.6 T. It is surrounded by toroidal magnetic fields, provided by the barrel toroid (BT) and the two end-cap toroids (ECT), to enable momentum measurements of the muon spectrometer. The BT has a peak magnetic field of 3.9 T and the ECT peaks at 4.1 T.

3.2.3. Inner detector

The innermost layer of the ATLAS detector (ID) is comprised of three different tracking technologies. It has to provide high-precision momentum measurements with an excellent vertex resolution, while handling the high amount of tracks [27].

The current state of the detector for the next run, starting in 2015, is in the innermost part composed of three cylindrical layers of pixel detectors from the previous runs and the newly integrated innermost B-layer (IBL) [28]. These four layers provide a high spatial resolution in both dimensions and are essential for identifying short-lived particles such as b -quarks or taus by measuring a secondary vertex.

The next tracking layer consists of semiconductor trackers (SCT) aligned in eight cylindrical layers in the barrel and nine wheels in the end-caps.

The last layer of tracking detectors within the CS are the transition radiation detectors (TRT). They consist of straw detectors of 4 mm diameter used for direct tracking and detection of transition radiation photons created in the radiators of the TRT.

For the HL-LHC scenario described earlier a full replacement of the inner detector is planned. In the LOI from 2012 [27] an all-silicon design with finer granularity of the sensors and improved radiation-hardness is favored.

3.2.4. Calorimeter

The inner detector is enclosed by calorimeters measuring the energy of the produced particles. The inner electromagnetic (EM) calorimeters are absorbing light charged SM particles, most importantly electrons, positrons and photons, while the outer hadronic calorimeters absorb the strongly interacting particles.

The EM calorimeters have a special accordion-shaped geometry using lead as absorber and liquid argon (LAr) as detecting material. The barrel EM calorimeters cover a pseudorapidity range up to $|\eta| < 1.475$ and the end-caps $1.375 < |\eta| < 3.2$, where the outer wheel ($|\eta| > 2.5$) has a finer segmentation than the inner wheel to provide precision measurements.

Since the electronics on the EM calorimeters is subjected to significant radiation doses and was designed to withstand 10 years of operation at design luminosity, a complete replacement is planned including an upgrade of outdated components.

The hadronic calorimeter in the barrel consists of iron absorbers and plastic scintillators. It covers in total a range up to $|\eta| < 1.7$. The upgrade plans foresee a replacement of the readout electronics, since the trigger architecture will change and a higher granularity of the readout can be achieved.

The hadronic end-cap calorimeters (HEC) are once again LAr detectors, but in contrast to the EM calorimeters they are using copper plates as absorbers. With a range of $1.5 < |\eta| < 3.2$ they have an overlap with the tile calorimeter and the forward calorimeters (FCAL), to provide a continuous coverage.

The FCAL is also a LAr detector with copper and tungsten absorbers and extends with $3.1 < |\eta| < 4.9$ closest to the beam axis and is therefore particularly exposed to radiation. In the upgrade efforts both HEC and FCAL are subject to research and development, since the increased radiation doses in the HL-LHC scenario pose particular challenges for these high- η calorimeters.

3.2.5. Muon Spectrometer

The outermost layer of the ATLAS detector houses the muon spectrometers, which consist of three layers of detector chambers. The main types are monitored drift-tube chambers (MDT), while Cathode Strip Chambers (CSC) are used in the outer region covering $2 < |\eta| < 2.7$.

The MDTs consist of aluminum tubes filled with a mixture of 93% Ar and 7% CO₂ with a central W-Re wire. The resolution of each tube is $\approx 80 \mu\text{m}$. Each MDT consists of multiple layers of these aluminum tubes, which are built into “spacer frames” providing mechanical stability and an optical system for the monitoring of mechanical deformations.

Dedicated muon trigger chambers, the Resistive Plate Chambers in the barrel and Thin Gap Chambers in the end-cap regions, are used covering the range of $|\eta| < 2.4$. They are complementary to the precision MDTs, equipped with a sufficient time resolution to identify the exact bunch crossing producing the muons.

Like all other components the muon spectrometer will need a variety of improvements to cope with the HL-LHC scenario. In particular the trigger system will, step by step, be upgraded to match the new trigger design and help with improved trigger decisions to keep the rates caused by the muon trigger low.

3.2.6. Particle discrimination

Fig. 3.6 is a schematic representation of the principles of particle discrimination at the ATLAS detector. It shows a cross-section of the barrel with the tracks of some important particles.

- The signature left by photons is, in the simplest case, a shower in the EM calorimeter with no track in the inner detector. The discrimination can be more difficult, if a photon is converted in an electron-positron pair and thus leaves a track in the inner detector.
- An electron is identified by the track left in the inner tracking detector and the characteristic shower shape in the EM calorimeter. The curvature of the track gives besides the p_T measurement the charge, which allows the discrimination of positron and electron. Especially in events with many primary vertices it can be problematic to discriminate electrons and photons, therefore special discrimination techniques were developed.

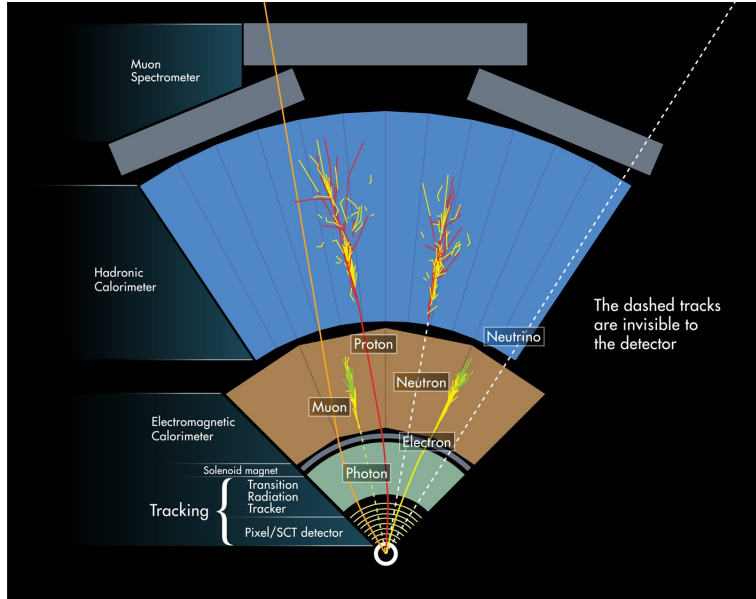


Figure 3.6.: Illustration of the signatures left by different common SM particles in the ATLAS detector [29].

- Muons are the only electrically charged particles not absorbed in the calorimeters, since they are too heavy to induce showers in the EM calorimeter and do not interact strongly. They are identified by their tracks in the muon spectrometer and the inner detector can be used to refine the measurement. Antimuons are similarly to positrons discriminated by the track curvature.
- Tau leptons decay with a probability of 35.2% leptonically³ and are difficult to distinguish from primary electrons and muons. Easier to detect are hadronic decays of tau leptons. Hadronizing taus leave multiple tracks in the inner detector and are absorbed in characteristic shower shapes in the calorimeters. The exact shower shape depends on the particular decay mode. This signature needs to be discriminated from jets produced from QCD processes. This can be done by requiring low track multiplicities in a narrow cone and is usually combined with the shower shape in a multivariate discrimination variable.
- Protons and neutrons are strongly interacting and shower therefore in the hadronic calorimeters. Since a neutron does not react electromagnetically, there are in contrast to the proton no tracks in inner detector and EM calorimeter.
- There are many processes, which produce or contain quarks and gluons. These particles hadronize in the detector and build up large showers in the hadronic calorimeter and are classified as jets. There are sophisticated jet reconstruction algorithms, as e.g. described in [30].
- An important kind of jets are those originating from b -quarks, usually called b -jets. These b -jets are important to identify top-quarks, since the principal decay mode

³via electron or muon in the case of τ^- , resp. positron or antimuon in the case of τ^+ .

of a top-quark is a W boson and a b -quark. Besides kinematic discrimination due to the higher b -quark mass (in comparison to lighter quarks) the most useful property of b -quarks, regarding discrimination, is the relatively long decay length of $c\tau \approx 450 \mu\text{m}$. With the inner detector a separated secondary vertex can be determined and the b -jet “tagged”.

- For the only weakly interacting neutrinos the detector volume is much too small to undergo reactions, which could be detected. Since the initial momentum and energy in the transverse x - y plane is known to be zero, the involvement of neutrinos can be inferred from missing transverse energy (\cancel{E}_T) in the sum of all visible⁴ transverse energy.

3.2.7. Trigger system

At the designed performance LHC will deliver bunch crossings at 40 MHz (at 25 ns bunch spacing). This rate is for several reasons too high to be recorded to disk. Each event contains 1-2 MB⁵ of data, which would amount to 40-80 PB per second, but there is no possibility to save this data to disk. From physics perspective only a small part of the interactions are of interest.

Triggers are designed to filter the events relevant for analyses and are implemented in 3 stages. Level 1 (L1) trigger is carrying out a hardware-based selection with low latency, since the data must be saved until the trigger decision has taken place. It uses fast algorithms to detect objects like taus, jets, but also \cancel{E}_T and clusters in the EM calorimeter. It reduces the rate to 70 kHz, while upgrade scenarios propose to introduce an additional level 0 trigger with an output rate of 500 kHz and a new L1 trigger with 200 kHz.

The level 2 (L2) trigger further narrows down the selection of L1 by investigating regions of interest identified by L1, now on software level, with increased granularity and more detector information. In the upgrade scenario these tasks will partly be done by the new L1 trigger, which will be able to access more detailed detector information, and partly by the high level trigger (HLT).

The HLT is a processor farm which uses algorithms similar to the offline reconstruction to improve the rejection. At HL-LHC the HLT will need an improved set of algorithms to select as much events of interest as possible, while keeping the recording rate at a low enough limit.

3.2.8. Pile-up

An important effect at high-luminosity colliders is the so-called pile-up. It describes additional collisions taking place or being detected during the interaction of interest [31]. Since usually one only wants to record the interaction of two partons, the additional events are unwanted and one tries to correct for it.

One source of additional collisions is the so-called in-time pile-up, where in one bunch-crossing multiple proton-proton collisions are taking place. The average number of inter-

⁴In this context visible means the energy collected by the calorimeters.

⁵With increasing pile-up (cf. Sec. 3.2.8) this number will increase.

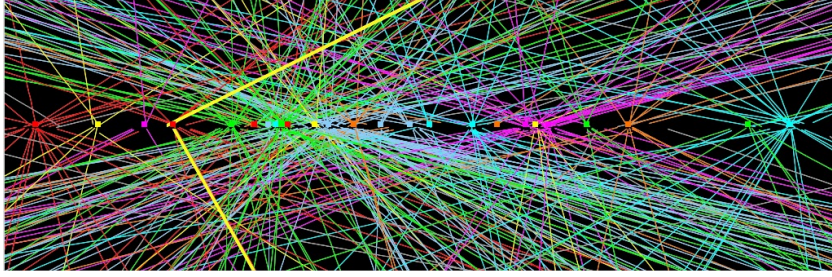


Figure 3.7.: Event recorded at ATLAS on April 15th 2012. It shows a high-pile-up environment with many reconstructed interaction vertices [32].

actions per bunch crossing $\langle\mu\rangle$ was about 21 at 8 TeV (cf. Fig. 3.8), while at the design luminosity of HL-LHC $\langle\mu\rangle = 140$ is expected. To isolate the event of interest the primary vertices of the interactions are reconstructed and tracks pointing to the unwanted primary vertices are discarded. A similar strategy is used for the calorimeters, but the pointing is considerably less precise. All contributions not removed will deteriorate the resolution of the detector. The loss of calorimeter resolution will be of importance in the reconstruction of \cancel{E}_T in the HL-LHC scenario.

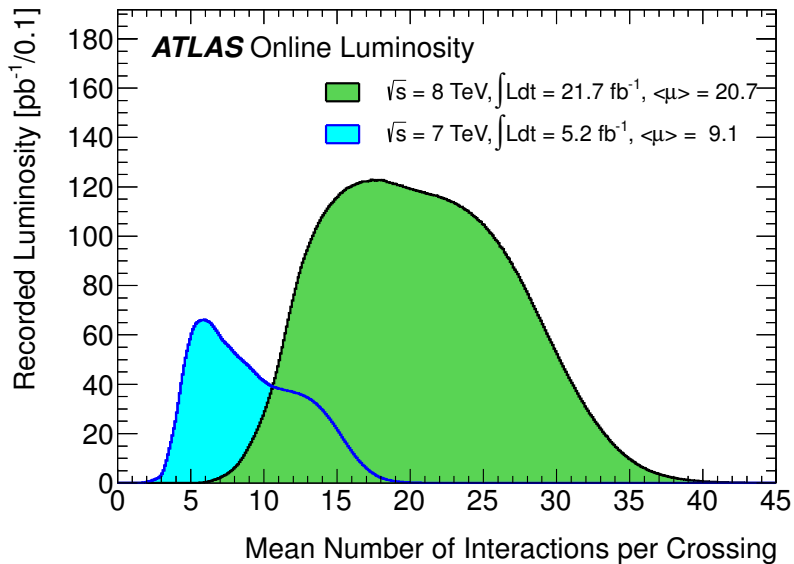


Figure 3.8.: Average number of interactions per bunch-crossing $\langle\mu\rangle$ at the ATLAS detector. The cyan shape shows the first run at 7 TeV center-of-mass energy in 2011 and the green area the run at 8 TeV in 2012 [33].

A detector-dependent component is the so-called out-of-time pile-up, e.g. the EM calorimeter has a drift time of 400 ns. Therefore collisions from bunch crossings before and after the interaction of interest may also give contributions to the calorimeter measurement and increase the noise. With decreasing bunch spacing from 50 ns to 25 ns the out-of-time pile-up contribution will increase.

An indirect influence is the pile-up from the cavern background. During operation of

LHC neutrons and photons are created in the ATLAS cavern. These particles induce random signals especially in the muon spectrometers. Dedicated shieldings are installed on the muon chambers to reduce the background.

4. Monte Carlo generated samples

An important ingredient of experiments in a variety of fields in physics are Monte Carlo (MC) simulations. They are often used to model distributions of theoretical expectations. This enables to form predictions and to verify these models with experiments.

At particle colliders, such as the LHC, MC simulations are used to simulate samples containing SM events to e.g. estimate the background in the signal region or to simulate the SUSY signal, which is used to optimize the signal region and to calculate the expected sensitivity.

The presented analysis is based on MC only, therefore an overview over MC samples and their handling in general is given. Afterwards the samples being used in this analysis are discussed with a detailed look on some of the generator level filters of the available samples.

4.1. Monte Carlo event generation

Using a simplified approach a MC generator can be summarized in the following steps [34].

The theoretical description of the hard process can be done by deriving the Feynman amplitude of the corresponding Feynman diagrams. Using the Feynman amplitude the differential cross-section of the process can be calculated.

The differential cross-section is now used as the probability distribution for the particles in the phase-space. The phase-space is the room spanned by all degrees of freedom, usually given by the four-momenta of the emanating particles. A scan through the phase-space yields the infinitesimal cross-sections at every point, which is called sampling.

A MC generator then creates events at points all over the phase-space. The distribution of events is chosen, such that the previous sampling is recreated. These events should in principle have the same particle content and kinematics as events obtained in the scattering process of a real experiment.

In reality however there are some difficulties to be considered. To describe the Feynman amplitude of a real process many corrections have to be taken into account. There is initial and final state radiation and loops within the diagrams, which can be calculated incorporating higher order diagrams. Since each higher order diagram complicates the calculations additionally, they can only be included up to a certain order, due to the limited computing power.

Another issue MC generators have to address is that e.g. quarks are known to hadronize after the hard interaction has taken place, due to the color charge they carry. The confinement forbids particles to form colorful states and in order to neutralize quarks other color carrying particles are created in so-called hadronization showers. MC generators

incorporate dedicated algorithms for hadronization showers, which are usually treated as separate part of the calculation. The advantage of the showering algorithms is that they are (almost) fully efficient. In the hard process many events are tried out and discarded until one is found, which fits the distribution to recreate and fulfills the filter requirements. This is rather inefficient, but since the showering works for almost all events without the need to discard events it can be applied after the generation of the hard process and therefore save computing time.

4.2. Monte Carlo sample handling

For the selection of MC samples a number of considerations have to be done. In the following the need of filters and the determination of the overall scaling factors for this analysis is highlighted.

4.2.1. Filters on generator level

The generation of MC events is a time-consuming task. In order to get maximal gain from the produced events, filter requirements are often applied. These help to limit the generation of events to only those, which will be used in the analyses. In many cases there are cuts e.g. on \cancel{E}_T or momenta of particles, which are mandatory for analyses and can therefore be applied beforehand. The selected filter requirements are then implemented early in the event generation (generator level) to speed up the sample production. Events which would not fulfill the filter requirement are already discarded before the full event generation is carried out.

Staying with the example of the \cancel{E}_T filter, the information of all visible particles would be needed for the calculation of the true \cancel{E}_T of an event. To decrease the time needed for the MC production, a filter on a variable already available on generator level is used. In the case of \cancel{E}_T this could be variables, such as the sum of p_T of the neutrinos or p_T of the W boson, since the neutrinos are the primary source of \cancel{E}_T and the p_T of the W boson limits the p_T of the produced neutrino. Both filter requirements are related to the true \cancel{E}_T , but usually they will not match the exact value.

A filter efficiency is calculated, which is the fraction of the number of events, where a complete event generation was carried out, over the number of all considered events. It is used as a correction to the cross-section of the process under consideration, since not the full phase-space is sampled.

4.2.2. Scaling

To get an idea of the statistics of a MC sample, an integrated luminosity can be calculated. The calculation is done as if each MC event would correspond to one event recorded in the experiment. Therefore the integrated luminosity of a MC sample is given by the ratio of the number of generated events N and the cross-section of the underlying process σ . With the filter efficiency ϵ (1, if no filter requirement is applied) and the factor k , which is a correction factor, introduced to describe next-to-leading order (NLO) effects, the full expression for the integrated luminosity of the MC sample

can be formulated:

$$L_{MC} = \frac{N}{\epsilon\sigma k} \quad (4.1)$$

To be able to perform an analysis at 3000 fb^{-1} the samples need to be scaled. Samples with a higher L_{MC} than 3000 fb^{-1} are scaled down and one event in the experiment is represented by more than one MC event, while in the opposite case the samples get scaled up and one MC event represents more than one event on data. This especially becomes a problem, when going to low event numbers in the signal region, since the modeling of the process becomes very unreliable.

A weight of

$$W = \frac{3000 \text{ fb}^{-1}}{L_{MC}}$$

is applied to all samples according to their integrated luminosities. These luminosities and the corresponding weights are given for all samples in appendix D (for the weight-correction of the signal samples cf. Sec. 4.4).

4.3. Background processes included in the analysis

To determine the contribution of background events in the analysis a number of background processes have been taken into consideration and corresponding MC samples were used. These samples are presented below with their most important properties and thereafter an analysis regarding the generator level filter of two groups of samples is explored in more detail.

4.3.1. Diboson

A set of samples including processes with two vector bosons (W , Z), resp. one Higgs and one vector boson, was used in this analysis.

- The process Wh is very similar to the signal process with the exception of missing two $\tilde{\chi}_1^0$. It is generated with PYTHIA8 [35] and filtered on two hadronically decaying taus.
- Because of its similar signature WZ is another candidate for background events. If the Z boson decays to two taus, the event topology will be close to signal-like and dedicated discrimination cuts will be necessary. WZ events are generated with the event generator SHERPA [36] and the sample is filtered on generator level on the sum of the p_T of all neutrinos $\sum_i p_T(\nu_i) > 50 \text{ GeV}$. To cope with the high production cross-section and keep at the same time the number of events to be generated in an acceptable amount, the sample is also filtered on three leptons, where the leading lepton has $p_T > 25 \text{ GeV}$, and both sub-leading leptons $p_T > 10 \text{ GeV}$. Since these cuts are later surpassed by the analysis cuts, the sample can be used with no other precautions.
- ZZ processes are important, if one Z boson decays via taus. The other Z can decay to two light leptons, where one of the leptons is not reconstructed or discarded in

the overlap removals, or decay hadronically with a jet reconstructed as an electron. The sample is generated with PYTHIA8 and a filter on $p_T > 10$ GeV and $|\eta| < 2.8$ of one of the light leptons is applied, but also these values are within the later applied object definitions.

- Events from WW processes can enter the analysis, if both W s decay leptonically (e, μ, τ) and one jet is reconstructed as electron or tau. The sample is generated with HERWIG [37] and no further filter requirements are applied.

4.3.2. Triboson

In a similar way as the Diboson processes, samples including three vector bosons are considered. All samples are listed below and filtered to three or more leptons (e, μ, τ), where in the cases of four leptons one will have to be not reconstructed or lost in the overlap removals to pass the channel definition:

$$WWW \rightarrow l\nu l\nu l\nu, \quad ZWW \rightarrow ll l\nu l\nu, \quad ZZZ \rightarrow ll ll \nu\nu$$

All three samples are generated with MADGRAPH PYTHIA [38] and no other filter requirements are applied.

4.3.3. Top-antitop

Top-antitop quark ($t\bar{t}$) processes have a signature of two W bosons and two b -jets. The W bosons can decay leptonically, while in the decay-chain of b -quarks light leptons can arise or a jet may be misidentified as tau or electron. The $t\bar{t}$ samples are split up by sub-processes and simulated with SHERPA. They have generator cuts on \cancel{E}_T up to 160 GeV, which will be discussed in detail in Sec. 4.3.6.

$t\bar{t}$ in combination with vector bosons ($t\bar{t} + V$) has a lower cross-section, but the additional vector boson can give rise to a light lepton or a hadronically decaying tau. These samples have no filters applied and are produced with MADGRAPH PYTHIA.

4.3.4. Z with jets

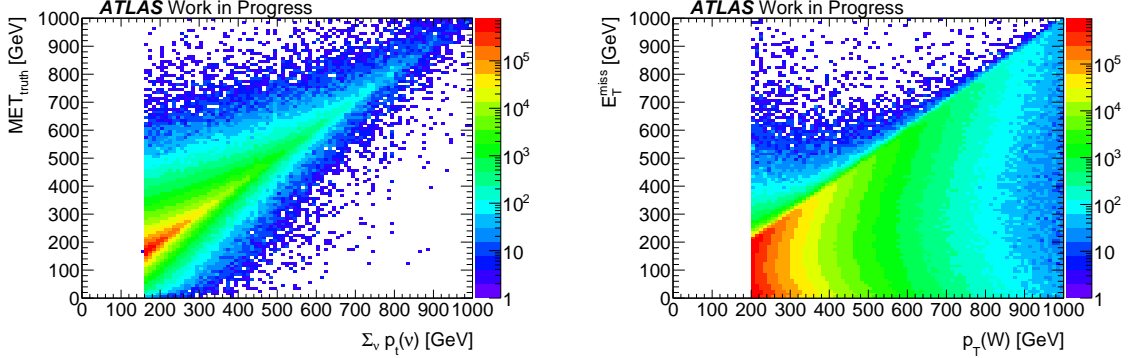
Another process which is important at the LHC are Z bosons in combination with jets. A Z boson can easily give rise to a pair of hadronically decaying taus and, as before, the jets can be misidentified as electrons or taus. The samples are split up according to the different decay channels of the Z boson and the number of additional jets, which is limited to a maximum of 5. The event generation is done with ALPGENJIMMY [39].

4.3.5. W with jets

The last process considered is W bosons in combination with jets. Because of the large cross-section it has to be taken into account, but it differs from the other backgrounds since the W boson can only give rise to one lepton. Both other leptons have to arise from secondary processes or misidentified jets. The samples are split up by decay mode of the W boson and are generated with SHERPA. They have a rather high \cancel{E}_T filter on generator level applied, which also will be explained in detail in Sec. 4.3.6.

4.3.6. Generator level filters and resulting true \cancel{E}_T cuts

Since the samples for the processes $t\bar{t}$ and W with jets were only available with cuts on different generator variables related to a rather high \cancel{E}_T cut, a dedicated analysis was carried out to determine the corresponding \cancel{E}_T cut in the following analysis.



- (a) Correlation of the sum of the p_T of all neutrinos in the initial state and the true \cancel{E}_T . Shown is the $t\bar{t}$ sample with one W boson decaying hadronically and the other one to a hadronically decaying tau. This sample has a generator cut of 160 GeV. The single non-zero bin below the generator cut contains one single event.
- (b) Correlation of the sum of the p_T of the W boson in the initial state and the true \cancel{E}_T . Shown is the W with jets sample, where the W boson decays to an electron and a neutrino. A generator cut on $p_T(W) > 200$ GeV was used in the production.

Figure 4.1.: Correlation of generator cut variables and true \cancel{E}_T for the two samples with the highest resulting true \cancel{E}_T cuts.

The samples for the $t\bar{t}$ processes are filtered on generator level on the sum of the transverse momenta of all neutrinos. The correlation of this generator variable and the true \cancel{E}_T used in the analysis is shown in Fig. 4.1a. One can see the filter requirement of $\sum_i p_T(\nu_i) > 160$ GeV. Unfortunately the true \cancel{E}_T of the MC sample is not closely correlated with $\sum_i p_T(\nu_i)$. This means that a cut on the true $\cancel{E}_T = 160$ GeV would lead to a substantial underestimation of the background.

To keep the problem of underestimated backgrounds at bay, a conservative estimate on the missed background events is carried out. Starting from Fig. 4.1a, the bin directly above the generator cut (in this case 160–170 GeV) is read out and regarded as a function of the true \cancel{E}_T . The conservative assumption is then, that all bins left of the selected bin (white stripe) are shifted to lower true \cancel{E}_T values. This is justified when looking at the correlation plot, where the events are distributed around the diagonal. Therefore the selected line of bins serves as an upper limit for the bins left of it and is used for the estimation of missed events.

For the estimation of the lowest possible cut on the true \cancel{E}_T a scan over the whole true \cancel{E}_T range, in the mentioned line of bins above the generator cut, in 10 GeV steps is performed. For each cut value on the true \cancel{E}_T the fraction of events with true \cancel{E}_T higher than the cut over all events in this line of bins is calculated. If the fraction is below 5%

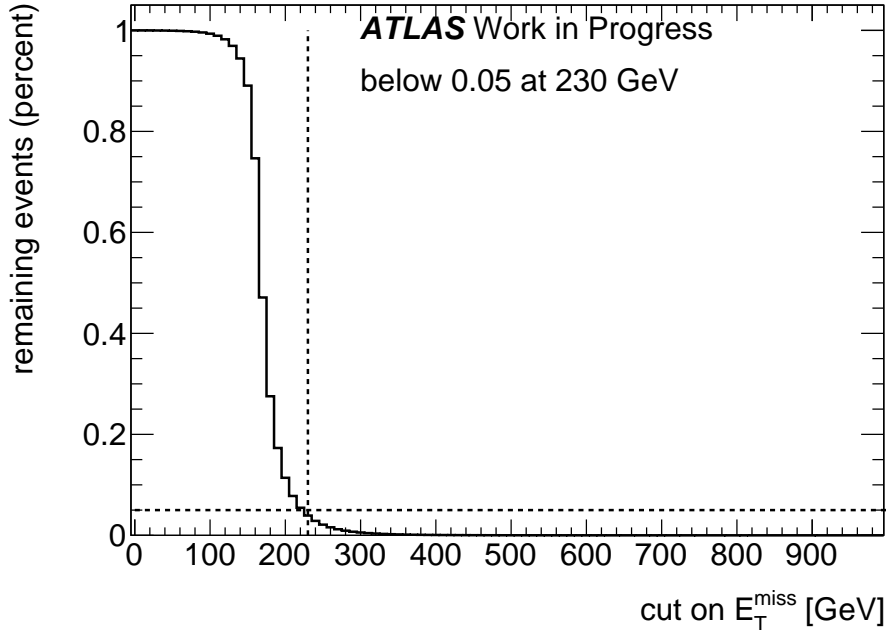


Figure 4.2.: Scan over true \cancel{E}_T cuts in 10 GeV steps. Shown is the fraction of events above the cut over all events. The horizontal dashed line marks the 0.05 line and the vertical line is put on the lowest cut at which less than 5% of the events are above the cut. The sample shown is the sub-process of $t\bar{t}$ from Fig. 4.1a

it is accepted as sufficient. Fig. 4.2 shows the scan for the $t\bar{t}$ sample already presented in Fig. 4.1a.

This test is done for all $t\bar{t}$ samples with generator level \cancel{E}_T filters and the corresponding plots are listed in appendix C, Fig. C.1. The list of generator cuts and the advised cuts on the true \cancel{E}_T in Tab. 4.1 shows that the resulting values for the proposed \cancel{E}_T cuts are not directly dependent on the generator cuts, but strongly dependent on the underlying sub-process. The correlation between $\sum_i p_T(\nu_i)$ and the true \cancel{E}_T gets worse with a higher numbers of jets in the sub-process. Fig. B.2 in appendix B shows the correlation plots for all remaining $t\bar{t}$ samples.

sub-process	gen. cut	true \cancel{E}_T cut
$W \rightarrow l, W \rightarrow l$	120 GeV	140 GeV
$W \rightarrow l, W \rightarrow \tau_{\text{had}}$	120 GeV	160 GeV
$W \rightarrow \tau_{\text{lep}}, W \text{ had.}$	120 GeV	210 GeV
$W \text{ had.}, W \rightarrow l$	160 GeV	190 GeV
$W \text{ had.}, W \rightarrow \tau_{\text{had}}$	160 GeV	230 GeV

Table 4.1.: $t\bar{t}$ generator cuts and corresponding true \cancel{E}_T cut for the differently filtered sub-processes.

In the case of the process W with jets a different generator cut is used. A cut on $p_T(W)$ is applied and in Fig. 4.1b the correlation with the true \cancel{E}_T is shown in the sub-process with the W boson decaying to an electron and the corresponding neutrino (cf. also Fig. B.1 in App. B). From this plot one can easily see that most of the events are below the diagonal and therefore a truth \cancel{E}_T cut can be applied at a just slightly higher value without missing much of the background. All three W with jets samples are filtered with $p_T(W) > 200$ GeV and the same thresholds as in the $t\bar{t}$ case (cf. also Fig. C.2 in appendix C) are applied. For all three decay channels (e, μ, τ) a cut on the true \cancel{E}_T at 210 GeV is fulfilling the requirements (cf Tab. 4.2).

subprocess	gen. cut	true \cancel{E}_T cut
$W \rightarrow e$	200 GeV	210 GeV
$W \rightarrow \mu$	200 GeV	210 GeV
$W \rightarrow \tau$	200 GeV	210 GeV

Table 4.2.: W with jets generator filter requirements and resulting true \cancel{E}_T cuts for all sub-processes.

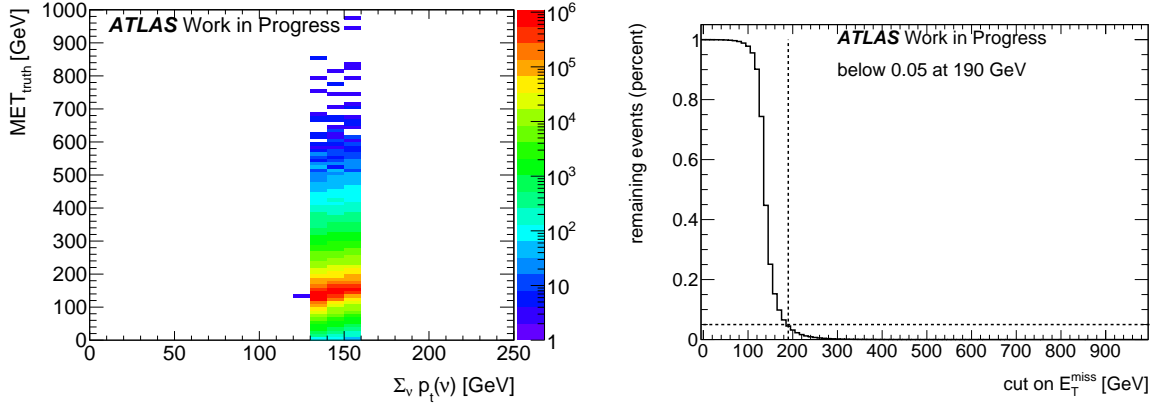
Since later in the analysis the true \cancel{E}_T is smeared (cf. Sec. 5.2), i.e. is varied according to a Gaussian with width of about 60 GeV, an additional safety margin of 120 GeV is introduced. In total the applied analysis cut on \cancel{E}_T would have to be at least 350 GeV, since the sample with the highest cut has a true \cancel{E}_T cut of 230 GeV.

4.3.7. Production of a new MC slice

Looking at the tables 4.1 and 4.2 one can see that all but one sample have a resulting cut on the true \cancel{E}_T less than or equal to 210 GeV. To lower the \cancel{E}_T cut with reasonable effort, a new slice with MC events with a generator cut of $130 \text{ GeV} < \sum_i p_T(\nu_i) < 160 \text{ GeV}$ was generated.

An estimation of the cross-section for the new slice was obtained by generating a small sample with a generator cut of 130–160 GeV. With a test sample of 50 events a cross-section of about 2.7 pb was estimated. Since the existing $t\bar{t}$ samples had an integrated luminosity of about 1000 fb^{-1} , the new sample was targeted to have a similar amount of statistics. Using Eq. 4.1 a conservative estimate of $3 \cdot 10^6$ events was calculated to achieve about 1000 fb^{-1} of integrated luminosity.

The produced slice has a cross-section of 2.98 pb, which is about 10% higher than the estimate. A corresponding integrated luminosity of $1.0 \cdot 10^3 \text{ fb}^{-1}$ could be calculated, showing that the sample has the desired statistics. Fig. 4.3 shows the correlation plot and the scan for different true \cancel{E}_T cuts, where a new lower limit of 190 GeV on the true \cancel{E}_T can be seen. The result of the production of the new MC slice is that the extension allows to lower the true \cancel{E}_T cut of the analysis to 210 GeV instead of 230 GeV, resp. the smeared \cancel{E}_T cut to 330 GeV instead of 350 GeV.



- (a) Correlation of $\Sigma_i p_T(\nu_i)$ and true \cancel{E}_T for the newly produced slice. It extends the existing sample down to a generator cut of 130 GeV. The single non-zero bin below the generator cut contains one single event.
- (b) Scan over true \cancel{E}_T cuts in 10 GeV steps. Shown is the fraction of events above the cut over all events. The horizontal dashed line marks the 5% line and the vertical line is put on the lowest cut at which less than 5% of the events are above the cut.

Figure 4.3.: Correlation and scan plots for the low- $\Sigma_i p_T(\nu_i)$ extension of the $t\bar{t}$ sample in the sub-process, where one W boson decays hadronically and the other W boson is decaying to a hadronically decaying tau.

4.4. Signal Monte Carlo samples

Signal samples were available for the decay channel $\tilde{\chi}_1^\pm \tilde{\chi}_2^0 \rightarrow W \tilde{\chi}_1^0 h \tilde{\chi}_1^0$. Only on-shell Higgs bosons were simulated. Filter requirements are applied to enhance the number of MC events useful for analyses. A filter on exactly three leptons (e , μ , τ) is applied, allowing to do e.g. a 3 light lepton search or as in this case a 1 light lepton and 2 τ search. All leptons are required to be within $|\eta| < 2.7$, where the light leptons need a $p_T > 5$ GeV and the taus a visible $p_T > 15$ GeV.

The signal MC samples are produced for different combinations of $\tilde{\chi}_1^\pm$ and $\tilde{\chi}_1^0$ masses, where the masses of $\tilde{\chi}_1^\pm$ and $\tilde{\chi}_2^0$ are assumed to be degenerate. For convenience $m_{\tilde{\chi}_1^\pm}$ will in the following be used synonymous with $m_{\tilde{\chi}_2^0}$.

The range for $m_{\tilde{\chi}_1^\pm}$ is varied from 200 GeV up to 1500 GeV in steps of 100 GeV. The spacing $m_{\tilde{\chi}_2^0} - m_{\tilde{\chi}_1^0} \geq 150$ GeV is used to allow a decay of the $\tilde{\chi}_2^0$ to h and $\tilde{\chi}_1^0$. The range for $m_{\tilde{\chi}_1^0}$ is therefore 0 GeV to a maximum of 1350 GeV in steps of 100 GeV, where the last step below the maximal mass is 50 GeV.

In the following expressions of the form (200,0) will, for the sake of readability, always refer to mass points in the $\tilde{\chi}_1^\pm$ - $\tilde{\chi}_1^0$ grid with the meaning:

$$(m_{\tilde{\chi}_1^\pm} = 200 \text{ GeV}, m_{\tilde{\chi}_1^0} = 0 \text{ GeV})$$

Signal samples are additionally down-weighted, since some of the decay channels of the Higgs boson were suppressed in the MC generation and therefore the signal samples are overestimated. The suppressed decay channels have, according to [40], the branching ratios listed in Tab. 4.3.

sub-process	branching ratio	sub-process	branching ratio
$h \rightarrow b\bar{b}$	0.577	$h \rightarrow gg$	0.0857
$h \rightarrow c\bar{c}$	0.0291	$h \rightarrow \gamma\gamma$	0.00228

Table 4.3.: Not simulated sub-processes with branching ratios.

These branching ratios were set to 0, therefore a re-weighting factor has to be applied. Adding up these branching ratios the actually generated fraction can be calculated, which is then applied as down-weighting factor:

$$1 - (0.577 + 0.0291 + 0.0857 + 0.00228) = 0.30592$$

The sub-processes listed in Tab. 4.4 were in contrast simulated (with the “real” branching ratios as obtained from theory) [40].

sub-process	branching ratio	sub-process	branching ratio
$h \rightarrow WW$	0.215	$h \rightarrow \mu\mu$	0.00022
$h \rightarrow ZZ$	0.0264	$h \rightarrow \tau\tau$	0.0632
$h \rightarrow Z\gamma$	0.00154		

Table 4.4.: Simulated sub-processes with branching ratios.

Therefore about 20 % of all generated events are $h \rightarrow \tau\tau$ events. The full list of samples with their corresponding weights can be found in appendix D.

4.5. Truth information

The advantage of using only MC samples is that the so-called truth information can be accessed. MC generators do not only output the raw event, but also can include information about decay chains and production processes. It is tempting to use this information, but it has to be taken into account, that not all of this information is corresponding to physical reality. In the case of interfering particles it isn’t even theoretically possible to know which particle was exchanged. MC generators may use intermediate particles as auxiliary entities, which do not correspond to actual physical particles.

In order to discern the internally used particles from the ones in final states, each particle is tagged with a so-called MC status. There are a variety of statuses, partly even depending on the generator, but particles with a status of 1,2 and 4 are generally considered being final state particles.

Internally the particles are numbered to indicate of which kind a particle is. The official numbering scheme is documented in [41]. The PDG-ID of τ^- is, e.g. 15, while the IDs of antiparticles are denoted with a minus sign. This is useful to directly address particles.

5. Analysis

This analysis is solely based on MC samples, simulated for proton-proton collisions at 14 TeV center-of-mass energy. These MC samples have no detector reconstruction algorithms applied. They are only a simulation of the interaction taking place at the collision point and include information about the produced particles. To be able to estimate the sensitivity of an analysis carried out at the ATLAS detector with 3000 fb⁻¹ of data the response of the detector has in addition to be taken into account.

This chapter lists the preparation steps necessary to emulate an analysis with data recorded by the detector. They are based on the recommendations of the ATLAS collaboration for the European Strategy for Particle Physics described in [42] and [43].

5.1. Object selection

Carrying out the analysis on truth level (cf. Sec. 4.5 on the “true” information in MC samples) at first the object selection from the provided MC information is performed. The light leptons and jets are taken directly from the according MC containers. Container refers in this context to collections of objects, like electrons or jets, which are provided in the derived MC samples. These containers include all final state particles of one type.

Hadronically decaying taus were identified using the MC information on truth level. Requiring a PDG-ID of ± 15 ensures that only taus are selected. A MC status of 2 selects all particles in final states. Since an analysis of this type can not discriminate prompt light leptons from light leptons from tau decays, all tau leptons decaying to light leptons are removed from the tau container, such that only hadronically decaying taus remain. The p_T of the escaping neutrino is subtracted to get the visible p_T of the hadronically decaying tau. In the following “tau” will refer to hadronically decaying taus.

5.2. Reconstruction efficiencies and energy smearing

The particles produced in the underlying physical process will not always be reconstructed in the detector. Having no simulation of the detector response available, a parameterized response following the recommendations for the European Strategy was applied instead.

To ensure that the detector is able to reconstruct the objects, an object dependent acceptance cut is carried out. Due to the symmetrical structure of the detector it is sufficient only to apply $|\eta|$ criteria.

It is possible that particles are not reconstructed by the detector. An important reason for failing reconstruction are the algorithms used for particle discrimination. Several cuts on discrimination variables are applied on the event information recorded by the

detector. Since the rate of false positive object reconstructions should be kept low, a trade-off with the identification sensitivity has to be done.

The finite resolution of the calorimeters and the tracking systems is taken into account by varying the particle energies and the \cancel{E}_T . This variation is called smearing. The resolution may depend on different variables and is given as width of a Gaussian distribution. For each object a value with the probability of the according Gaussian is selected and shifted by this value.

5.2.1. Electrons

Anticipating the object definition cut only electrons with $p_T > 10$ GeV are selected. Only electrons in the pseudo-rapidity range $|\eta| < 2.47$, where the finer segmented EM calorimeters are located, are considered in order to achieve the best energy resolution. According to the European Strategy functions an energy-dependent reconstruction efficiency is applied [43]:

$$\epsilon_e = 0.97 - 0.103 \exp\left(1 - \frac{E}{15 \text{ GeV}}\right)$$

The energy smearing is based on the detector performance of run 2 and, while also being energy-dependent, split into two $|\eta|$ areas:

$$\begin{aligned} \sigma(\text{GeV}) &= \sqrt{0.3^2 + \left(0.1 * \sqrt{E(\text{GeV})}\right)^2 + (0.01 * E(\text{GeV}))^2} && \text{for } |\eta| < 1.4 \\ \sigma(\text{GeV}) &= \sqrt{0.3^2 + \left(0.15 * \sqrt{E(\text{GeV})}\right)^2 + (0.015 * E(\text{GeV}))^2} && \text{for } 1.4 < |\eta| < 2.47 \end{aligned}$$

5.2.2. Muons

Muons enter the analysis with a $p_T > 10$ GeV and $|\eta| < 2.4$. The reconstruction efficiency is energy-independent, but split into the pseudorapidity regions $|\eta| < 0.1$, where servicing shafts are located and the efficiency is assumed to be 54%, and the remaining available region $0.1 < |\eta| < 2.4$ with a constant efficiency of 97% over the whole range [42].

The muon smearing functions are composed of the muon spectrometer resolution, assumed to be still valid in future LHC operations and the inner detector (ID) resolution adapted for an improved resolution due to the upgrades.

The parametrization of the ID resolution is given by

$$\sigma_{\text{ID}} = p_T \times \sqrt{a_1^2 + (a_2 \times p_T)^2}$$

with the $|\eta|$ -dependent values a_1 and a_2 listed in appendix Tab. A.1.

The resolution of the MS is parameterized as

$$\sigma_{\text{MS}} = p_T \times \sqrt{\left(\frac{b_0}{p_T}\right)^2 + b_1^2 + (b_2 \times p_T)^2}$$

with the values for b_0 , b_1 and b_2 given by:

	b_0	b_1	b_2
$ \eta < 1.05$	0.24	0.02676	0.00012
$ \eta > 1.05$	0.00	0.03880	0.00016

The combination of both is calculated as

$$\sigma_{\text{CB}} = \frac{\sigma_{\text{ID}} \sigma_{\text{MS}}}{\sqrt{\sigma_{\text{ID}}^2 + \sigma_{\text{MS}}^2}}$$

giving the width of the muon p_{T} smearing.

5.2.3. Taus

Taus are included in the analysis if they are within $|\eta| < 2.5$ and $p_{\text{T}} > 20$ GeV. In this range, the reconstruction efficiency is assumed to be independent of energy and pseudo-rapidity, but dependent on the number of charged particles in the hadronization process (n -prong). For 1-prong taus the efficiency is assumed to be at a constant value of 55% and for 3-prong taus at 50%.

Energy smearing of taus is also parameterized depending on the n -prong and the tau energy:

$$\frac{\sigma_{\tau}}{E(\text{GeV})} = 0.03 \oplus \frac{0.62}{\sqrt{E(\text{GeV})}} \quad \text{for 1-prong taus}$$

$$\frac{\sigma_{\tau}}{E(\text{GeV})} = 0.03 \oplus \frac{0.76}{\sqrt{E(\text{GeV})}} \quad \text{for 3-prong taus}$$

5.2.4. Jets

Jets are only accepted, if they are in the range $|\eta| < 4.5$ and have $p_{\text{T}} > 20$ GeV. For the energy smearing several uncertainties are taken into consideration. The noise N is given as linear function of the average number of interactions per bunch crossing $\langle \mu \rangle$ with $N = a + b \langle \mu \rangle$ and a dependence on $|\eta|$. The stochastic term S and the constant term C are independent of $\langle \mu \rangle$. The uncertainty is calculated as

$$\sigma_{\text{jet}} = \sqrt{\frac{N^2}{p_{\text{T}}^2} + \frac{S^2}{p_{\text{T}}} + C^2}$$

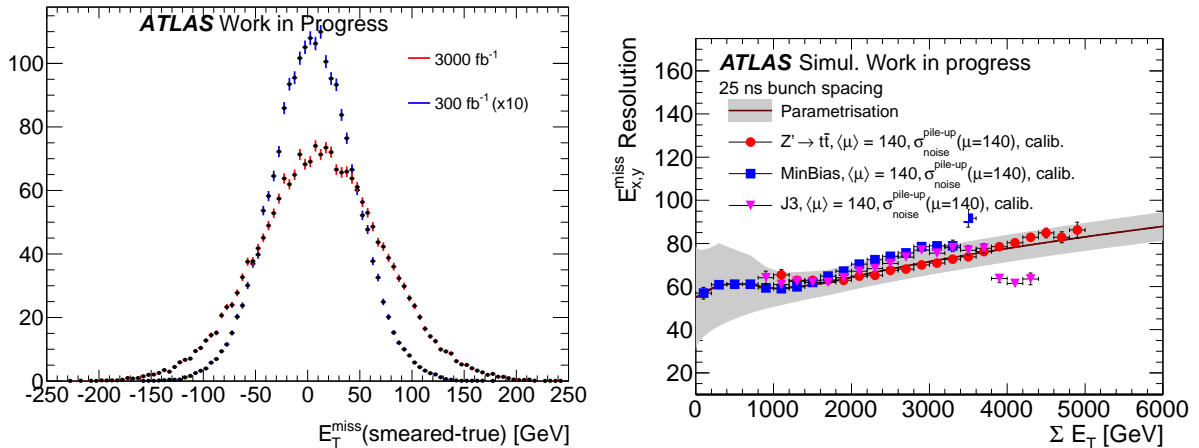
with these $|\eta|$ -dependent values

$ \eta _{\text{min}}$	$ \eta _{\text{max}}$	a	b	S	C
0	0.8	3.16	0.07	0.74	0.055
0.8	1.2	3.03	0.07	0.85	0.053
1.2	2.8	3.32	0.08	0.56	0.065
2.8	3.6	2.84	0.11	0.83	0.054

and the smearing is performed with a Gaussian distribution of width $p_{\text{T}}\sigma_{\text{jet}}$.

5.2.5. Missing transverse energy

Due to the finite resolution of the calorimeters, the reconstruction of the \cancel{E}_T will not be exact. In addition the pile-up complicates the reconstruction. Since the \cancel{E}_T can only be calculated by summing up all visible E_T , pile-up events spoil the sum and therefore degrade the detector resolution. The functions for the European Strategy also include \cancel{E}_T smearing, which is derived in dependence on $\langle\mu\rangle$ in [42].



(a) Comparison of smearing in scenarios assuming 300 fb^{-1} and 3000 fb^{-1} of integrated luminosity. Shown is the signal sample (600, 0). For the comparison the 300 fb^{-1} sample is scaled by a factor of 10. (b) \cancel{E}_T resolution for a pile-up of $\langle\mu\rangle = 140$ [42].

Figure 5.1.: \cancel{E}_T smearing from the European Strategy functions.

The impact of the different smearing functions on the \cancel{E}_T distribution is shown in Fig. 5.1a. It shows the difference between true and smeared \cancel{E}_T for a 300 fb^{-1} analysis assuming $\langle\mu\rangle = 60$ and a 3000 fb^{-1} analysis assuming $\langle\mu\rangle = 140$. A fit of a Gaussian on both distributions yields a width of 60 GeV for $\langle\mu\rangle = 140$ and 40 GeV for $\langle\mu\rangle = 60$. It should be noted that the mean of both distributions is shifted to values above 0. This is due to the fact that the \cancel{E}_T distribution is mostly falling. If in a falling distribution events are shifted in each bin in the same amount to lower and higher values, the result will be a net shift to higher values.

The resolution for \cancel{E}_T in the case of 3000 fb^{-1} with a pile-up of $\langle\mu\rangle = 140$ is shown in Fig. 5.1b. It can be seen that for lower ΣE_T values the resolution for \cancel{E}_T is about 60 GeV in accordance to the width of the Gaussian presented above.

In this analysis some of the MC samples have generator cuts which require rather high cuts on the true \cancel{E}_T (cf. Sec. 4.3.6). If the smearing is applied on these samples, events are shifted below the generator cut, but no events are shifted back. Therefore the background process is underestimated in a region of the order of the smearing above the generator cut. In order to avoid this underestimation the analysis cut has to take into account the smearing. For this analysis a conservative safety margin of two times the smearing resolution above the highest generator cut was chosen. An optimistic signal region, where the effects of smearing lead to a possible underestimation of some

background processes, with a safety margin of only one time the smearing resolution is also defined.

5.3. Overlap Removal I

Since the particles considered as reconstructed are organized in containers, it is possible, that one physical object is reconstructed in two or more different containers. Most of the misidentifications are electrons and taus additionally reconstructed in the jet container. This overlap removal is done to remove the objects which are reconstructed in multiple containers. In the next step electron and tau fakes from jets will be introduced, where only “real” jets should be used. After this step another overlap removal will be carried out, then with physically motivated cuts.

To avoid having the same simulated object appearing in different roles in the analysis, a set of ΔR requirements, the so called “overlap removal” (summarized in Table 5.1), is executed:

- If electrons are overlapping with other electrons the electron with lower E_T is discarded in order to remove electrons reconstructed twice.
- It happens that electrons leave shapes similar to jets, therefore jets within a cone of $\Delta R = 0.2$ of electrons are removed.
- Since taus are also reconstructed as jets, jets within a cone of $\Delta R = 0.2$ of taus are removed.
- Taus within a cone of $\Delta R = 0.2$ of electrons or muons are removed, since electrons and muons could also be reconstructed as taus.

considered objects	ΔR requirement	
$\Delta R_{e,e}$	< 0.05	discard lowest E_t electron
$\Delta R_{e,j}$	< 0.2	discard jet
$\Delta R_{\tau,j}$	< 0.2	discard jet
$\Delta R_{e,\tau}$	< 0.2	discard tau
$\Delta R_{\mu,\tau}$	< 0.2	discard tau

Table 5.1.: ΔR requirements applied to ensure that objects reconstructed in multiple containers are only used as one kind of object.

5.4. Fake electrons from jets

After the removal of excess objects in the first overlap removal, “fake” electrons from jets are introduced. This is necessary, since the MC samples only contain the objects produced in the interaction. During detection in the calorimeters it can however happen, that the shapes left by jets are misidentified as electrons.

To account for this effect, in this analysis the probability p of jets to be misidentified as electrons is parameterized dependent on the jet p_T :

$$p = 0.11 \exp(-0.033 \cdot p_T)$$

Since jets are reconstructed in a wider $|\eta|$ range than electrons, jets outside the reconstruction range of electrons a fake probability of 0 is assigned. With a decision based on random numbers created by the software, a jet will be ignored or added to the electron container. If a jet fakes an electron it is also kept in the jet container. It is removed with the repetition of the first overlap removal after adding the tau fakes from jets in the next step.

Since the calorimeter measurement of every object is calibrated according to the reconstructed type to optimize the energy resolution, the jets added to the electron containers need to be re-scaled in p_T . The re-scaling for the p_T of the jet is down to about 40% with a Gaussian variation of 13%-21% width as prescribed by the recommendations to the European Strategy.

5.5. Fake taus from jets

In the same way as fake electrons, jets may leave shapes similar to taus and therefore may be misidentified. The probabilities for jets faking a tau range from 0.94% down to 0.05%, once again a probability of 0 if out of tau reconstruction range.

Similar to jets faking electrons the random number based method could in principle be used for jets faking taus. From the probabilities ($< 1\%$) it can easily be concluded, that introducing fake taus based on a random number procedure leads to a rejection of many events. This especially becomes a problem, when using MC samples with an integrated luminosity lower than 3000 fb^{-1} with a process relying on fakes from jets as e.g. the $t\bar{t}$ samples. The description of the tails of distributions will be degraded and the background contribution in the signal region will be highly dependent on the random decisions at the tau faking.

In contrast to electrons from jets, the taus have a lower fake probability. It is possible that up to two fake taus are necessary to pass the signal region cut. In order to keep the number of unused events as low as possible, a re-weighting method for fake taus from jets was developed.

5.5.1. Re-weighting of events

The idea of the re-weighting method is, that in the limit of high event numbers the random number based, as well as the re-weighting based method, will produce similar distributions. This is visualized below in a simple exaggerated model.

In the random number based approach a “real” distribution, here illustrated in dark blue and cyan, will be poorly sampled in the tails, since single events with high weights, here sketched in orange, are not able to recreate the distribution:



In the case of high event numbers the individual event weights (orange boxes in this picture) get smaller and the “real” distribution can be recreated in much more detail.

In the case of the re-weighting method each event is split up according to the probability of the different combinations of tau fakes from jets, e.g. no fakes from jets or jet i faking a tau. This not only has the advantage that the distributions can be recreated more accurate, as in this picture (with the parts of events colored olive):



Also each bin might be filled with parts of different events. This is useful for the case of several signal region cuts. Each cut leaves a certain amount of background. In the case of the random number based approach this certain amount of background consists of less MC events than in the case of the re-weighting method. Consequently all following distributions will be better modeled with the re-weighting method and the analysis less susceptible to fluctuations.

Instead of throwing a die and not using the event in more than 99% of the cases (this holds for the number of background samples with one or zero real taus), the event state is saved and the following cases calculated and included with the corresponding event weight. The event state includes all particle containers, \cancel{E}_T and the event weight from the MC sample.

- The first case is that no jet is faking taus. The probability p for this case is

$$p = \prod_{i=0}^n (1 - p_i),$$

where n is the number of jets and p_i is the probability of jet i faking a tau. The remaining analysis steps, as stated below, are carried out with no taus from jets and an individual weight of

$$p \times \text{MC event weight.}$$

- For the case of one fake from jets the remaining analysis steps are repeated n times, every time using the saved state and the weight based on the individual probability. The probability, resp. the re-weighting factor, for the iteration with jet j faking a tau is given by:

$$p = p_j \prod_{\substack{i=0 \\ i \neq j}}^n (1 - p_i)$$

- For two fakes from jets all different combinations of pairs of fakes are considered and the probability reads

$$p = p_j p_k \prod_{\substack{i=0 \\ i \neq j, i \neq k \\ j < k}}^n (1 - p_i).$$

In the two fake case in total $0.5 n(n - 1)$ iterations are necessary.

- Three and more tau fakes from jets are not considered, since later on in the analysis exactly two taus are required. This means that in most of the cases these parts of the event would not enter the analysis.

Furthermore the probability, i.e. the weight, gets negligible. Recalling that the maximum probability for a jet to fake a tau is 0.94%, the maximum probability for three fakes is given by $0.0094^3 = 0.83 \cdot 10^{-6}$. Since events with three fake taus can only enter the signal region, if the third tau is lost during the second overlap removal or it is out of the range of the object definition of the taus, these events will barely contribute to the overall background estimation.

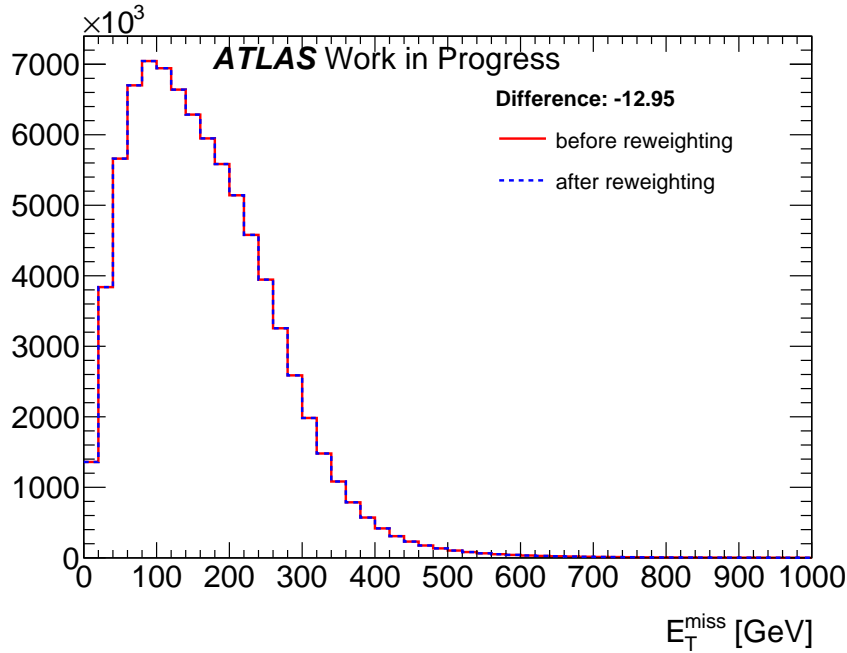


Figure 5.2.: \cancel{E}_T distributions after smearing. They are shown before and after the re-weighting procedure. The difference between the distributions is barely visible and determined to be about 13 events. Shown is the W with jets sample with the W boson decaying to an electron. It has the generator cut $p_T(W) > 200$ GeV.

Fig. 5.2 shows the \cancel{E}_T distributions before and after the re-weighting procedure. A difference in the distributions is not visible, since only about 13 events are lost with the re-weighting. This shows that the re-weighting method is able to recreate the \cancel{E}_T distribution.

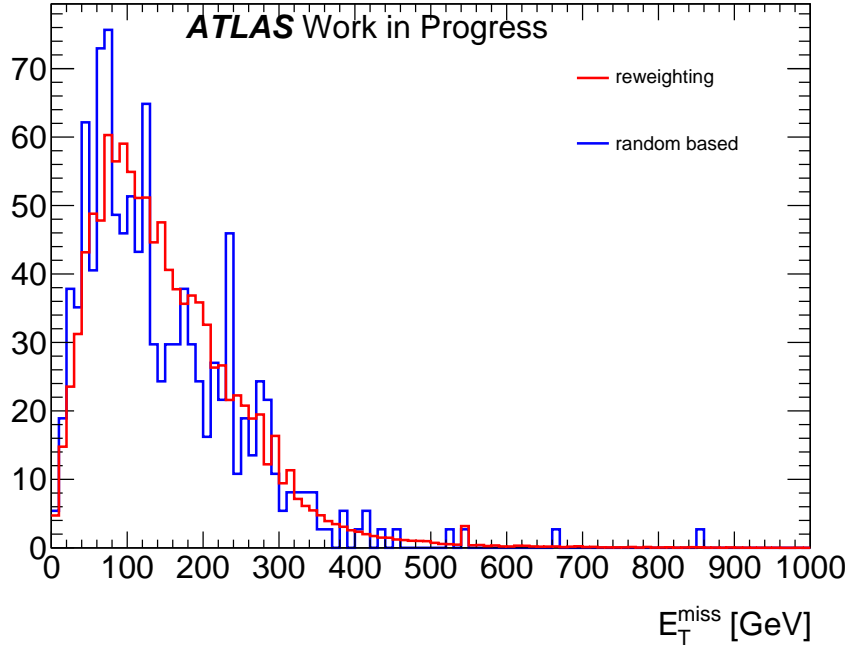


Figure 5.3.: \cancel{E}_T distributions after applying channel definition cuts with the random number based and re-weighting based approach. Shown is the W with jets sample in the decay mode with one electron. Due to the generator cuts a \cancel{E}_T cut of about 300 GeV will be needed.

The picture changes substantially if the channel definition is taken into account. Fig. 5.3 shows the comparison of the \cancel{E}_T distributions of events passing the channel definition cuts. The W with jets sample is shown, where the W boson decays to an electron. Since there are only very few taus in the original MC sample, the fakes from jets are very important. Since one of the channel definition cuts is requiring two taus, the event numbers are reduced to much lower numbers.

The shape of the curve from the re-weighting based approach is more smooth than the random number based approach. The weight of the events in the random number based case are at about 3, since the integrated luminosity of the samples is only about 1000 fb^{-1} . In the area around 400 GeV can be seen that the random number based curve consists of single events, containing only a small part of the sample information. However the curve of the re-weighting events shows in this area a much smoother behavior.

Since after re-weighting the event parts get different weights according to their probability, i.e. the number of faked taus, there are still some event parts with a weight of about 3, if no jet was faking a tau. In this case the weight is multiplied with at least $(1 - 0.0095)^n$, since 0.95% is the highest fake probability. In the case of 10 jets the weight is still at least 91% of the original weight. One of these event parts with high weights can e.g. be seen at about 540 GeV.

Since a high cut of \cancel{E}_T at around 300 GeV will be necessary, the re-weighting method will contribute more different MC events to the signal region.

5.5.2. Validation of the re-weighting method

To validate the re-weighting method additional cross-checks were devised. They show that virtually the full event weight enters the analysis and that the amount of event weight not covered corresponds to the expectation. Missing event weight is expected, since the event parts with 3 or more fake taus are not included.

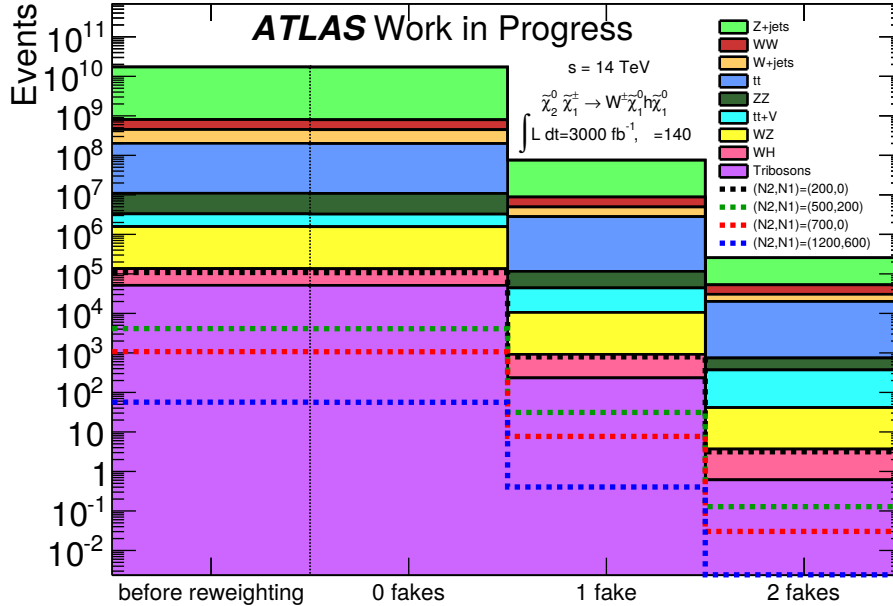


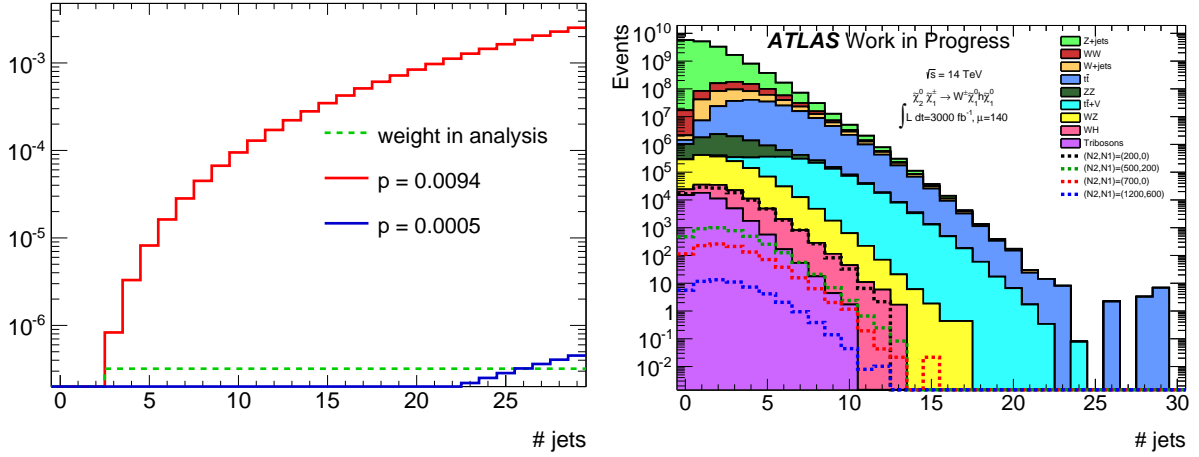
Figure 5.4.: Comparison between full event weight and event weight covered in the different re-weighting steps. The first bin shows the sum of the initial weights of the event before the re-weighting and the following bins the sums of the re-weighted events in the cases of 0, 1 or 2 fake taus.

Fig. 5.4 shows the amount of weight entering the analysis. The first bin “before reweighting” contains the sum of the initial event weight before the re-weighting procedure is done. The following bins hold the sums of event weights added for the different cases 0, 1 or 2 tau fakes. It can be seen, that the latter bins do not sum up to a bigger weight than the first one, since the sum of probabilities can not exceed 1 and therefore the weight can not increase.

One can see, that most of the event weight is covered in the zero to two fakes bins. Especially $t\bar{t}$ and the other multijet backgrounds get additional event information in the tau fake case. The difference in event weight is event information, which is completely lost and could introduce a harmful bias, but as explained above the events lost are exclusively holding 3 or more fake taus from jets and would be in most cases discarded at the application of the channel definition.

The second validation is a cross-check written as an independent piece of software. In a simplified approach the expected missing event weight after re-weighting with up to two tau fakes was calculated. The simplification is a limitation on the extreme cases with maximal and minimal probability of jets faking taus.

From the event weight analysis (Fig. 5.4) one could see, that event parts with a sum of



(a) Percentage of weight missed by applying the re-weighting method. The red and blue lines show the expected extreme cases in dependence on the number of jets, with red being the highest possible probability of jets faking taus. The green dashed line shows the mean missed weight obtained from the analysis.

(b) Number of jets before applying the re-weighting method. All background samples are shown and 4 different signal samples. The number of jets is one of the important factors on the missed event weight.

Figure 5.5.: Cross-check of missed weight in the re-weighting method (a) and jet multiplicity (b).

about 80 full events out of $250 \cdot 10^6$ events are not used. This corresponds to a fraction of $0.32 \cdot 10^{-6}$.

Fig. 5.5a shows the two expected extreme cases for the missing weight after applying the re-weighting procedure with up to two fake taus from jets in dependence on the number of jets. The red line describes the case, where every jet has a probability of 0.94% to fake a tau. This is the “worst” case scenario, where in the case of a high number of jets the fraction of missed events rises fast. The blue line is a kind of “best” case scenario, where all jets have a probability of 0.05% of jets faking taus. Due to the range restrictions, jets are used in a broader $|\eta|$ range, some jets have a probability of 0 of faking taus, but this is the trivial case, where 100% of the weights enter the analysis.

For the bins 0-2 jets the method gives full coverage of the event information. Therefore as well the best case as the worst case scenario yield no missed event weight.

The area between the red and blue line should cover the percentage of missed weight of the analysis, since it covers the cases where the probabilities lie between 0.05% and 0.94%, which is the realistic case, as seen before.

Looking at Fig. 5.5b there are only a few events with more than 25 jets. The green dashed line marks the previously from the analysis derived value of $0.32 \cdot 10^{-6}$. Since the value lies within the expected area, this test is successfully passed.

5.6. Overlap removal II

After the incorporation of fake electrons and fake taus from jets another overlap removal needs to be done. At first overlap removal I (cf. Tab. 5.1) is repeated to remove the jets producing the fake electrons and fake taus and to get rid of tau fakes in proximity of electrons. This is necessary, since the fake electrons and taus from jets would be indistinguishable from “real” ones in an analysis with data.

The second part of the overlap removal is targeted towards event cleaning (cf. Tab. 5.2). I.e. removing light leptons possibly originating from jets and discarding events from bremsstrahlung and low mass decays.

considered objects	$\Delta R/m_{ll'}$ requirement	
$\Delta R_{e,j}$	< 0.4	discard electron
$\Delta R_{\mu,j}$	< 0.4	discard muon
$\Delta R_{e,\mu}$	< 0.01	discard both
$\Delta R_{\mu,\mu}$	< 0.05	discard both
$m_{\text{SFOS}}(ll')$	$< 12 \text{ GeV}$	discard both

Table 5.2.: Requirements of the second overlap removal.

The first two requirements discard all electrons and muons within a cone of $\Delta R = 0.4$ around jets to remove electrons and muons originating from these jets.

In the following steps electrons and muons closer than $\Delta R = 0.01$ to each other are both removed, since the electron could originate from the muon due to bremsstrahlung processes. Muons next to muons (within $\Delta R = 0.05$) are both removed. Finally a reduction of low-mass decays is achieved by vetoing same flavor and opposite sign (SFOS) light lepton pairs with an invariant mass lower than 12 GeV.

5.7. Lepton isolation

The light leptons entering the analysis have to be isolated. I.e. only a small amount of energy should be deposited around the light lepton.

A cone of $0.0001 < \Delta R < 0.3$ around the light lepton is considered and the sum of the visible¹ p_T is calculated. If the sum of the visible p_T is smaller than 15% of the p_T of the light lepton it passes the isolation criterion, otherwise it is discarded.

5.8. Object definitions

After executing all preparation steps the final object selection takes place. The thresholds for the different objects are already anticipated in the selection process, but the smearing procedure alters the p_T of the objects. At this step it is ensured, that all objects fulfill the requirements listed in Tab. 5.3.

¹All final state particles, excluding neutrinos and neutralinos.

Object	Minimal p_T	Maximal $ \eta $
electron	10 GeV	2.47
muon	10 GeV	2.4
tau	20 GeV	2.5
jet	20 GeV	4.5

Table 5.3.: Object definition cuts.

5.9. Trigger

Due to the high event rate provided by the LHC, ATLAS uses triggers to keep the recording event rate sufficiently low. For this kind of analyses mostly p_T and $|\eta|$ thresholds are used to select the relevant events.

In a sample of real data only events above these threshold would be recorded, but in the MC generation all events enter. To account for this fact, a simple trigger requirement is introduced, requiring a high p_T electron or a muon with the requirements listed in Tab. 5.4.

Object	Minimal p_T	Maximal $ \eta $
electron	25 GeV	2.47
muon	25 GeV	2.4

Table 5.4.: Trigger requirements.

The thresholds are an estimation based on the experiences from the recent LHC runs. This trigger emulation in the presented analysis assumes a trigger efficiency of 100% above these thresholds.

6. Expected sensitivity in the 1 lepton and 2 tau final state

To calculate the expected sensitivity of an analysis in the channel $Wh \rightarrow 1l + 2\tau$ (cf. Sec. 2.3.2) at 3000 fb^{-1} signal regions were defined and optimized. In the following sections at first the calculation of the expected sensitivity is presented, then the channel definition is shown, thereafter the signal region cuts are explained and finally the obtained expected sensitivity is discussed.

6.1. Calculation of sensitivity

The goal of this analysis is to determine the sensitivity of a search in the Wh channel. The potential of exclusion or discovery of supersymmetric particles at the ATLAS detector in the HL-LHC scenario is investigated. For this purpose two kinds of sensitivities are calculated and interpreted as exclusion and discovery contours in the plane spanned by the $\tilde{\chi}_1^\pm$ and $\tilde{\chi}_1^0$ masses.

The sensitivity in general is based on the calculation of the p -value (cf. also [3]). The p -value describes the probability to get a result equal or less probable than an observation under the assumption of a certain hypothesis, e.g. the Standard Model or a SUSY signal model. Different hypotheses are tested for discovery and exclusion and tried to be rejected. If the probability of an observation is below certain limits (again different for discovery and exclusion) the hypothesis will be rejected.

In this analysis expectations for the number of events from background processes N_b and from signal processes N_s are obtained through definition of signal regions and counting the Monte Carlo events passing the preselection as well as all signal region cuts. It is assumed that SUSY processes always yield additional events. With a given expectation of events the observed number of events follows a Poisson distribution. From these Poisson distributions the p -values can in principle be calculated.

In the case of discovery the null hypothesis, i.e. the hypothesis tried to be rejected, is that the Standard Model holds unmodified. This means that the sum of expected events from background and signal processes lies in a tail of the Poisson distribution, formed by assuming only background events, corresponding to a low probability. For the exclusion of a certain signal model the null hypothesis is that the observed number of events (SM expectation) is unlikely with respect to a Poisson distribution of the sum of signal and background events.

A relative total background uncertainty δ_b is introduced, to emulate the impact of the uncertainties of a real analysis on the sensitivity. Since the uncertainties are not yet known, a fixed uncertainty has to be used. As a conservative estimate a constant total uncertainty of 30% on the background contribution is adopted from previous searches

at 8 TeV with 20.3 fb^{-1} of data [44] and applied for all mass-point pairs. It is assumed that these uncertainties will also hold in the HL-LHC scenario.

The p -value for discoveries can therefore be calculated as

$$p = \int_{N_b + N_s}^{\infty} di \mathcal{P}(i; N_b),$$

where $\mathcal{P}(i; N_b)$ is the probability of observing i events taken from a Poisson with an expected number of events N_b . Since the Poisson distribution is a discrete distribution and sensitivities for fractional events will be derived, a linear interpolation of the cumulative distribution function is used. The integral from $N_b + N_s$ to infinity is the probability that given an expectation of N_b events equal to or more than $N_b + N_s$ events will be observed.

To include the uncertainty on the background estimate the number of background events is varied with a Gaussian distribution \mathcal{G} centered around N_b with width $\delta_b N_b$:

$$p_{\text{disc}} = \int_0^{\infty} db \mathcal{G}(b; N_b, \delta_b N_b) \int_{N_b + N_s}^{\infty} di \mathcal{P}(i; b)$$

The p -values derived are usually converted in sensitivities. Sensitivities relate the probabilities to the corresponding number of standard deviations of a Gaussian distribution. E.g. a sensitivity of 5 corresponds to a probability of $2.85 \cdot 10^{-7}$. This is the probability which is by convention required to claim a discovery. The sensitivity is calculated as

$$Z_N = \sqrt{2} \text{erf}^{-1}(1 - 2p),$$

where $\text{erf}(x)$ is the error function.

For the exclusion potential a similar approach is used, now using the hypothesis that $N_b + N_s$ events are expected. To exclude a certain signal model it is required that the background expectation lies in the lower tail of the Poisson distribution with mean $N_b + N_s$. Including the background uncertainty the p -value is calculated as:

$$p_{\text{excl}} = \int_0^{\infty} db \mathcal{G}(b; N_b + N_s, \delta_b N_b) \int_0^{N_b} di \mathcal{P}(i; b)$$

For exclusion a weaker claim of $p = 5\%$ is required, corresponding to a sensitivity of 1.64. After the signal region cuts are specified the sensitivity is plotted on the $\tilde{\chi}_1^{\pm} - \tilde{\chi}_1^0$ grid and in the areas where the sensitivity exceeds 1.64 we expect, that an analysis carried out with 3000 fb^{-1} of data at ATLAS in the HL-LHC scenario will give an exclusion at 95% CL.

6.2. Channel definition

The channel definition is chosen according to the decay process presented in Sec. 2.3. At first exactly one light lepton (e or μ) is required, which in the case of a signal event

is supposed to originate from the W boson of the $\tilde{\chi}_1^\pm$ decay, but for background events may also arise from other W bosons, Z bosons or jets.

The second step is the selection of exactly two (hadronically decaying) taus, originating from the Higgs boson, but in many of the background processes coming from Z bosons or even misidentified jets. Since the pair of taus is supposed to be the direct decay product of the Higgs boson from the $\tilde{\chi}_2^0$ decay, both taus are required to carry opposite charges.

It is important to note, that this selection is heavily influenced by the re-weighting method applied during the introduction of fake taus from jets (cf. Sec. 5.5.1). In an analysis without the re-weighting method many events would be discarded at this point. With the re-weighting method there are almost always parts of the events passing this cut.

6.3. B-tagged jet veto

Important backgrounds entering the analysis are processes involving top antitop quark pairs ($t\bar{t}$). $t\bar{t}$ pairs are produced at high cross-sections at the LHC and are therefore to be considered and have also a lot of jet activity.

Top quarks decay almost exclusively to a W boson and a b -quark. Due to their short lifetime there is no hadronization and only the decay products of the top-quarks can be detected.

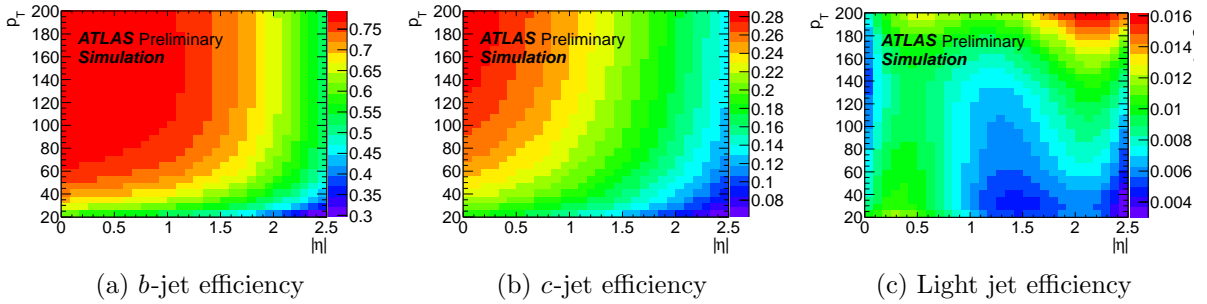


Figure 6.1.: Efficiency of tagging a b -jet plotted in the p_T - $|\eta|$ plane [43]. From left to right the tagging efficiencies for true b -jets, c -jets and light flavor (u, d, s) jets are shown.

A common way to identify events involving top-quarks is to try to find signatures of b -quarks. Since b -quarks live, in contrast to the top quarks, long enough to hadronize, the identification targets the emanating B -hadrons. In principle these B -hadrons can be detected using their decay length of $c\tau = 455.4 \mu\text{m}$ [3]. The procedure of identifying jets from B -hadrons is commonly called b -tagging.

Signatures for B -hadrons are, e.g. displaced secondary vertices, which can be resolved with the inner tracking system. If a secondary vertex can be reconstructed, the participation of a b -quark should be taken into consideration. Other measurements used for identification are e.g. the impact parameter due to the decay length and leptons next to the jet.

At ATLAS b -tagged jets (b -jets) are actually reconstructed with a multivariate procedure [45]. An algorithm employing neural networks is used. These machine learning

algorithms use e.g. the impact parameter and secondary vertices as input and optimize the discrimination cuts, which are then applied during the jet reconstruction. The algorithms are especially important in the discrimination of b -jets from c -jets, due to similarities in the signatures.

The performance of the b -jet-tagging algorithm is parameterized according to the functions for the European Strategy [43], highlighted in Sec. 5. In Fig. 6.1 the efficiencies of the b -jet-tagging for (real) b -jets, c -jets and light flavor (u, d, s) jets are shown. They are used to determine whether a jet will be considered as a b -jet in the analysis.

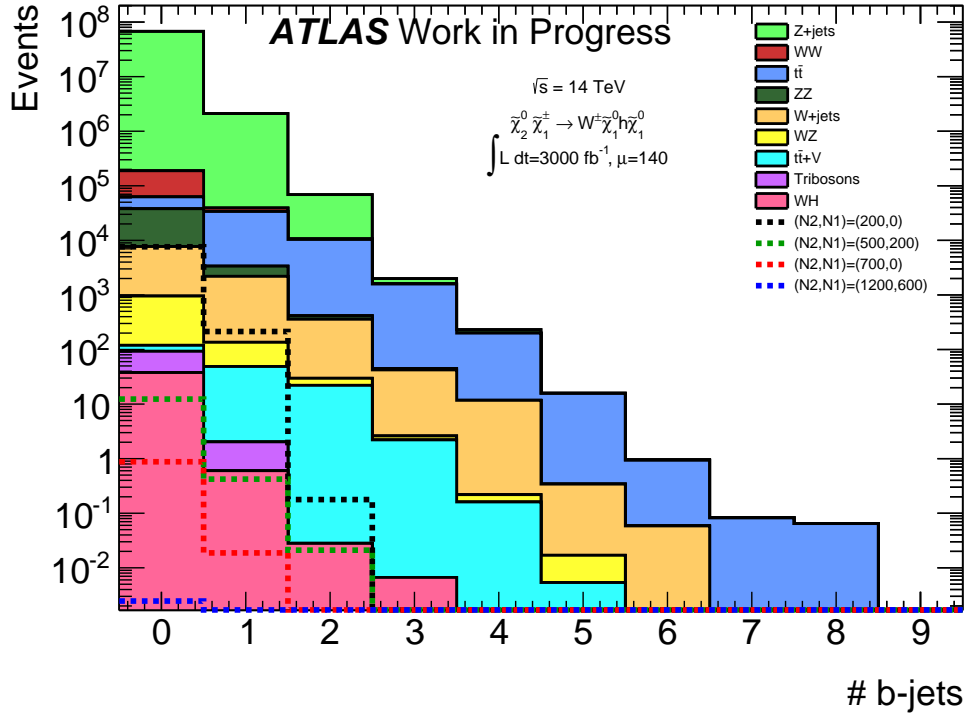


Figure 6.2.: b -jet multiplicity in the signal region after applying the channel definition. All background samples are stacked and color-coded. Four selected signal samples are overlaid with dashed lines.

Since the signature of the signal decay does not contain b -jets, a veto on these b -jets is applied. Fig. 6.2 shows for all included background samples and for four selected signal samples the multiplicity of b -jets in the events. It is visible that $t\bar{t}$ and $t\bar{t} + V$ processes have a lower contribution in the bin containing 0 b -jets, compared to the other background and signal samples. Since the b -jet veto is very useful in reducing $t\bar{t}$ contributions it is used for all signal regions.

6.4. Signal regions

After passing the channel definition and the b -jet veto the events are subjected to the final signal region cuts. These cuts are optimized to suppress most of the background, while increasing the proportional fraction of the signal. The optimization was pursued in several signal regions to speed up the optimization process. In the end two signal regions

were defined, one to cover the high-mass range and one optimized to have sensitivity for low masses.

6.4.1. Missing transverse energy

The first signal region cut is chosen to be applied on \cancel{E}_T . From the generator level filters of the $t\bar{t}$ and W with jets samples (cf. Sec. 4.3.6) it could be seen that a cut on the smeared \cancel{E}_T is necessary. In order to get a conservative estimate, a cut on \cancel{E}_T at 330 GeV was chosen. This is a rather high cut, motivated by the generator cuts of maximal 210 GeV on the true \cancel{E}_T (cf. 4.3.7). Adding two times the resolution of the smearing of 60 GeV results in the mentioned estimate. Since the high cut is especially difficult in the low-mass region, the sensitivity was additionally investigated in an optimistic scenario, possibly underestimating the backgrounds only, with a cut on \cancel{E}_T at 270 GeV.

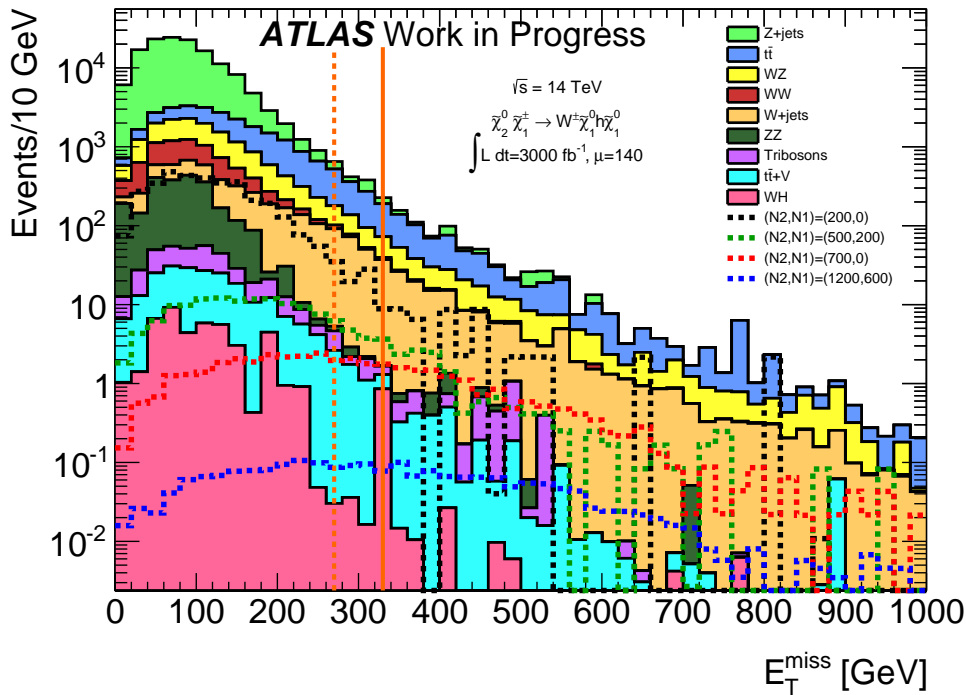
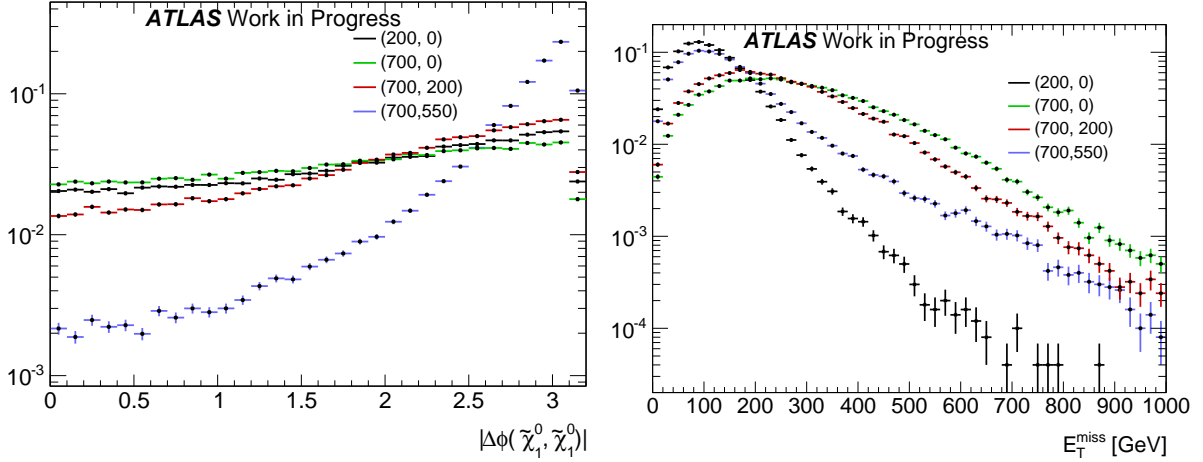


Figure 6.3.: \cancel{E}_T distribution after applying channel definition and b -jet veto. As explained in Sec. 4.3.6 the $t\bar{t}$ and W with jets background are underestimated below about 300 GeV. All background samples are stacked and color-coded. Overlaid are four selected signal samples with dashed lines. The vertical solid orange line shows the signal region cut at 330 GeV, while the dashed orange line shows the less conservative cut for comparison.

In Fig. 6.3 the \cancel{E}_T distribution after applying channel definition and b -jet veto is shown. Four selected signal samples are superimposed on the sum of the background contribution. It can be seen that for the signal points with a higher mass of $\tilde{\chi}_1^\pm$ the events have in general higher \cancel{E}_T and the discrimination power of the \cancel{E}_T cut is increased. In the case of the low mass samples, e.g. $m_{\tilde{\chi}_1^\pm} = 200$ GeV and $m_{\tilde{\chi}_1^0} = 0$ GeV, the signal

samples have a similar distribution as the background and therefore the discrimination power of the \cancel{E}_T cut is lower.



(a) $|\Delta\phi|$ of the two emerging $\tilde{\chi}_1^0$ for selected signal samples. With increasing $\tilde{\chi}_1^0$ masses the neutralinos tend to have larger angular separations. All samples are normalized to 1.
 (b) \cancel{E}_T of selected signal samples after smearing with no other selection cuts applied. With decreasing mass splitting the distributions are shifted to lower \cancel{E}_T values. All samples are normalized to 1.

Figure 6.4.: Smearred \cancel{E}_T and $\Delta\phi$ of the $\tilde{\chi}_1^0$ for selected signal samples.

The differences in the \cancel{E}_T distributions of the signal samples at different mass pair points can be explained by considering the kinematics of the process. The production of $\tilde{\chi}_1^\pm$ and $\tilde{\chi}_2^0$ will be always back to back in the transverse plane. Depending on the following decay of the $\tilde{\chi}_1^\pm$ to a W boson and a $\tilde{\chi}_1^0$ and the decay of the $\tilde{\chi}_2^0$ to a h and a $\tilde{\chi}_1^0$ the \cancel{E}_T will vary substantially. Fig. 6.4a shows the difference in ϕ of the two escaping $\tilde{\chi}_1^0$ for the lowest-mass signal sample (200, 0) and three samples with a mass of the $\tilde{\chi}_1^\pm/\tilde{\chi}_2^0$ of 700 GeV and varying $\tilde{\chi}_1^0$ masses. For the same selection of samples the \cancel{E}_T distribution after smearing without any other cuts applied is shown in Fig. 6.4b.

The events in the low-mass case (200, 0) are not expected to have much additional \cancel{E}_T , since the mass difference of 200 GeV between $\tilde{\chi}_1^\pm$ and $\tilde{\chi}_1^0$ is partly used to produce a h or a W boson and therefore the p_T of the produced particles will be rather low. The $\Delta\phi$ distribution of the two $\tilde{\chi}_1^0$ is rather flat, since their mass is 0 GeV. Because there is not much p_T involved, the \cancel{E}_T distribution is high at lower values and fast decreasing for higher values.

More interesting are the distributions in the case of a high $\tilde{\chi}_1^\pm$ mass of e.g. 700 GeV. In this case the initial $\tilde{\chi}_1^\pm$ and $\tilde{\chi}_2^0$ have a high amount of energy. If the mass of the $\tilde{\chi}_1^0$ is also high, as in the case of (700, 550), most of the available energy is used to produce both $\tilde{\chi}_1^0$. Since the $\tilde{\chi}_1^0$ are in this case the heavier decay products, they are oriented predominantly in the direction of their mother particles due to momentum conservation, which is back to back to each other, as can be seen in Fig. 6.4a (blue sample). Therefore the high momenta they are carrying away preferably cancel each other out in the transverse plane, causing the \cancel{E}_T to be shifted to lower values than expected.

For the samples with a lighter $\tilde{\chi}_1^0$ the $\Delta\phi$ distribution is rather flat, since they have

comparable masses to the respective other decay product. With the isotropic escaping particles the cancellation of p_T in the transverse plane is reduced and therefore the \cancel{E}_T distribution is much broader than in the high $\tilde{\chi}_1^0$ mass case.

In summary the high \cancel{E}_T cut can be accepted in the region with high mass splittings, since due to the flat \cancel{E}_T distributions the sensitivities benefit from a high cut on \cancel{E}_T . In the low mass region and the region with small mass splittings however the high cut reduces a lot of the signal contribution and will unfortunately lead to a decreased reach in sensitivity.

6.4.2. Invariant mass of the two taus

The next signal region cuts are carried out on the invariant mass of the two taus. The invariant mass of the two taus (τ_1, τ_2) with four-momenta p_1 and p_2 , energies E_1 and E_2 and three-momenta \vec{p}_1 and \vec{p}_2 is calculated as:

$$m_{\tau\tau}^2 = (p_1 + p_2)^2 = 2m_\tau^2 + 2(E_1E_2 - \vec{p}_1 \cdot \vec{p}_2) \quad (6.1)$$

If the two taus are the decay product of a common mother particle, $p_1 + p_2$ will be equal to the four-momentum of the mother particle, due to energy and momentum conservation. Therefore calculating the invariant mass of the two taus would in principle give the mass of the mother particle.

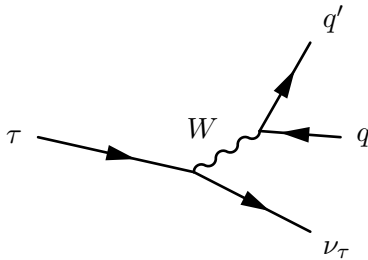


Figure 6.5.: Feynman diagram of the hadronic tau decay. The tau neutrino escapes the detector and a jet arises from the W boson.

In the case of the decay to two hadronically decaying taus it is not possible to directly infer the mass of the mother particle. This is due to the fact that the tau jet originating from the tau does not hold all the momentum. Fig. 6.5 shows the process of the tau decay. The tau in the initial state decays to a W boson and a tau neutrino. This tau neutrino escapes the detector and carries away a part of the momentum. The remaining part of the momentum of the tau is transferred to the W boson, which is then decaying to two quarks. These two quarks build up the jet which will be reconstructed as a tau and will consecutively give rise to the momentum of the tau. Therefore the invariant mass of the two taus is expected to be distributed more broadly below the mass of the mother particle, which in this case is the Higgs boson. In addition the Higgs boson mass gives an upper limit for the invariant mass.

Even if the reconstruction of the Higgs boson mass is not expected to be exact, a cut on the invariant mass is useful. On the one hand this cut helps to reduce background processes with an unassociated production of the two taus, i.e. events with taus from W

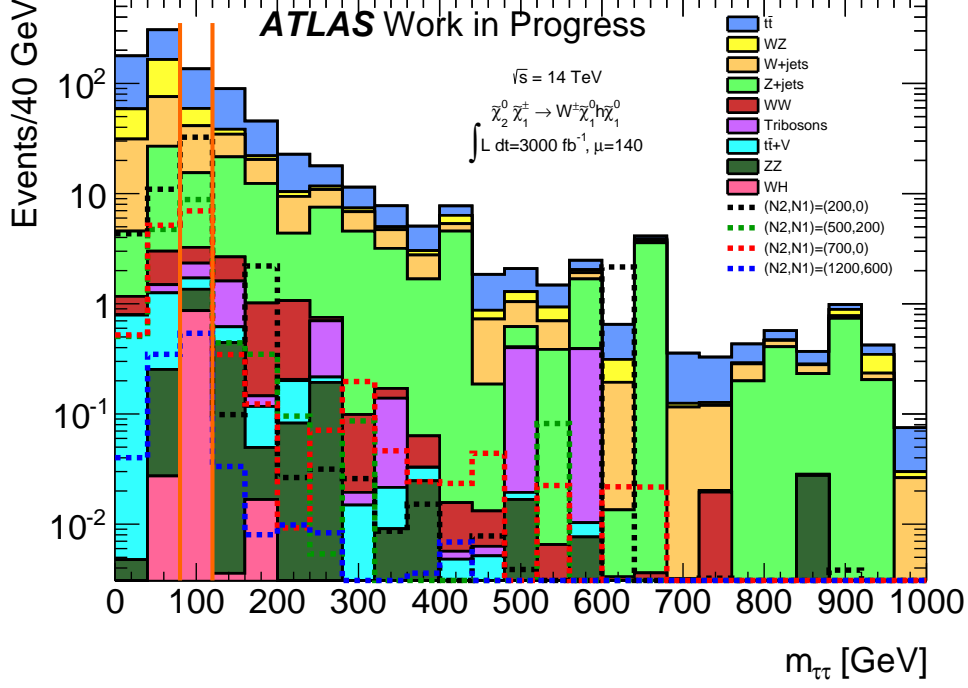


Figure 6.6.: Invariant mass of both taus after applying the channel definition, the b -jet veto and the cut on \cancel{E}_T . All background samples are stacked and color-coded. Four selected signal samples are overlaid with dashed lines. The vertical orange lines show the optimized signal region cuts at 80 GeV and 120 GeV.

decays or jet fakes will have a broadly distributed $m_{\tau\tau}$. On the other hand events with taus from a Z decay will have their invariant mass distributed below about 90 GeV, showing a similar shift as taus from a h decay.

Fig. 6.6 shows the distribution of the invariant mass of the two taus with all previous cuts applied. The accumulation of the signal samples below 120 GeV can be seen. A window between 80 GeV and 120 GeV is chosen, to include most of the signal, which is below the Higgs boson mass of 125 GeV, but to also provide a separation from background processes involving Z bosons decaying to two taus, exploiting the lower Z boson mass.

6.4.3. Scalar sum of the transverse momenta of the two taus

The penultimate signal region cut is performed on the scalar sum of the p_T of the two taus. This cut is especially useful for bigger mass splittings between $\tilde{\chi}_1^\pm$ and $\tilde{\chi}_1^0$.

Since in the previous step a cut on the invariant mass of the two taus was performed, a first constraint is put on both taus. Recalling Eq. 6.1 there is a degree of freedom left, which can be parameterized by the angle between both taus or by the momenta $|\vec{p}_1|$ and $|\vec{p}_2|$.

The cut on the scalar sum of the p_T of the two taus is complementary to the cut on the invariant mass of those taus. It targets the increased p_T of the taus from the Higgs boson decay, since the Higgs boson will be boosted in dependence on the mass

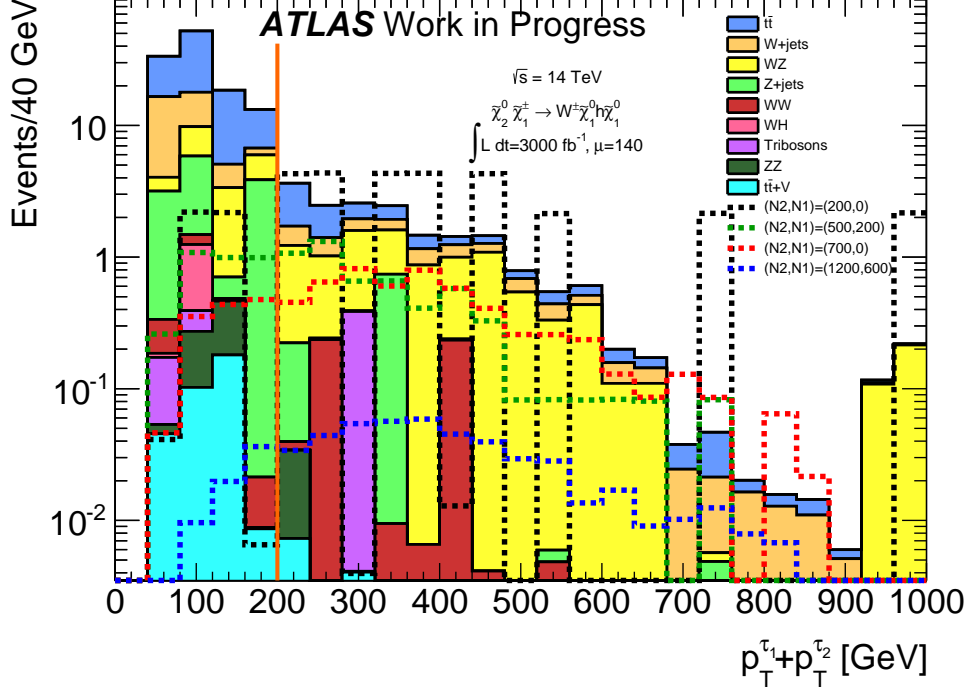


Figure 6.7.: Distribution of the scalar sum of p_T of both taus after applying the channel definition, the b -jet veto and the cuts on \cancel{E}_T and $m_{\tau\tau}$. The first bin is not filled since all taus are required to have p_T of at least 20 GeV and therefore all events have a minimum value of $|p_T^{\tau_1}| + |p_T^{\tau_2}| = 40$ GeV. All background samples are stacked and color-coded. Four selected background samples are overlaid with dashed lines. The vertical orange line shows the optimized signal region cut at 200 GeV.

splitting. Since in Eq. 6.1, assuming fixed $|\vec{p}_1|$ and $|\vec{p}_2|$, the expression

$$\vec{p}_1 \cdot \vec{p}_2 = |\vec{p}_1| |\vec{p}_2| \cos(\theta)$$

decreases with increasing angular separation θ between \vec{p}_1 and \vec{p}_2 , $m_{\tau\tau}$ in total increases. This means in reverse, that at fixed $m_{\tau\tau}$ large angular separations need less $|p_T|$ than small ones.

In the case of signal events it is expected that both taus stem from a Higgs boson decay, which might be slightly to highly boosted, due to the mass difference of $\tilde{\chi}_2^0$ and $\tilde{\chi}_1^0$. The angular separation should be smaller than the one in uncorrelated events as e.g. events from jet fakes. Therefore should $|\vec{p}_1|$ and $|\vec{p}_2|$ be in signal events in general increased.

Fig. 6.7 shows the distribution of the sum of the scalar p_T of the two taus with channel definition, b -jet veto and the cuts on \cancel{E}_T and $m_{\tau\tau}$ already applied. It can be seen that background processes with one or more jets misidentified as taus such as $t\bar{t}$ and Z or W with jets have high contributions at lower $|p_T^{\tau_1}| + |p_T^{\tau_2}|$ values. In contrast signal samples with higher mass splittings, such as (700, 0) (red) or (1200, 600) (blue), are centered towards higher values of $|p_T^{\tau_1}| + |p_T^{\tau_2}|$.

An optimization for highest possible sensitivities was carried out on this variable. In combination with the other cuts a cut value of $|p_T^{\tau_1}| + |p_T^{\tau_2}| = 200$ GeV was obtained as

an optimum for the reach in sensitivity.

6.4.4. Transverse mass of the light lepton

After the cut on \cancel{E}_T targeting the escaping particles, after both cuts on the invariant mass and the sum of p_T of the two taus tailored on the Higgs boson decay, the information of the light lepton is exploited for the last cut. The light lepton is supposed to originate from the W boson decaying from the $\tilde{\chi}_1^\pm$. Since once again a neutrino is involved in the decay, a full reconstruction of the W boson mass is not possible.

W bosons would usually be reconstructed by calculating the invariant mass of the lepton and the \cancel{E}_T with the assumption that the primary source of \cancel{E}_T is the escaping neutrino from the W boson. The transverse mass can therefore be calculated using the azimuthal angle of the direction of the \cancel{E}_T , $\phi_{\cancel{E}_T}$, and the angle of the light lepton ϕ_l as [3]:

$$m_T^2 = 2\cancel{E}_T p_T(l) (1 - \cos(\phi_{\cancel{E}_T} - \phi_l))$$

If most of the missing transverse energy is caused by the escaping neutrino from the W boson decay, the peak of the transverse mass should be about the value of the W boson mass. But the mass resolution is usually limited due to additional sources of \cancel{E}_T , which will be most of the time present.

In the case of production of supersymmetric particles and escaping $\tilde{\chi}_1^0$ however, substantial additional sources of \cancel{E}_T can be present. The m_T is expected to be increased due to the escaping $\tilde{\chi}_1^0$ and the neutrinos from the tau and W boson decays.

In Fig. 6.8 can be seen that, after applying all other signal region cuts, the m_T distribution provides an additional signal and background discrimination. Especially the W boson dominated backgrounds as WZ and W with jets have, as expected, most of their contribution at lower m_T values. The signal samples are less dependent on m_T and shifted to higher m_T values. The low mass sample (200, 0) is badly modeled due to the low statistics. The scale factor for each MC event entering the distribution is about 2. Therefore the originally devised cut on m_T at 160 GeV only yields high sensitivities for samples with higher masses. A lower cut (magenta line) of 80 GeV defines a low-mass signal region with more signal contribution from low-mass points. The optimization of the signal region cut is especially for the low-mass samples influenced by statistical fluctuations due to the low statistics.

6.4.5. Signal region yields

After applying all cuts the yields of the different samples can be evaluated. The expected event numbers after each signal region cut are presented in Table 6.1.

It can be seen how the different signal region cuts reduce the background processes, but also how many signal events survive the cuts. In the case of the high-mass region with a cut on $m_T > 160$ GeV, 2.19 events from background processes are expected entering the signal region, where the biggest contribution is from $t\bar{t}$ processes. Further contributions come from WZ and WW backgrounds and all other processes are suppressed to negligible levels. The highest signal contribution is achieved at the signal point (500, 0) with 8.54 events.

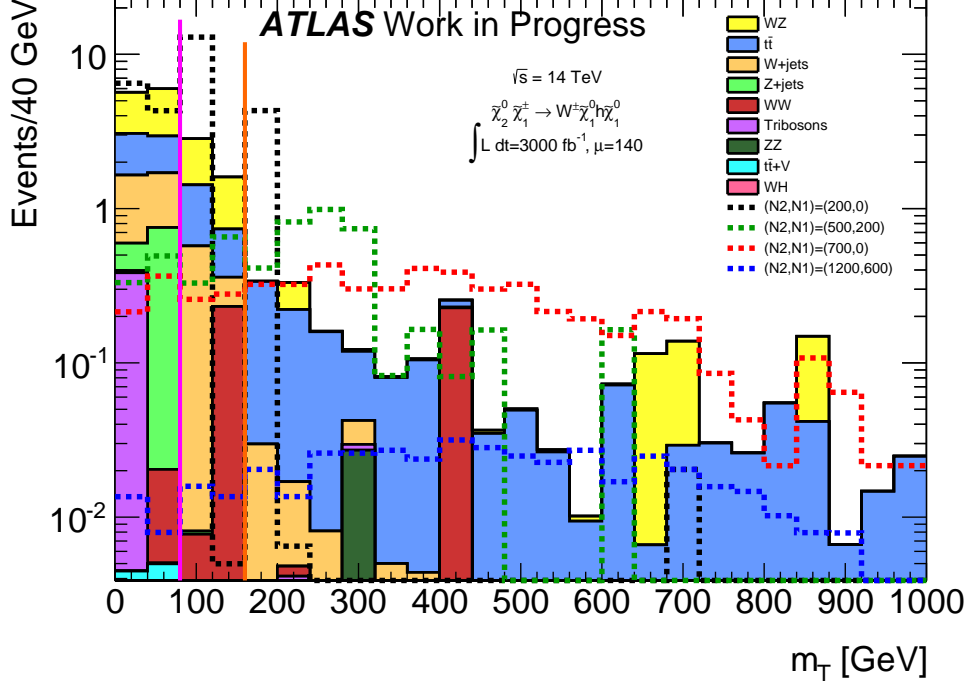


Figure 6.8.: Distribution of the transverse mass of the light lepton after applying channel definition, b -jet veto and the cuts on \cancel{E}_T , $m_{T\tau}$ and $|p_T^{\tau 1}| + |p_T^{\tau 2}|$. All background samples are stacked and color-coded. Four selected signal samples are overlaid with dashed lines. The vertical orange line shows the optimized cut for the high-mass signal region at 160 GeV and for the low-mass region a cut of 80 GeV is applied (magenta line).

The low-mass region with the loosened m_T cut has an increased background contribution of 6.64 events in the signal region. As expected samples containing W boson decays enter increasingly the signal region. But this increase of the background contribution can be accepted since the signal contribution of $(200, 0)$ increases to 17.28 events.

6.5. Expected sensitivities

After performing all preparation steps and executing the necessary signal region cuts the sensitivities can be calculated. As described above an estimate on signal and background yield is obtained from processing all selected samples with the above explained procedure and both signal region definitions. The results of the analysis will be presented in the following.

6.5.1. Results

The signal region cuts were optimized, that on the one hand the sensitivity has a maximal reach, i.e. as many points in the $\tilde{\chi}_1^\pm - \tilde{\chi}_1^0$ mass grid as possible have a sensitivity for exclusion larger than 1.64, and on the other hand reaches maximal values in the discovery sensitivity in order to achieve a discovery region, i.e. to exceed the value of 5.

	$t\bar{t}V$	Wh	WZ	triboson	
b -jet veto	179	45.1	7.69e3	183	
$\cancel{E}_T > 330$ GeV	2.59	0.924	145	3.26	
$80 \text{ GeV} < m_{\tau\tau} < 120$ GeV	0.36	0.866	18.0	0.625	
$ p_T^{\tau_1} + p_T^{\tau_2} > 200$ GeV	0.021	0.36e-6	8.39	0.384	
$m_T > 80$ GeV	0.012	0.14e-6	2.74	5.0e-3	
$m_T > 160$ GeV	8.0e-3	0.0	0.45	5.0e-3	

	ZZ	Z with jets	$t\bar{t}$	WW	
b -jet veto	1.97e3	116e3	11.5e3	3.56e3	
$\cancel{E}_T > 330$ GeV	1.55	101	447	5.84	
$80 \text{ GeV} < m_{\tau\tau} < 120$ GeV	0.488	12.2	76.7	0.91	
$ p_T^{\tau_1} + p_T^{\tau_2} > 200$ GeV	0.027	0.935	5.27	0.50	
$m_T > 80$ GeV	0.027	0.37e-3	2.61	0.47	
$m_T > 160$ GeV	0.027	0.0	1.37	0.23	

	W with jets	(200,0)	(500,200)	(700,0)	(1200,600)
b -jet veto	2.50e3	3.52e3	150	40.7	2.17
$\cancel{E}_T > 330$ GeV	139	52.4	15.1	13.6	1.01
$80 \text{ GeV} < m_{\tau\tau} < 120$ GeV	25.8	32.5	8.83	6.97	0.54
$ p_T^{\tau_1} + p_T^{\tau_2} > 200$ GeV	2.78	28.1	5.51	5.66	0.47
$m_T > 80$ GeV	0.77	17.3	4.68	5.08	0.45
$m_T > 160$ GeV	0.083	4.35	3.70	4.54	0.42

Table 6.1.: Table including the cutflows for the signal region cuts. The first line holds the event numbers after applying channel definition and b -jet veto. The last two lines show the signal region yields for both presented signal regions according to their m_T cut. All considered sub-processes and the four selected signal processes are shown.

After pursuing optimization in different signal regions it could be seen, that the signal regions optimizing for discovery potential have a similar exclusion reach as the dedicated exclusion signal regions. Only in the case of the lowest-mass sample (200, 0) the exclusion sensitivity could be considerably improved with a differing signal region. Therefore these two signal regions are selected and presented in the following.

Exclusion for high masses

Pushing the sensitivity towards higher $\tilde{\chi}_1^\pm$ masses, decreasing signal cross-sections become a problem. Fig. 6.9 shows the sensitivity in the $\tilde{\chi}_1^\pm$ - $\tilde{\chi}_1^0$ grid for the high-mass signal region, which is the overall best performing signal region.

The exclusion limit could be pushed to an optimum of about 700 GeV in terms of the $\tilde{\chi}_1^\pm$ mass with the presented signal region cuts. The reach is limited due to the low number of signal events in the signal region. While for the signal sample (700, 0) 4.5 events enter the signal region the next mass pair point (800, 0) has only 3.5 events, failing

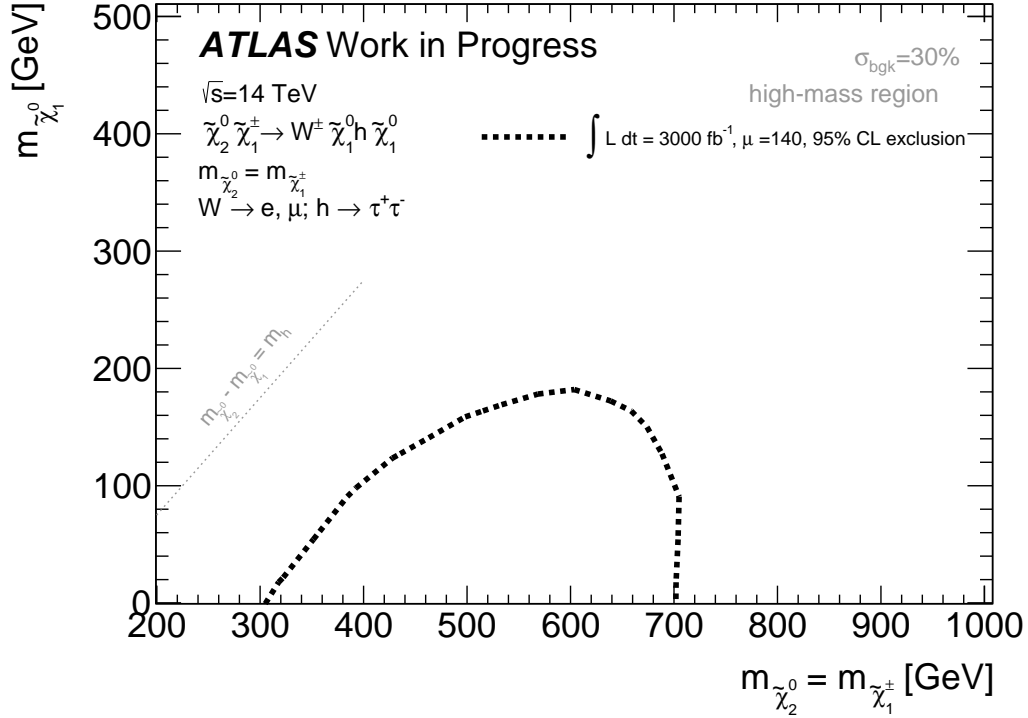


Figure 6.9.: Sensitivity in the $\tilde{\chi}_1^\pm$ - $\tilde{\chi}_1^0$ mass grid for the high-mass signal region cuts described in Sec. 6.4. The dashed line marks the exclusion potential at 95% CL with 3000 fb^{-1} at 14 TeV center-of-mass energy.

with a sensitivity of 1.25 to provide an exclusion limit. Although the signal region cuts do a good job in discriminating signal from background, the limiting factor of the mass reach is the low number of events after channel definition and b -jet veto. For example (1200, 0) (cf. Tab. 6.1) enters the signal region cuts with only about 2 events and despite the fact that the cuts only reduce them by a factor of 5, which is few in comparison to lower mass samples, it is not enough to achieve sensitivity.

Discovery potential

The optimization for discovery potential was done by maximizing the sensitivity in the most promising area. After trying out different signal region cuts it turned out that the areas around the mass pair points (200, 0) and (500, 0) were the most promising, assuming a \cancel{E}_T cut at 330 GeV. (500, 0) is characterized having a comparably high cross-section and good discrimination potential due to the mass difference in $\tilde{\chi}_2^0$ and $\tilde{\chi}_1^0$ and therefore a boosted Higgs boson. (200, 0) has an even higher cross-section, but suffers in discrimination power to the backgrounds.

Unfortunately the maximal sensitivity reached at (500, 0) is 2.78, not enough for a discovery potential. Interestingly enough the sensitivity in the low mass region reaches at (200, 0) a value of 3.72. This is not a reliable result due to the low statistics in the signal regions, but suggests that lower \cancel{E}_T cuts could increase the sensitivity and a discovery potential should, based on this analysis, not be excluded.

Exclusion for small masses

As already mentioned above a dedicated signal region for the lowest-mass region was developed. The sensitivity in Fig. 6.9 is at (200, 0) below the exclusion threshold, therefore the cut on m_T was relaxed in this signal region to show that an exclusion potential can certainly be expected there.

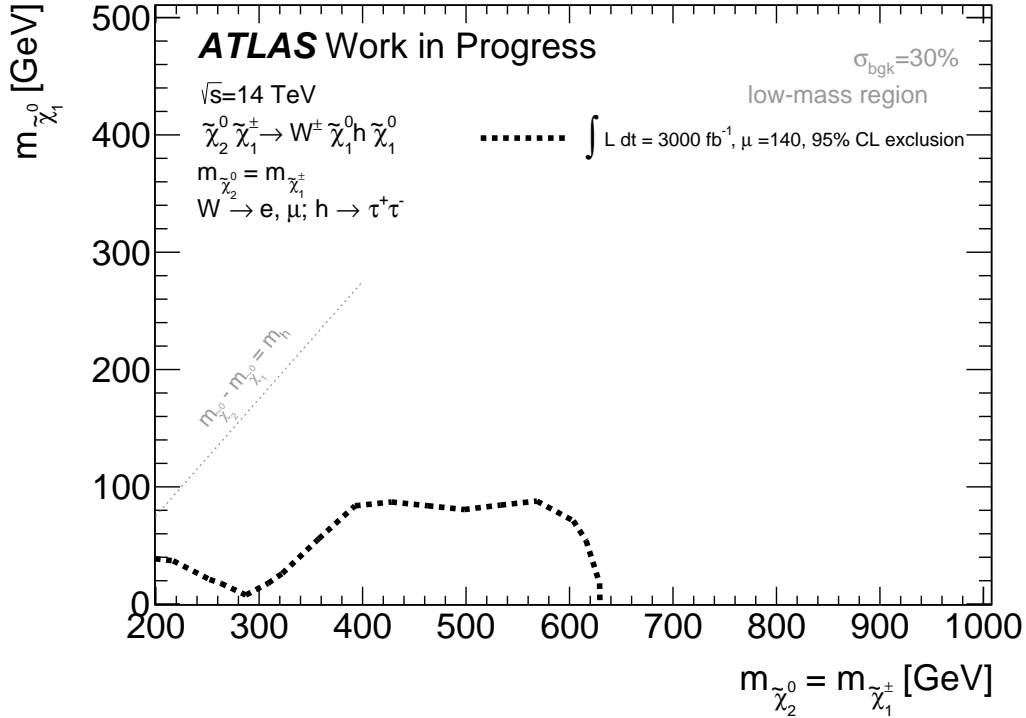


Figure 6.10.: Sensitivity in the $\tilde{\chi}_1^\pm - \tilde{\chi}_1^0$ mass grid for the low-mass signal region cuts described in Sec. 6.4. The dashed line marks the exclusion potential at 95% CL with 3000 fb⁻¹ at 14 TeV center-of-mass energy.

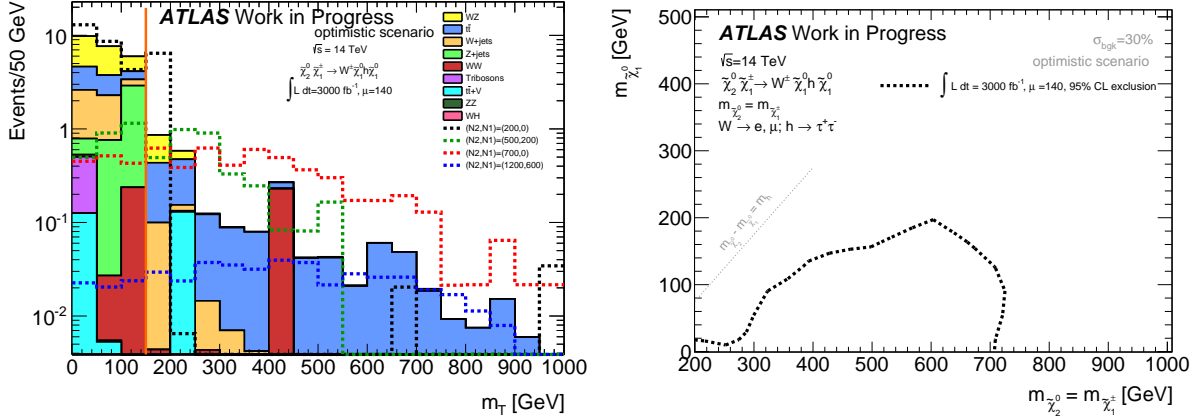
Fig. 6.10 shows the exclusion contour in the low-mass signal region. A significantly higher sensitivity could be reached by relaxing the m_T cut showing that on the lowest mass point exclusion potential can certainly be expected at the cost of reach in the high-mass region.

Exclusion for small mass splittings

An especially difficult area for sensitivity is the diagonal, the region of small mass splittings between $\tilde{\chi}_1^\pm$ and $\tilde{\chi}_1^0$. Fig. 6.9 and 6.10 mark with a dotted line in light gray the border above which the mass difference between $\tilde{\chi}_2^0$ and $\tilde{\chi}_1^0$ is smaller than 125 GeV and therefore the decay to a Higgs boson is kinematically forbidden.

As seen in the discussion of the \cancel{E}_T cut (Sec. 6.4.1) the differences in the azimuthal angles of the escaping neutralinos are larger for samples with small mass splittings. This resulted in \cancel{E}_T distributions shifted to lower values (cf. Fig. 6.4b) and therefore a strong reduction of signal and background events at the \cancel{E}_T cut. Another problem is that the visible decay products are a W boson and a Higgs boson with low p_T . As we could see

beforehand the discrimination power of the signal region improves with higher energetic decay products.



(a) m_T distribution for the optimistic scenario described in Tab. 6.2. The vertical orange line shows the optimized cut on m_T at 150 GeV. (b) Sensitivity in the $\tilde{\chi}_1^\pm - \tilde{\chi}_1^0$ mass grid for the optimistic scenario described in Tab. 6.2. The dashed line marks the exclusion potential at 95% CL with 3000 fb^{-1} at 14 TeV center-of-mass energy.

Figure 6.11.: Optimistic scenario using \cancel{E}_T cut of 270 GeV. It has to be noted, that backgrounds are possibly underestimated and therefore the sensitivity overestimated.

To see how the \cancel{E}_T cut influences the exclusion reach an optimistic scenario is considered. It is based on a loosened \cancel{E}_T cut at 270 GeV corresponding to the generator cut with a safety margin of only one time the smearing resolution of 60 GeV. The other cuts are optimized accordingly and all signal region cuts are summarized in Tab. 6.2.

$\cancel{E}_T > 270 \text{ GeV}$	$80 \text{ GeV} < m_{\tau\tau} < 120 \text{ GeV}$
$ p_T^{\tau 1} + p_T^{\tau 2} > 260 \text{ GeV}$	$m_T > 150 \text{ GeV}$

Table 6.2.: Signal region cuts for the optimistic scenario.

Fig. 6.11b shows the sensitivity reached in this optimistic scenario (the according cut-flow is found in App. E). A similar exclusion potential as in the conservative estimation can be seen. But in this scenario one signal region is enough to cover as well the high-mass as the low-mass region. Some improvement towards the diagonal can be seen. Tab. 6.3 holds the signal region yields for the optimistic region.

In summary it is seen that it is very difficult to gain sensitivity next to the diagonal, since on the one hand the high \cancel{E}_T cut removes much of the signal contribution and on the other hand the cross-sections decrease with higher masses. Loosening the \cancel{E}_T cut is expected to improve the exclusion reach towards the diagonal, but cannot be shown due to the high generator cuts on the MC samples.

$t\bar{t}V$	0.4	WW	0.23
Wh	0.0	W with jets	0.15
WZ	0.55	(200,0)	6.50
triboson	5.14e-3	(500,200)	3.29
ZZ	0.372e-3	(700,0)	4.73
Z with jets	0.0	(1200,600)	0.42
$t\bar{t}$	1.24		

Table 6.3.: Table including the signal region yields for the optimistic signal region (cf. Tab. 6.2). All considered sub-processes and the four selected signal processes are shown.

6.5.2. Exclusion potential at 300 fb⁻¹

As a small complementary analysis the exclusion potential at 300 fb⁻¹ was investigated. The main difference to the presented analysis is that the pile-up is lower, but also the event numbers are scaled down with a factor of 10. The reduced pile-up of $\langle\mu\rangle = 60$ results in a reduced smearing with a resolution of 40 GeV. But even in an optimistic scenario using a \cancel{E}_T cut at 250 GeV no sensitivity above the exclusion threshold could be achieved. The improvement in the discrimination cuts due to the reduced pile-up is not high enough to compensate the reduced event numbers.

6.5.3. Exclusion potential in context

In the end a short comparison to the related $Wh \rightarrow 3$ light lepton analysis is done. The sensitivity for discovery is in this channel derived in a similar way, as in the analysis described above. But as described in [46] the same sensitivity is used for discovery and for the exclusion limits. The exclusion contour is set at 1.64 assuming similarity of the p -values for both hypotheses.

Besides targeting a different final state another major difference between the analyses is the \cancel{E}_T cut. While the 3 light lepton analysis uses a \cancel{E}_T cut of 100 GeV, for the one light lepton and two taus analysis a cut of 330 GeV is necessary. Looking at the sensitivity in the $\tilde{\chi}_1^\pm$ - $\tilde{\chi}_1^0$ grid (Fig. 6.12) there are several striking differences. The overall exclusion reach at 3000 fb⁻¹ of data is extended with respect to the analysis with two taus in the final state. Especially at the diagonal a much higher sensitivity could be achieved. The other big differences are the discovery contour at 3000 fb⁻¹ and the exclusion line at 300 fb⁻¹.

The increased sensitivity can be explained with the increased probability to reconstruct two light leptons from the Higgs boson decay. Since the W boson from the $\tilde{\chi}_1^\pm$ decay gives in both final states rise to a light lepton it is excluded from these considerations. A rough estimation of the number of events with the different final states is derived, as summarized in Fig. 6.13. Two decay processes of the Higgs boson are considered, $h \rightarrow WW$ with a branching ratio of 0.215 and $h \rightarrow \tau\tau$ with a branching ratio of 0.0632 (cf. Tab. 4.4). Taus decay in about 35% of the cases leptonically and in 65% of the cases

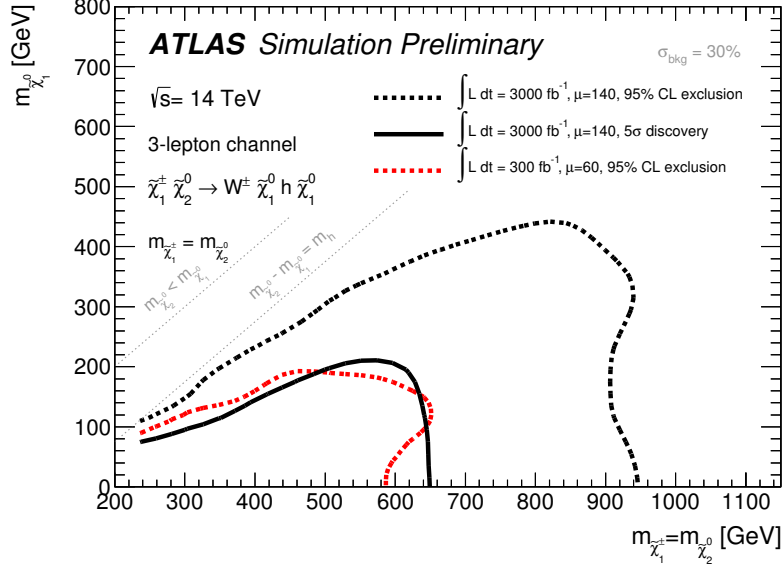


Figure 6.12.: Sensitivity in the $\tilde{\chi}_1^\pm$ - $\tilde{\chi}_1^0$ mass grid in the channel $Wh \rightarrow 3$ light leptons [46]. The black dashed line represents the exclusion at 95% CL at 3000 fb^{-1} . Enclosed by a black solid line a 5σ discovery region is visible. The red dashed line shows the exclusion limit at 300 fb^{-1} .

hadronically [3]. For W to light lepton decays an approximate branching ratio of

$$0.11 + 0.11 + 0.11 \cdot 0.35 = 0.26$$

is assumed, where 0.11 is the probability of a W to decay to 1 lepton (e , μ or τ) and the tau is required to decay leptonically.

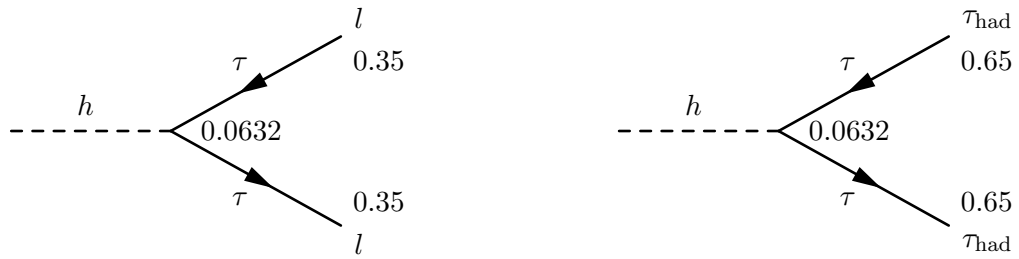
Combining the decay channels listed in Fig 6.13 the 2 light lepton final state occurs in $1.5\% + 0.77\% = 2.27\%$ of Higgs boson decays and the 2 hadronically decaying tau final state occurs in $0.11\% + 2.7\% = 2.81\%$ of Higgs boson decays. This means that the final state with two taus is favored and a search should be taken into consideration. But since taus are assumed to be only in roughly 55% of the cases reconstructed only $2.81\% \cdot 0.55^2 = 0.85\%$ of the Higgs boson decays will enter the analysis with 2 hadronically decaying taus. Therefore in the 3 light lepton analysis an about 2.7 times higher signal than in the 1 light lepton and 2 tau analysis is expected.

In total can be seen that the analysis targeting one light lepton and two taus has an overall reduced reach in sensitivity. The higher signal contribution in the 3 light lepton analysis allows to reach higher exclusion limits for $\tilde{\chi}_1^\pm/\tilde{\chi}_2^0$ and $\tilde{\chi}_1^0$ masses and the analysis provides at the same time a region where discovery is possible. Improvement of the one light lepton and two tau analysis could be achieved with a better tau reconstruction.

Combining both analyses would, using the presented assumptions, add only a small amount of sensitivity, since the exclusion contour of the one light lepton and two tau analysis is only about 10% higher than the discovery contour of the 3 light lepton analysis.



(a) $h \rightarrow WW$ with two light leptons in the final state. This sub-channel has a probability of 1.5%. (b) $h \rightarrow WW$ with two hadronic taus in the final state. This sub-channel has a probability of 0.11%



(c) $h \rightarrow \tau\tau$ with two light leptons in the final state. This sub-channel has a probability of 0.77%. (d) $h \rightarrow \tau\tau$ with two hadronic taus in the final state. This sub-channel has a probability of 2.7%

Figure 6.13.: Diagrams of $h \rightarrow WW$ and $h \rightarrow \tau\tau$ sub-channels with final states of two light leptons or 2 hadronically decaying taus. The probabilities as described in the text are listed at the vertices and final state particles and the overall probability of each diagram is given in the captions. Note that in these diagrams τ refers to the tau lepton and hadronically decaying taus are labeled as τ_{had} .

7. Conclusion and outlook

An analysis exploring the sensitivity in the HL-LHC scenario has been presented. The goal was to investigate up to which $\tilde{\chi}_1^\pm$ and $\tilde{\chi}_1^0$ masses exclusion potential will be expected in this analysis as well as if a discovery would be possible.

A detailed description of the necessary preparation steps for this analysis was given. The parameterized detector response was presented with focus on the \cancel{E}_T cuts of the available MC samples and the implication of the \cancel{E}_T smearing on these cuts. A rather high \cancel{E}_T cut of 330 GeV was inferred causing greatly reduced statistics in the signal regions. The introduction of fake taus misidentified from jets was improved by applying a re-weighting method in order to increase the amount of events passing the channel definition.

The considered channel targets an electroweakly produced pair of $\tilde{\chi}_1^\pm$ and $\tilde{\chi}_2^0$ decaying via W boson and Higgs boson to a final state of one light lepton, two hadronically decaying taus, the corresponding neutrinos and two $\tilde{\chi}_1^0$. Several signal region cuts were devised in order to provide the best possible separation between signal and background processes. The signal regions include a rejection of b -jets in order to suppress $t\bar{t}$ background processes. The kinematics of the signal processes were exploited using cuts involving the invariant mass of the two taus, the $|p_T|$ of the taus and the transverse mass of the light lepton.

It could be seen that defining two signal regions resulted in sensitivity for exclusion in the low-mass as well as in the high-mass region. The exclusion potential reaches at 3000 fb^{-1} up to 700 GeV in the $\tilde{\chi}_1^\pm/\tilde{\chi}_2^0$ masses and up to 180 GeV in the $\tilde{\chi}_1^0$ mass. No discovery contour could be reached, neither was there exclusion potential at 300 fb^{-1} . It could be shown that a lower \cancel{E}_T cut would likely improve the exclusion reach towards the diagonal, where the samples with low mass splittings are located.

The comparison with the related analysis with 3 light leptons in the final state shows that over the whole mass grid the expected sensitivity is significantly lower. This could be explained with a comparison of the branching fractions taking into account the reconstruction efficiency for taus.

The presented analysis shows that in a high luminosity scenario with an integrated luminosity of 3000 fb^{-1} the signal region targeting a final state of one light lepton and two hadronically decaying taus can be used to provide exclusion limits. With the production of MC samples with lower generator cuts on \cancel{E}_T and improved statistics more detailed projections can be done and the exclusion potential in the region of small mass splittings explored. To be able to keep up with the 3 light lepton analysis however more improvement would be necessary, such as a better tau reconstruction.

A. Parameters for detector response

$ \eta _{\min}$	$ \eta _{\max}$	a_1	a_2
0.00	0.18	0.01061	0.000157
0.18	0.36	0.01084	0.000153
0.36	0.54	0.01124	0.000150
0.54	0.72	0.01173	0.000149
0.72	0.90	0.01269	0.000148
0.90	1.08	0.01406	0.000161
1.08	1.26	0.01623	0.000192
1.26	1.44	0.01755	0.000199
1.44	1.62	0.01997	0.000232
1.62	1.80	0.02453	0.000261
1.80	1.98	0.03121	0.000297
1.98	2.16	0.03858	0.000375
2.16	2.34	0.05273	0.000465
2.34	2.52	0.05329	0.000642
2.52	2.70	0.05683	0.00074

Table A.1.: $|\eta|$ -dependent parameters for the muon ID resolution

B. Correlations for generator cut and true \cancel{E}_T

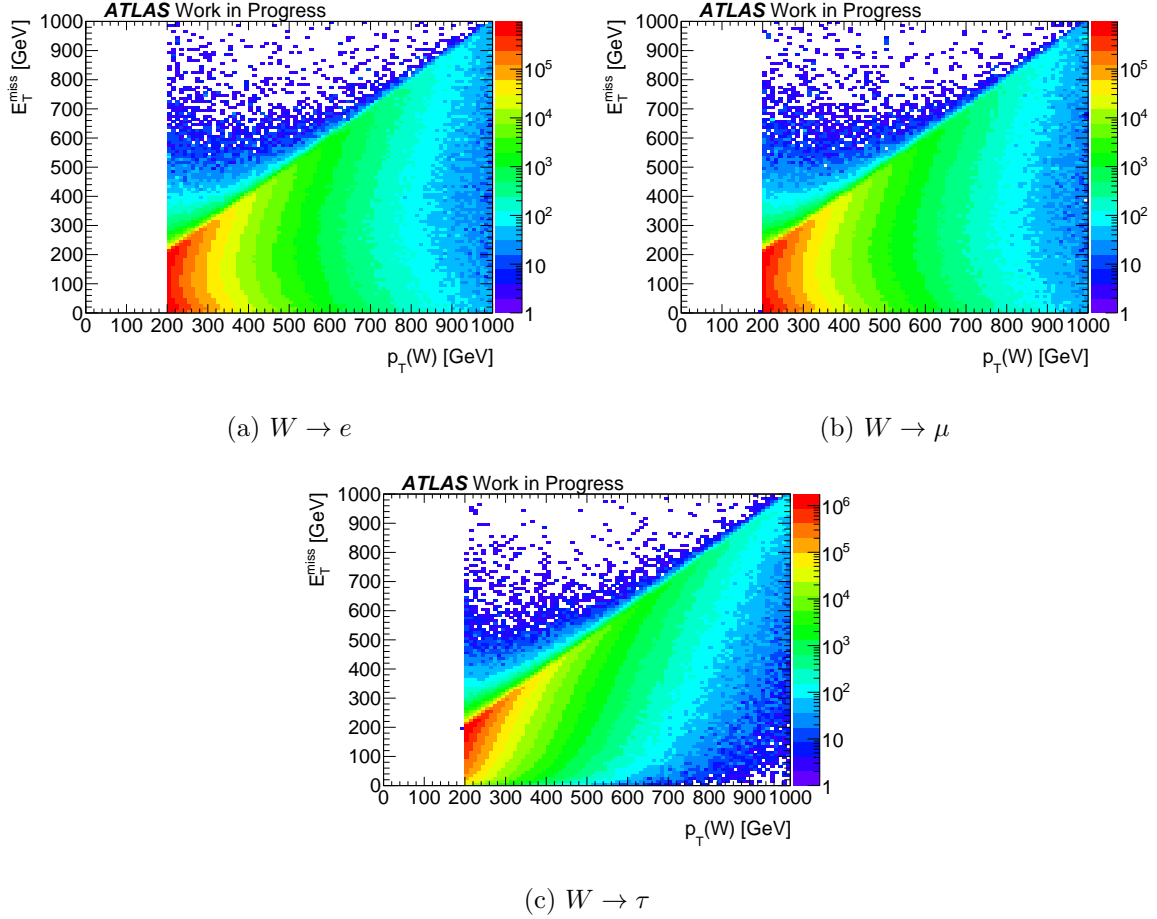
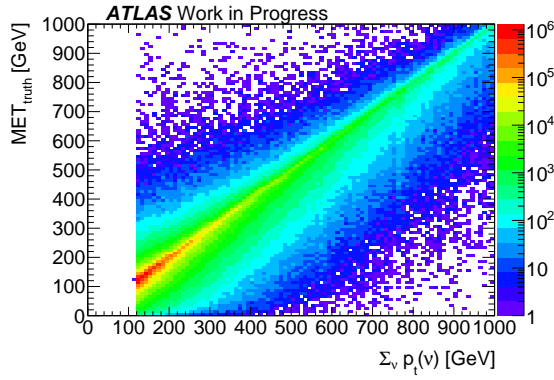
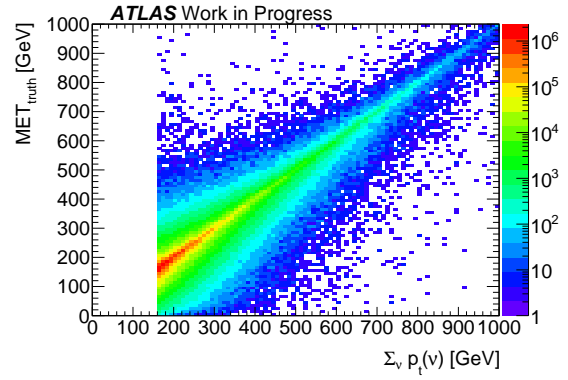


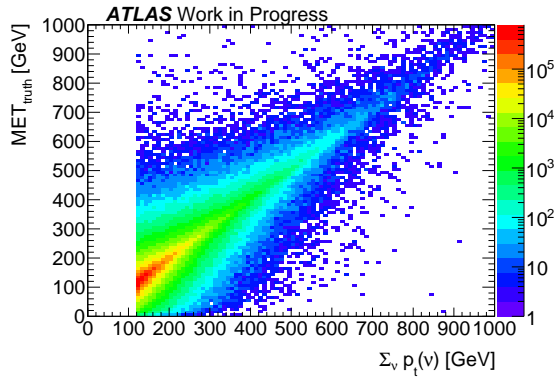
Figure B.1.: Correlation of $p_T(W)$ and true \cancel{E}_T for all W with jets samples. For a detailed description cf. Fig. 4.1b. The decay modes of the W bosons are listed for each plot.



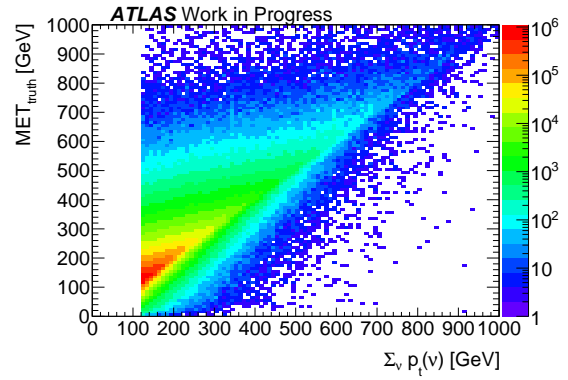
(a) $W \rightarrow l, W \rightarrow l$



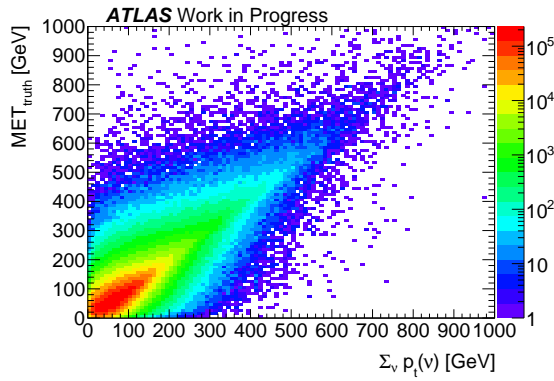
(b) $W \text{ had.}, W \rightarrow l$



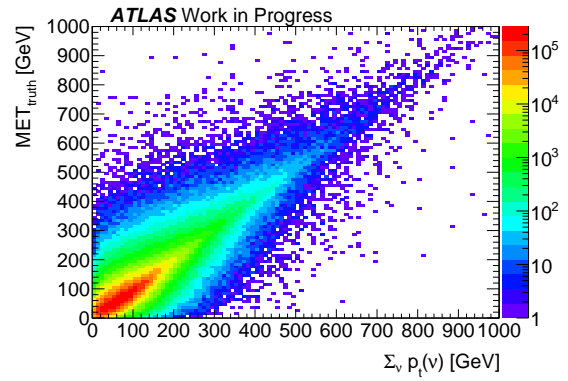
(c) $W \rightarrow l, W \rightarrow \tau_{\text{had}}$



(d) $W \rightarrow \tau_{\text{lep}}, W \text{ had.}$



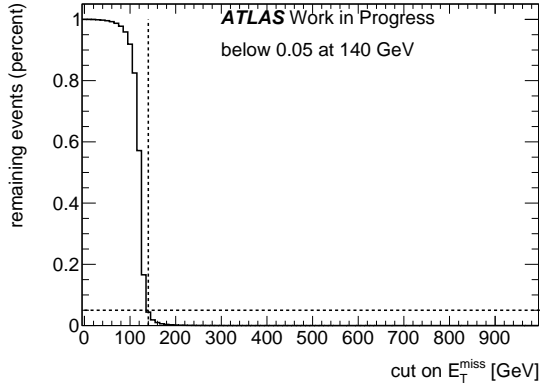
(e) $W \rightarrow \tau_{\text{lep}}, W \rightarrow \tau_{\text{had}}$



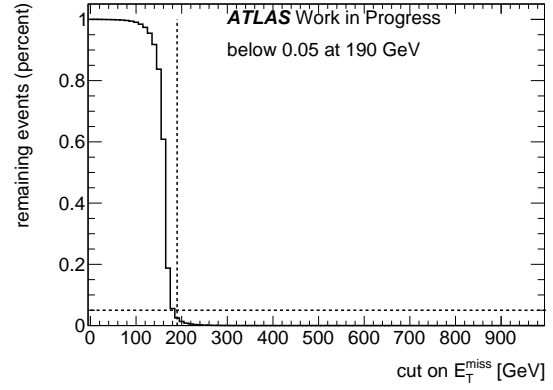
(f) $W \rightarrow \tau_{\text{had}}, W \rightarrow \tau_{\text{had}}$

Figure B.2.: Correlation of $\Sigma_i p_T(\nu_i)$ and true \cancel{E}_T for remaining $t\bar{t}$ samples. For a detailed description cf. Fig. 4.1a. The decay modes of the W bosons are listed for each plot.

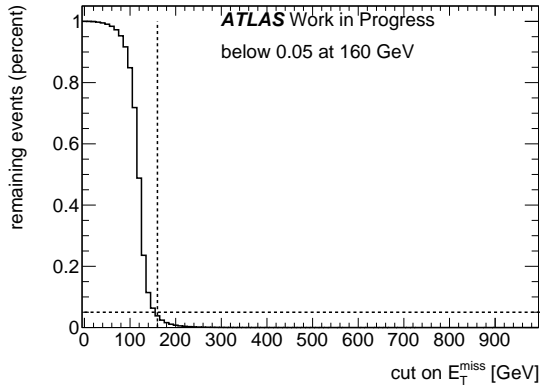
C. Generator cut on \cancel{E}_T



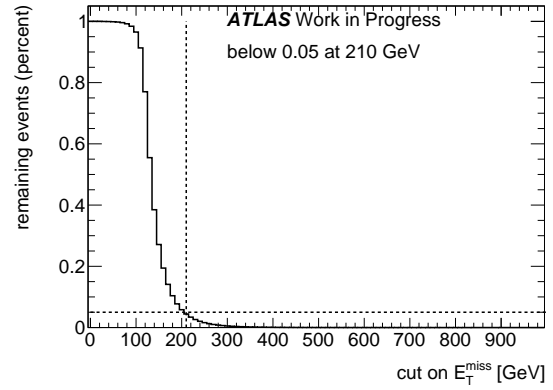
(a) Both W s decaying to light leptons



(b) One hadronically decaying W , one W to light leptons

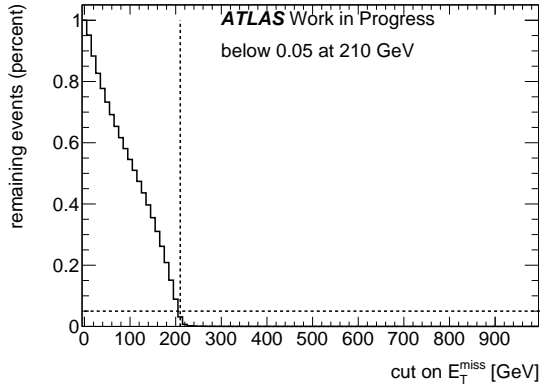


(c) One W to light leptons, one W to hadronic taus

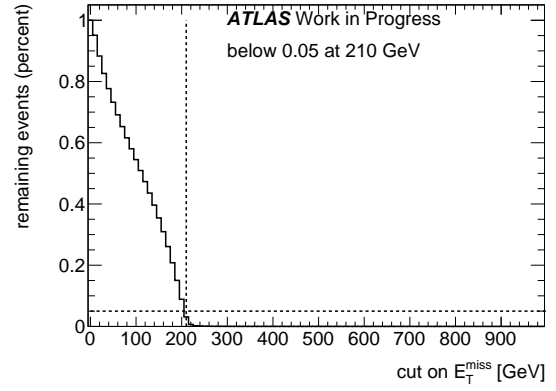


(d) One W to leptonically decaying taus, other W decaying hadronically

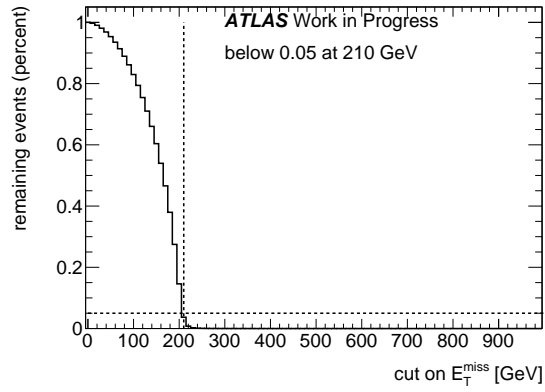
Figure C.1.: Remaining $t\bar{t}$ samples. For a detailed description cf. Fig. 4.2. The decay modes of the W bosons are listed for each plot.



(a) $W \rightarrow e$



(b) $W \rightarrow \mu$



(c) $W \rightarrow \tau$

Figure C.2.: W with jets samples. For a detailed description cf. Fig. 4.2. The decay modes of the W bosons are listed for each plot.

D. MC weights

Description	Dataset ID	N_{gen}	Efficiency	k-fac	Xsection (fb)	$L_{MC} [fb^{-1}]$	Weight
LepT_TauLept	117801	12530000	0.03058	1	530900	771.7930520393	3.8870523543
TauLept_TauLept	117802	1320000	0.00271	1	530900	917.4700901275	3.2698613636
LepTLepT_METT120	157728	13199400	0.0116	1	530900	2143.3025246653	1.3997090777
LepTHad_METT160	157729	9582000	0.0179	1	530900	1008.3014928797	2.9753005636
LepTTauHad_METT120	157730	5720000	0.00815	1	530900	1321.9824652431	2.2693190559
TauLeptT_Had_METT120	157731	11196000	0.0155	1	530900	1360.562404681	2.2049705252
TauLeptT_HadUpTto3lets	157732	10450000	0.0099	1	530900	1988.2380025533	1.5088736842
HadT_Had_METT160	157733	5060000	0.00936	1	530900	1018.2676409838	2.9461802372
TauHadT_HadUpTto3lets	157734	10450000	0.00885	1	530900	2224.1306469241	1.3488416268
TtbarHadT_Had_METT130_160	183733	3000000	0.648	1	4603.7	1005.6323456415	2.9831976
tthbarW	119353	3500000	1	1.22	258.5	11098.0752766592	0.2703171429
tthbarWj	119354	3480000	1	1.22	373.84	7630.1600053324	0.393176517
tthbarZ	119355	3500000	1	1.56	229.58	9772.5836030566	0.3069812571
tthbarZj	119356	3500000	1	1.56	489.27	4585.5861663085	0.6542238857
WW_NoLeptonFilter	161995	9980000	1	1.639	71822	84.7801329193	35.3856486974
WH125_tautauhh	161657	500000	0.42029	1	38.733	30714.2426919684	0.0976745554
WZlep_METT50	157953	13250000	1	1	478.4	27696.4882943144	0.1083169811
WWVStar_lhuhluhu	167006	100000	1	1.5	12.649	5270.5088676312	0.569205
ZZVStar_lhuhluhu	167007	100000	1	1.5	3.7871	17603.6193041289	0.1704195
ZZStar_mumuIIII	167008	100000	1	1.5	0.70607	944119.3446353289	0.03177315
ZZinclusive_1LepEF	146906	500000	0.2122	1	12062	195.3463498597	15.3573884
ZeeNp0	147073	4880000	1	1	1306400	3.7354562156	803.1147540984
ZeeNp1	147074	1910000	1	1	334370	5.7122349493	525.1884816754
ZeeNp3	147076	300000	1	1	40950	7.326007326	409.5
ZeeNp2	147075	745000	1	1	121290	6.14230357	488.4161073826
ZeeNp4	147077	118000	1	1	13043	9.04669983899	331.6016949153
ZeeNp5	147078	36700	1	1	5033.3	7.2914390162	411.4414168937
ZmumuNp0	147081	4895000	1	1	1306800	3.7457912458	800.8988764045
ZmumuNp1	147082	1910000	1	1	334550	5.7091615603	525.4712041885
ZmumuNp2	147083	745000	1	1	121260	6.1438231898	488.2953020134
ZmumuNp3	147084	300000	1	1	40905	7.33406674	409.05
ZmumuNp4	147085	117000	1	1	13041	8.9717046239	334.3846153846
ZmumuNp5	147086	36900	1	1	5023.4	7.3456224868	408.406504065
ZtautauNp0	147089	4900000	1	1	1306300	3.7510525913	799.7755102041
ZtautauNp1	147090	1910000	1	1	334470	5.7105271026	525.3455497382
ZtautauNp2	147091	745000	1	1	121090	6.152448592	487.610738255
ZtautauNp3	147092	300000	1	1	40866	7.3410659228	408.66
ZtautauNp4	147093	115000	1	1	13031	8.8251093546	339.9391304348
ZtautauNp5	147094	36800	1	1	5056.4	7.277905229	412.2065217391
ZbbeeNp0	167100	500000	1	1	22058	22.6675129205	132.348
ZbbeeNp1	167101	500000	1	1	9578.7	52.1991501978	57.4722
ZbbeeNp2	167102	436000	1	1	3936.2	110.7667293329	27.0839449541
ZbbmumuNp0	167105	500000	1	1	22077	22.6480047108	132.462
ZbbmumuNp1	167106	500000	1	1	9577.1	52.2078708586	57.4626
ZbbmumuNp2	167107	436000	1	1	3934.2	110.8230389914	27.0701834862
WmunuPc200	157534	30800000	1	1	27742	1110.2299762094	2.7021428571
WmunuPc200	157535	30800000	1	1	27740	1110.3100216294	2.7019480519
WtaunuPt200	157536	30800000	1	1	27771	1109.0706132296	2.7049675325

Description	Dataset ID	N_{gen}	Efficiency	k-fac	Xsection (fb)	$L_{\text{MC}} [\text{fb}^{-1}]$	Weight
(200, 0)	178474	50000	0.063604	1	1854	424.00975236	2.1675916523
	178475	50000	0.062692	1	1854	430.1779539511	2.1365111607
	178476	50000	0.075939	1	405	1625.7363162994	0.5653315304
	178477	50000	0.073519	1	405	1679.2501274971	0.5473157242
	178478	50000	0.070413	1	405	1753.3238197983	0.5241929581
	178479	50000	0.086916	1	130.4	4411.5649917401	0.2083342309
	178480	50000	0.084102	1	130.4	4559.1731804486	0.2015891837
	178481	50000	0.078672	1	130.4	4873.8507070125	0.1885736874
	178482	50000	0.074532	1	130.4	5144.5765955843	0.1786502704
	178483	50000	0.093858	1	50.1	10633.1265530479	0.0864355366
(500, 200)	178484	50000	0.093078	1	50.1	10722.2328801217	0.0857172205
	178485	50000	0.089607	1	50.1	11137.5672884481	0.0825207135
	178486	50000	0.082349	1	50.1	12119.1998933317	0.0758366895
	178487	50000	0.076716	1	50.1	13009.07231889	0.0706491575
	178488	50000	0.10017	1	23.09	21617.6458444205	0.0425152677
	178489	50000	0.099816	1	23.09	21694.3133789733	0.0423650191
	178490	50000	0.097118	1	23.09	22296.9952453263	0.0412199038
	178491	50000	0.091889	1	23.09	23565.8194586468	0.0390005534
	178492	50000	0.08391	1	23.09	25806.6926973615	0.0356140173
	178493	50000	0.078589	1	23.09	27553.9780915344	0.0333556192
(700, 0)	178494	50000	0.10493	1	11.18	42621.4801689925	0.0215637748
	178495	50000	0.10487	1	11.18	42645.8654918697	0.0215514444
	178496	50000	0.10303	1	11.18	43407.4727179693	0.0211733128
	178497	50000	0.10004	1	11.18	44704.8372064412	0.020558849
	178498	50000	0.093485	1	11.18	47839.4599575588	0.0192117553
	178499	50000	0.085232	1	11.18	52471.7466929367	0.0175157119
	178500	50000	0.07927	1	11.18	56418.2151398055	0.0162904834
	178501	50000	0.1104	1	5.53	81898.4721021045	0.0112221874
	178502	50000	0.11082	1	5.53	81588.0826572129	0.0112648805
	178503	50000	0.1079	1	5.53	83796.0270627649	0.0109680618
	178504	50000	0.10514	1	5.53	85995.732547768	0.0106875071
	178505	50000	0.10079	1	5.53	89707.2261144194	0.0102453285
	178506	50000	0.095142	1	5.53	95032.5967508811	0.0096712079
	178507	50000	0.086921	1	5.53	104020.792674639	0.0088355412
	178508	50000	0.079893	1	5.53	113171.258058557	0.0081211433
	178509	50000	0.11372	1	2.848	154380.757784742	0.0059533326
	178510	50000	0.11423	1	2.848	153691.497638807	0.0059800315
	178511	50000	0.11279	1	2.848	155653.690710887	0.0059046464
	178512	50000	0.10987	1	2.848	159790.477612459	0.005751782
	178513	50000	0.10763	1	2.848	163116.043624277	0.0056345163
	178514	50000	0.10338	1	2.848	169821.820229067	0.0054120254
	178515	50000	0.096262	1	2.848	182379.129617927	0.0050393924
	178516	50000	0.087187	1	2.848	201362.356489854	0.0045643089
	178517	50000	0.079833	1	2.848	219911.312054926	0.0041793212
	178518	50000	0.11828	1	1.646	256820.009442758	0.0035786931
	178519	50000	0.11845	1	1.646	256451.420151029	0.0035838367
	178520	50000	0.11639	1	1.646	260990.383339543	0.0035215091
	178521	50000	0.11534	1	1.646	263366.314521323	0.0034897401
	178522	50000	0.11293	1	1.646	268986.723783666	0.0034168229
	178523	50000	0.1086	1	1.646	279711.516730105	0.0032858139

Description	Dataset ID	N _{gen}	Efficiency	k-fac	Xsection (fb)	L _{MC} [fb ⁻¹]	Weight
	178524	50000	0.10415	1	1.646	291662.704914925	0.0031511742
	178525	50000	0.096841	1	1.646	313675.723266896	0.0029300323
	178526	50000	0.087088	1	1.646	348804.321110709	0.0026349444
	178527	50000	0.080226	1	1.646	378638.729550139	0.002427327
	178528	50000	0.12159	1	0.927	443600.892986342	0.0020718624
	178529	50000	0.12104	1	0.927	445616.594334181	0.0020624905
	178530	50000	0.12037	1	0.927	448096.972486577	0.0020510739
	178531	50000	0.1186	1	0.927	454784.423087768	0.0020209135
	178532	50000	0.11723	1	0.927	460099.228680451	0.0019975691
	178533	50000	0.1143	1	0.927	471893.548365785	0.0019476426
	178534	50000	0.11038	1	0.927	488652.224843353	0.0018808469
	178535	50000	0.10505	1	0.927	513445.336298994	0.001790025
	178536	50000	0.098483	1	0.927	547682.671915044	0.001678125
	178537	50000	0.087847	1	0.927	613992.880556072	0.0014968903
	178538	50000	0.08142	1	0.927	662459.255443494	0.0013873759
	178539	50000	0.1241	1	0.54	746112.752559167	0.0012318245
	178540	50000	0.12447	1	0.54	743894.854925625	0.0012354972
	178541	50000	0.12362	1	0.54	749009.809032459	0.00122706
	178542	50000	0.12336	1	0.54	750588.461353701	0.0012244793
	178543	50000	0.12024	1	0.54	770064.808654296	0.0011935099
	178544	50000	0.11796	1	0.54	784949.072504176	0.0011708785
	178545	50000	0.11423	1	0.54	810580.343102448	0.0011338543
	178546	50000	0.11028	1	0.54	839613.643385859	0.0010946463
	178547	50000	0.1047	1	0.54	884360.960769748	0.0010392589
	178548	50000	0.098192	1	0.54	942974.912341052	0.0009746601
	178549	50000	0.088845	1	0.54	1042181.24365572	0.0008818812
	178550	50000	0.081979	1	0.54	1129467.21224451	0.0008137288
	178551	50000	0.12796	1	0.3456	1130633.99441955	0.0008128891
	178552	50000	0.12734	1	0.3456	1136138.88743463	0.0008089504
	178553	50000	0.12654	1	0.3456	1143321.68425736	0.0008038682
	178554	50000	0.12593	1	0.3456	1148859.88982709	0.0007999931
	178555	50000	0.1241	1	0.3456	1165801.1758737	0.0007883677
	178556	50000	0.12237	1	0.3456	1182282.63402734	0.0007773776
	178557	50000	0.11979	1	0.3456	1207746.27202543	0.0007609877
	178558	50000	0.11652	1	0.3456	1241640.28429391	0.0007402144
	178559	50000	0.11139	1	0.3456	1298823.28688326	0.0007076251
	178560	50000	0.10592	1	0.3456	1365898.09220096	0.000672876
	178561	50000	0.099114	1	0.3456	1459692.13154475	0.0006296396
	178562	50000	0.087829	1	0.3456	1647245.51032035	0.0005579496
	178563	50000	0.080897	1	0.3456	1788396.67634061	0.0005139128
	178564	50000	0.13034	1	0.1906	2012655.25421365	0.0004566505
	178565	50000	0.13043	1	0.1906	2011266.4711662	0.0004569658
	178566	50000	0.12947	1	0.1906	2026179.70058089	0.0004536024
	178567	50000	0.12841	1	0.1906	2042905.42663506	0.0004498887
	178568	50000	0.12713	1	0.1906	2063474.28485965	0.0004454041
	178569	50000	0.12543	1	0.1906	2091441.32850361	0.0004394481
	178570	50000	0.12319	1	0.1906	2129470.62126965	0.0004316002

(1200, 600)

Description	Dataset ID	N_{gen}	Efficiency	k-fac	Xsection (fb)	$L_{\text{MC}} [\text{fb}^{-1}]$	Weight
	178571	50000	0.12058	1	0.1906	2175563.82347162	0.000422456
	178572	50000	0.11692	1	0.1906	2243666.48848963	0.0004096331
	178573	50000	0.11247	1	0.1906	2332439.63576249	0.0003940424
	178574	50000	0.10613	1	0.1906	2471775.04790547	0.00037183
	178575	50000	0.098582	1	0.1906	2661028.2387678	0.0003453853
	178576	50000	0.088558	1	0.1906	2962233.63032372	0.0003102659
	178577	50000	0.08119	1	0.1906	3231056.60591462	0.0002844518
	178578	50000	0.13254	1	0.1074	3512519.60337191	0.0002616583
	178579	50000	0.13229	1	0.1074	3519157.51932053	0.0002611648
	178580	50000	0.13129	1	0.1074	3545961.97906095	0.0002591906
	178581	50000	0.13048	1	0.1074	3567974.77184942	0.0002575915
	178582	50000	0.13035	1	0.1074	3571533.16632844	0.0002573349
	178583	50000	0.12787	1	0.1074	3640801.97255738	0.0002524389
	178584	50000	0.12634	1	0.1074	3684892.73572038	0.0002494184
	178585	50000	0.1237	1	0.1074	3763535.55562581	0.0002442065
	178586	50000	0.12135	1	0.1074	3836418.19720571	0.0002395672
	178587	50000	0.11721	1	0.1074	3971925.16193936	0.0002313941
	178588	50000	0.11245	1	0.1074	4140056.4538098	0.000221997
	178589	50000	0.10736	1	0.1074	4336338.93657705	0.0002119484
	178590	50000	0.099237	1	0.1074	4691288.0082408	0.0001959121
	178591	50000	0.088384	1	0.1074	5267348.70826069	0.0001744863
	178592	50000	0.081231	1	0.1074	5731178.34608601	0.0001603649

E. Cutflow optimistic signal region

	$t\bar{t}V$	Wh	WZ	triboson	
b -jet veto	179.35	45.1	7.7e3	183.32	
$\cancel{E}_T > 270$ GeV	6.41	1.00	299	6.177	
80 GeV $< m_{\tau\tau} < 120$ GeV	1.20	0.90	36.5	0.764	
$ p_T^{\tau_1} + p_T^{\tau_2} > 260$ GeV	0.27	5.2e-05	11.5	0.385	
$m_T > 150$ GeV	0.14	0.0	0.55	5.14e-3	

	ZZ	Z with jets	$t\bar{t}$	WW	
b -jet veto	1.97e3	116e3	11.6e3	3.56e3	
$\cancel{E}_T > 270$ GeV	2.87	322	1.07e3	21.3	
80 GeV $< m_{\tau\tau} < 120$ GeV	0.780	82.8	206	4.15	
$ p_T^{\tau_1} + p_T^{\tau_2} > 260$ GeV	0.549e-3	3.65	5.47	0.515	
$m_T > 150$ GeV	0.372e-3	0.0	1.24	0.23	

	W with jets	(200,0)	(500,200)	(700,0)	(1200,600)
b -jet veto	2.50e3	3.52e3	150	40.7	2.17
$\cancel{E}_T > 270$ GeV	314	122	28.6	19.5	1.28
80 GeV $< m_{\tau\tau} < 120$ GeV	56.9	62.9	16.9	9.33	0.64
$ p_T^{\tau_1} + p_T^{\tau_2} > 260$ GeV	3.98	32.4	5.84	6.13	0.48
$m_T > 150$ GeV	0.15	6.50	3.29	4.73	0.42

Table E.1.: Table including the cutflows for the signal region cuts in the optimistic scenario (cf. Tab. 6.2). The first line holds the event numbers after applying channel definition and b -jet veto. The following lines the subsequent cuts. All considered subprocesses and the four selected signal processes are shown.

Bibliography

- [1] Peskin, M. and Schroeder, D. *An Introduction to Quantum Field Theory*. Westview Press, 1995.
- [2] NIST. *electron g factor*. 2010. URL: <http://physics.nist.gov/cgi-bin/cuu/Value?gem> (visited on 12/06/2014).
- [3] K.A. Olive et al. (Particle Data Group). *Chin. Phys. C*, 38, 090001, 2014.
- [4] Georges Aad et al. “Observation of a new particle in the search for the Standard Model Higgs boson with the ATLAS detector at the LHC”. In: *Phys.Lett.* B716 (2012), pp. 1–29. DOI: 10.1016/j.physletb.2012.08.020. arXiv: 1207.7214 [hep-ex].
- [5] Serguei Chatrchyan et al. “Observation of a new boson at a mass of 125 GeV with the CMS experiment at the LHC”. In: *Phys.Lett.* B716 (2012), pp. 30–61. DOI: 10.1016/j.physletb.2012.08.021. arXiv: 1207.7235 [hep-ex].
- [6] David Griffiths. *Introduction to Elementary Particles*. Wiley-VCH, 2008.
- [7] Prof. Paul Langacker. *Grand unification couplings*. 2012. URL: http://www.scholarpedia.org/article/File:Grand_unification_couplings.jpg (visited on 12/05/2014).
- [8] V. C. Rubin, W. K. J. Ford, and N. . Thonnard. “Rotational properties of 21 SC galaxies with a large range of luminosities and radii, from NGC 4605 /R = 4kpc/ to UGC 2885 /R = 122 kpc/”. In: *APJ* 238 (June 1980), pp. 471–487. DOI: 10.1086/158003.
- [9] S. P. Martin. “a Supersymmetry Primer”. In: *Perspectives On Supersymmetry. Series: Advanced Series on Directions in High Energy Physics, ISBN: 978-981-02-3553-6. WORLD SCIENTIFIC, Edited by Gordon L Kane, vol. 18, pp. 1-98* 18 (July 1998), pp. 1–98. DOI: 10.1142/9789812839657_0001. eprint: hep-ph/9709356.
- [10] S. Schael et al. “Precision electroweak measurements on the Z resonance”. In: *Phys.Rept.* 427 (2006), pp. 257–454. DOI: 10.1016/j.physrep.2005.12.006. arXiv: hep-ex/0509008 [hep-ex].
- [11] CERN Press Office. *LHC sets new world record*. 2009. URL: <http://press.web.cern.ch/press-releases/2009/11/lhc-sets-new-world-record> (visited on 11/03/2014).
- [12] Lyndon Evans and Philip Bryant. “LHC Machine”. In: *Journal of Instrumentation* 3.08 (2008), S08001. URL: <http://stacks.iop.org/1748-0221/3/i=08/a=S08001>.
- [13] Jean-Luc Caron. “CERN Accelerator Complex (operating and approved projects)”. AC Collection. Legacy of AC. Pictures from 1992 to 2002. 1991.
- [14] Michael Benedikt et al. *LHC Design Report*. Vol. 3. Geneva: CERN, 2004.
- [15] Oliver Sim Brüning et al. *LHC Design Report*. Vol. 1. Geneva: CERN, 2004.
- [16] Vittorio Frigo. “LHC map in 3D”. AC Collection. Legacy of AC. Pictures from 1992 to 2002. 1997.

- [17] Cian O’Luanaigh. *CERN announces LHC restart schedule*. 2014. URL: <http://home.web.cern.ch/about/updates/2014/06/cern-announces-lhc-restart-schedule> (visited on 11/05/2014).
- [18] *HL-LHC: High Luminosity Large Hadron Collider*. URL: <http://hilumilhc.web.cern.ch/> (visited on 11/04/2014).
- [19] HL-LHC. *LHC / HL-LHC plan*. 2014. URL: http://hilumilhc.web.cern.ch/sites/hilumilhc.web.cern.ch/files/new_timeplan_24Sept2014.png (visited on 11/05/2014).
- [20] K Hanke et al. “Status of the LIU Project at CERN”. In: *IPAC2014* (2014).
- [21] Maurizio Vretenar. *LINAC4 update*. 2014. URL: <http://indico.cern.ch/event/290148/contribution/0/material/slides/1.pdf> (visited on 11/04/2014).
- [22] Lucio Rossi and Oliver Brüning. “High Luminosity LHC High Luminosity Large Hadron Collider”. In: *Open Symposium - European Strategy Preparatory Group* (2012).
- [23] Oliver Sim Brüning et al. “Electron Cloud and Beam Scrubbing in the LHC; rev. version”. In: LHC-Project-Report-290. CERN-LHC-Project-Report-290 (1999). revised version submitted on 2004-08-20 17:29:43.
- [24] G Arduini et al. “How to maximize the HL-LHC performance (HL-LHC)?”. In: (2013). URL: <http://cds.cern.ch/record/1954204>.
- [25] Joao Pequena. “Computer generated image of the whole ATLAS detector”. 2008.
- [26] *ATLAS detector and physics performance: Technical Design Report, 1*. Technical Design Report ATLAS. Electronic version not available. Geneva: CERN, 1999.
- [27] C Buttar and D della Volpe. *Letter of Intent for the Phase-II Upgrade of the ATLAS Experiment*. Tech. rep. ATL-COM-UPGRADE-2012-040. Geneva: CERN, 2012.
- [28] Abha Eli Phoboo. *A new subdetector for ATLAS*. 2014. URL: <http://home.web.cern.ch/about/updates/2014/05/new-subdetector-atlas> (visited on 11/07/2014).
- [29] Joao Pequena and Paul Schaffner. “An computer generated image representing how ATLAS detects particles”. 2013.
- [30] Matteo Cacciari, Gavin P. Salam, and Gregory Soyez. “The anti- k_t jet clustering algorithm”. In: *Journal of High Energy Physics* 2008.04 (2008), p. 063. URL: <http://stacks.iop.org/1126-6708/2008/i=04/a=063>.
- [31] Zachary Marshall and the ATLAS Collaboration. “Simulation of Pile-up in the ATLAS Experiment”. In: *Journal of Physics: Conference Series* 513.2 (2014), p. 022024. URL: <http://stacks.iop.org/1742-6596/513/i=2/a=022024>.
- [32] ATLAS. *2012 $Z \rightarrow \mu\mu$ event with high pileup, image detail*. 2012. URL: https://twiki.cern.ch/twiki/pub/AtlasPublic/EventDisplayStandAlone/2012_highPileup.png (visited on 11/14/2014).
- [33] Guillaume Unal and Luca Fiorini. *Number of Interactions per Crossing*. 2012. URL: https://atlas.web.cern.ch/Atlas/GROUPS/DATAPREPARATION/InteractionsperCrossing/muplot/2012/mu_2011_2012-dec.eps (visited on 11/10/2014).
- [34] M.A. Dobbs et al. “Les Houches guidebook to Monte Carlo generators for hadron collider physics”. In: (2004), pp. 411–459. arXiv: hep-ph/0403045 [hep-ph].

- [35] Torbjorn Sjostrand, Stephen Mrenna, and Peter Z. Skands. “A Brief Introduction to PYTHIA 8.1”. In: *Comput.Phys.Commun.* 178 (2008), pp. 852–867. DOI: 10.1016/j.cpc.2008.01.036. arXiv: 0710.3820 [hep-ph].
- [36] T. Gleisberg et al. “Event generation with SHERPA 1.1”. In: *JHEP* 0902 (2009), p. 007. DOI: 10.1088/1126-6708/2009/02/007. arXiv: 0811.4622 [hep-ph].
- [37] G. Corcella et al. “HERWIG 6: An Event generator for hadron emission reactions with interfering gluons (including supersymmetric processes)”. In: *JHEP* 0101 (2001), p. 010. DOI: 10.1088/1126-6708/2001/01/010. arXiv: hep-ph/0011363 [hep-ph].
- [38] Johan Alwall et al. “MadGraph 5: going beyond”. English. In: *Journal of High Energy Physics* 2011.6, 128 (2011). DOI: 10.1007/JHEP06(2011)128. URL: <http://dx.doi.org/10.1007/JHEP06%282011%29128>.
- [39] Michelangelo L. Mangano et al. “ALPGEN, a generator for hard multiparton processes in hadronic collisions”. In: *JHEP* 0307 (2003), p. 001. DOI: 10.1088/1126-6708/2003/07/001. arXiv: hep-ph/0206293 [hep-ph].
- [40] S. Dittmaier et al. “Handbook of LHC Higgs Cross Sections: 2. Differential Distributions”. In: (2012). DOI: 10.5170/CERN-2012-002. arXiv: 1201.3084 [hep-ph].
- [41] K.A. Olive et al. (Particle Data Group). *Monte Carlo particle numbering scheme*. 2014. URL: <http://pdg.lbl.gov/2014/reviews/rpp2014-rev-monte-carlo-numbering.pdf> (visited on 12/10/2014).
- [42] *Performance assumptions based on full simulation for an upgraded ATLAS detector at a High-Luminosity LHC*. Tech. rep. ATL-PHYS-PUB-2013-009. Geneva: CERN, 2013.
- [43] *Performance assumptions for an upgraded ATLAS detector at a High-Luminosity LHC*. Tech. rep. ATL-PHYS-PUB-2013-004. Geneva: CERN, 2013.
- [44] Georges Aad et al. “Search for direct production of charginos and neutralinos in events with three leptons and missing transverse momentum in $\sqrt{s} = 8\text{TeV}$ pp collisions with the ATLAS detector”. In: *JHEP* 1404 (2014), p. 169. DOI: 10.1007/JHEP04(2014)169. arXiv: 1402.7029 [hep-ex].
- [45] *b-jet tagging calibration on c-jets containing D^{*+} mesons*. Tech. rep. ATLAS-CONF-2012-039. Geneva: CERN, 2012.
- [46] *Search for Supersymmetry at the high luminosity LHC with the ATLAS experiment*. Tech. rep. ATL-PHYS-PUB-2014-010. Geneva: CERN, 2014.

Erklärung

Hiermit erkläre ich, die vorliegende Arbeit selbständig verfasst zu haben und keine anderen als die in der Arbeit angegebenen Quellen und Hilfsmittel benutzt zu haben.

München, den 22. Dezember 2014

Ort, Datum

Unterschrift des Verfassers